Type Ia supernova explosions in binary systems: The impact on the secondary star and its consequences

TYPE IA SUPERNOVA EXPLOSIONS IN BINARY SYSTEMS: THE IMPACT ON THE SECONDARY STAR AND ITS CONSEQUENCES

by

Evonne Grace Marietta

A Dissertation Submitted to the Faculty of the

DEPARTMENT OF ASTRONOMY

In Partial Fulfillment of the Requirements
For the Degree of

DOCTOR OF PHILOSOPHY

In the Graduate College

THE UNIVERSITY OF ARIZONA

1999

THE UNIVERSITY OF ARIZONA ®
GRADUATE COLLEGE

As members of the Final Examination Committee, we certify that we have read the dissertation prepared by Evonne Grace Marietta

entitled TYPE IA SUPERNOVA EXPLOSIONS IN BINARY SYSTEMS: THE IMPACT ON THE SECONDARY STAR AND ITS CONSEQUENCES

and recommend that it be accepted as fulfilling the dissertation requirement for the Degree of Doctor of Philosophy

Adam Burrows	7/6/99 Date
John Bieging	7/6/99 Date
Matthias Steinmetz	7/6/99 Date
Philip Pinto	7/6/99 Date
	Date

Final approval and acceptance of this dissertation is contingent upon the candidate's submission of the final copy of the dissertation to the Graduate College.

I hereby certify that I have read this dissertation prepared under my direction and recommend that it be accepted as fulfilling the dissertation requirement.

Dissertation Director Adam Burrows — 7/6/99 Date

STATEMENT BY AUTHOR

This dissertation has been submitted in partial fulfillment of requirements for an advanced degree at The University of Arizona and is deposited in the University Library to be made available to borrowers under rules of the Library.

Brief quotations from this dissertation are allowable without special permission, provided that accurate acknowledgment of source is made. Requests for permission for extended quotation from or reproduction of this manuscript in whole or in part may be granted by the head of the major department or the Dean of the Graduate College when in his or her judgment the proposed use of the material is in the interests of scholarship. In all other instances, however, permission must be obtained from the author.

SIGNED: 

ACKNOWLEDGMENTS

Brian Chaboyer provided the stellar models used in the simulations and Matthias Steinmetz provided the Poisson solver. Conversations with Phil Pinto, Jim Liebert, and Betsy Green are gratefully acknowledged. The calculations were performed on the Cray C90 at Pittsburgh Supercomputer Center and on the Cray T90 at the San Diego Supercomputer Center.

On a personal note, I'd like to thank my family and friends for not asking me "When are you going to graduate?" years before it actually happened. I'd also like to thank my office mates, Aditya Dayal, Sally Oey, Lisa Wells, Mario Hamuy, and Valorie Burkholder for their support. I might not have made it through without the support of the other grad students including Craig Kulesa, Tim Pickering, Peter Tamblyn, Eric Hooper, Julio Saucedo-Morales, Dave Sudarsky, Chad Engelbracht, Sue Dubuque, Anne Turner and Doug Williams (and their 16-legged beastie). Special thanks to Ruth Kneale, who convinced me to take dance classes to relieve a little stress. It worked. Special thanks to Lisa Wells, Mario Hamuy, and Doug Miller for sharing their supernova expertise. Finally and most importantly, I'd like to thank my advisor, Adam Burrows, for his advice, patience, and unending chocolate supply that made this successful project possible.

Dedication

Dedicated to my parents, Mom and Fat Pops, and to my Sweetbaby, Al.

Table of Contents

List of Figures

List of Tables

ABSTRACT

One method of discriminating between the many Type Ia progenitor scenarios is searching for contaminating hydrogen and helium stripped from the companion star. However, this requires understanding the effect of the impact on different companion stars to predict the amount of mass stripped and its distribution in velocity and solid angle. We present several high-resolution 2-D numerical simulations of the impact of a Type Ia supernova explosion with low-mass, hydrogen-rich main sequence, subgiant, and red giant companions. The binary parameters were chosen to represent several classes of single-degenerate Type Ia progenitor models that have been suggested in the literature.

We find that the main sequence and subgiant companions lose $0.15 - 0.17$ $M_\odot$ as a result of the impact of the supernova shell. The red giant companions lose $0.53 - 0.54$ $M_\odot$, $96\% - 98\%$ of their envelopes. The main sequence companion receives a kick of 86 km s^{-1} and the subgiant receives a kick of 49 km s^{-1}. In all cases, the kick to the remnant is smaller than the original orbital velocity. Because it is too small to intercept more than a negligible amount of momentum, the red giant core will not receive an appreciable kick. The characteristic velocity of the stripped hydrogen is less than 10^3 km s^{-1} for all the scenarios: $420 - 590$ km s^{-1} for the red giant companions (depending on the scenario), 850 km s^{-1} for the main sequence companion, and 900 km s^{-1} for the subgiant companion. The stripped hydrogen contaminates a wide solid angle behind the companion: 115° from the downstream axis for the red giant, 66° for the main sequence star, and 72° for the subgiant. We find that the bulk of the stripped hydrogen and helium is embedded within the low-velocity iron of the supernova ejecta and may be visible

as narrow emission lines months after maximum light. To make any definitive predictions requires non-LTE radiative transfer calculations using the low-velocity distribution of the stripped material to determine the effect of hydrogen and helium contamination on the late-time supernova spectrum. With synthetic late-time spectra, it will be possible to place constraints on some of the single-degenerate Type Ia scenarios.

CHAPTER 1

INTRODUCTION

Unlike a Type II explosion, a Type Ia explosion, the thermonuclear explosion of a CO white dwarf, is characterized by the absence of hydrogen in its spectrum. Although a massive star that is responsible for a Type II supernova explosion can be in a single or a binary system, the Type Ia progenitor scenarios that are based on the thermonuclear explosion of an accreting white dwarf require a companion as a mass donor to enable the white dwarf to reach its critical mass. However, despite searches for the remnant of the companion star, no direct evidence has yet been observed (Ruiz-Lapuente 1997).

One method of discriminating between the many Type Ia progenitor scenarios is searching for contaminating hydrogen and helium stripped from the companion star. However, this requires understanding the effect of the impact on different companion stars to predict the amount of hydrogen stripped and its distribution in velocity and solid angle for the types of binary scenarios that have been proposed as progenitor models. To date, there have been only three numerical investigations of supernova impacts on companion stars. Fryxell & Arnett (1981) and Taam & Fryxell (1984) focused on impacts with low-mass main sequence stars. Livne et al. (1992) focused on red giant companions. In this paper, we improve upon the

earlier theoretical work by exploring the nature of the interaction between the supernova ejecta and the companion star for specific Type Ia binary scenarios with higher resolution than was possible in the past. We select realistic ejecta profiles and realistic stellar models. It is no longer necessary to represent the supernova-secondary interaction by the collision of a simple shell with a polytropic companion. Although the earlier simulations studied the stripped mass and kick, they did not study or provide the distribution of stripped hydrogen in velocity and solid angle, which are essential to predict any spectral signatures of the impact.

The goal of this project is to simulate with a 2-D hydrodynamics code the impact of a realistic supernova blast on a companion star in the context of current Type Ia progenitor scenarios in which the companion is hydrogen-rich. We select several of these scenarios from the literature to cover the possible range of secondary types which are typically low-mass ($1.0 - 2.0\ M_{\odot}$) main sequence, subgiant, or red giant stars. We use realistic stellar models and supernova debris profiles to represent each binary system. For each scenario we explore the hydrodynamics of the supernova-secondary interaction, calculate the amount of stellar material stripped from the secondary and the kick delivered by the impact, and construct the velocity and solid angle distributions of the stripped material. With the velocity and spatial distributions of the stripped material within the supernova debris it is possible to predict whether the contaminating hydrogen and helium are observable in the supernova spectrum as broad emission lines near maximum light or as narrow emission lines at late times. In addition, we can explore the change in structure of the secondary star caused by the impact to explore the possible final states (perhaps observable) of the secondary.

We find that our main sequence and subgiant companions lose $0.15 - 0.17$

$M_\odot$ as a result of the impact of the supernova ejecta. In contrast, the red giant companions lose almost their entire envelopes, $0.53 - 0.54\ M_\odot$. The bulk of the stripped hydrogen, which has a characteristic velocity of less than or equal to 10^3 km s^{-1}, is embedded within the inner, low-velocity supernova debris. The complication that hydrogen and helium can be hidden deep and unseen within the ejecta, and obscured by competing iron and cobalt lines, can be addressed by radiative transfer calculations (Pinto et al. 1999). In principle, radiative transfer calculations can reveal how much of the stripped material can be hidden and when it is likely to be observable.

1.1. History of Theory

The effect of a supernova explosion on a nearby companion star has been the subject of speculation for many years. One issue raised was the strength of the kick delivered to the companion. Colgate (1970) proposed that the shock-heating of the stellar envelope would cause material to evaporate preferentially back in the direction of the supernova. The secondary would receive a substantial kick from the ablation (evaporation from the surface of the star), as well as a smaller kick from the direct collision with the ejecta. Other groups (Cheng 1974; Wheeler et al. 1975) made similar arguments supporting the suggestion that the kick due to ablation was larger than the kick from the collision. Numerical simulations by Fryxell & Arnett (1981) and Taam & Fryxell (1984) showed that the momentum transfer to the secondary was much less than previously thought and that ablation did not substantially increase the kick. The small binary separations we employ for the simulations in this paper, necessary for Roche lobe overflow, result in kicks larger than the ~ 10 km s^{-1} kicks reported by Fryxell & Arnett (1981). However, our typical $40 - 80$ km s^{-1} kicks are still small in comparison with typical orbital

velocities.

The impact of the supernova debris on a nearby companion may be quite dramatic. The supernova ejecta may either directly strip material from the companion by direct transfer of momentum, or, through the conversion of the blast kinetic energy into internal heat, by evaporation. Because the incident energy (a fraction of 10^{51} ergs) greatly exceeds the secondary's binding energy (10^{48} ergs), Sofia (1967) suggested that a main sequence secondary in Roche lobe overflow would be completely destroyed. It was not until a more detailed study of the shock propagation into the stellar envelope was done that it was realized that, because the kinetic energy of the impact is deposited in the outer layers of the star, a main sequence star could easily survive such an impact (Cheng 1974).

Wheeler et al. (1975) analytically estimated the amount of mass stripped and the kick received by the companion as a result of the inelastic collision and the shock-heating. They calculated the outcome of the impact for an arbitrary secondary star using a geometrical parameter they devised, which depended on the incident momentum and the mass and compactness of the secondary. Their analysis implied that main sequence stars (represented by an $n = 3$ polytrope), being tightly bound, are only slightly stripped by an explosion in a close binary system. Red giants with loosely-bound envelopes are so catastrophically heated by the impact that the entire envelope is ejected.

The analytic prescription for the stripped mass and kick proposed by Wheeler et al. (1975) was put to the test in a series of numerical simulations of supernova impacts on both low-mass main sequence companions (Fryxell & Arnett 1981; Taam & Fryxell 1984) and low-mass red giants (Livne et al. 1992). Fryxell & Arnett (1981) demonstrated that the collision of a supernova shell with a 2.0

$M_\odot$, n=3 polytrope, with a binary separation 5.9 times the stellar radius, ejects 0.013 – 0.052 $M_\odot$ from the secondary, a mass loss roughly consistent with the analytic estimates of Wheeler et al. (1975). Although in their study the emphasis was on the momentum transfer rather than the stripped mass, Taam & Fryxell (1984) performed numerical simulations with n= 3/2 and n= 3 polytropes that were designed to represent the range of compactness expected from a fully convective star to a radiative star. They found that the momentum was more efficiently transferred for the n=3/2 star, which is less centrally concentrated than the n= 3 star. The stripped n= 3/2 star presents a larger geometrical area to intercept the momentum, even when a higher fraction of mass is stripped, so that the momentum transfer is more efficient. More recently, Livne et al. (1992) simulated a Type Ia supernova explosion of a white dwarf in a close binary with a low-mass red giant that is almost close enough to be in Roche lobe overflow. The blast stripped the red giant of almost its entire envelope, imparting a velocity to the stripped material well below the velocity of the supernova ejecta. This not only confirmed the conclusion of Wheeler et al. (1975) that the impact would destroy the red giant, but also verified a prediction of Chugai (1986). Chugai (1986) focused on the supernova red giant interaction for Type Ia events in which the hydrogen donor is a symbiotic star - with a binary separation 3 – 10 times the red giant's radius. Chugai's analytic model predicted that 0.3-1.0 $M_\odot$ would be ejected from the companion with a characteristic velocity less than or equal to 10^3 km s^{-1}, much smaller than the 10^4 km s^{-1} characteristic velocity of the supernova ejecta, and that it would fill the inner 20% of the radius of the supernova ejecta. The confirmation by Livne et al. (1992) of the low velocity of the stripped hydrogen has important implications for the identification of Type Ia progenitors. Our more detailed calculations build on and extend this earlier, seminal work.

1.2. Discriminating Between Type Ia Progenitor Scenarios by Searching for Hydrogen

The exact amount of hydrogen stripped and its characteristic velocity is a key issue in light of the current interest in identifying the progenitors of Type Ia supernovae. Because it is difficult to reconcile the extremely hydrogen-poor spectra with the presence of a hydrogen-rich companion, the amount of stripped hydrogen can be used to discriminate between Type Ia progenitor scenarios. Type Ia explosions, which are characterized by a lack of hydrogen, could be the result of mass accretion onto a white dwarf in a binary system (single-degenerate scenario) (Whelan & Iben 1973; Nomoto 1982) or the merging of two degenerate white dwarf stars (double-degenerate scenario) (Iben & Tutukov 1984; Webbink 1984). Naturally, the double-degenerate scenario could account for the lack of hydrogen in the supernova spectrum. However, no double-degenerate binaries have been found that are close enough to merge within a Hubble time and are massive enough to exceed the Chandrasekhar mass (Marsh et al. 1995; Saffer et al. 1998). The single-degenerate scenario is currently in favor (Livio 1999). If the companion is a main sequence, subgiant, or red giant star, the single-degenerate scenario necessarily implies that the binary system is rich in hydrogen. Hydrogen-rich material could be ejected from the secondary star as a consequence of the impact of the supernova shell. Hydrogen could also be present in the immediate environment as circumstellar material from stellar winds, mass lost from the primary in an earlier phase of mass transfer, or even as a layer of hydrogen on the white dwarf primary. If the hydrogen is swept up by the supernova ejecta, the origin of the material may determine its characteristic velocity, which in turn determines when it is most likely to be observed. Circumstellar material swept up with the supernova ejecta is expected to be observed as transient narrow H_α emission or absorption lines

(Wheeler 1992; Filippenko 1997) near maximum light. If the hydrogen is stripped from the secondary and embedded within the inner iron layer of the supernova ejecta, it is more likely to be observed in emission as narrow H_α lines months after maximum light (Chugai 1986). Searches for hydrogen must be targeted at either early-times near maximum light or at late-times when the photosphere has receded to reveal the iron layer (Chugai 1986).

Identification of hydrogen at early-times, either in emission or absorption, has been claimed in at least three Type Ia supernovae: 1981B, 1990M, and 1990N. Branch et al. (1983) presented high-quality optical spectra of SN1981B from maximum light to 116 days post-maximum. Their March 13 observation showed a small, narrow emission feature consistent with the rest wavelength of H_α. The feature was absent from a spectrum that was taken just 5 days later. Unable to firmly conclude that the feature was H_α, they suggested that high-resolution spectra be taken of supernovae near the same phase ($\sim$ 6 days past maximum light) to search for H_α emission. Cumming et al. (1996) searched for narrow H_α emission in high-resolution spectra of SNIa 1994D 10 days before maximum and 6.5 days after maximum without detecting any hydrogen either in emission or absorption. Likewise, Ho & Filippenko (1995) in their high-resolution echelle observations of SNIa 1994D at 23 days past maximum did not detect any H_α in emission or absorption.

From a series of observations of SNIa 1990N from 14 days before maximum light to 1 week past maximum light, Leibundgut et al. (1991) suggested that an unidentified absorption feature at 6300Å could be hydrogen. They suggested that a thin layer of hydrogen on the surface of the progenitor star could be responsible for the feature, but because the velocity of the feature (1.2×10^4 km s^{-1}) was much

lower than that of the other lines, this was unlikely. Later, based on an analysis of optical and UV spectra of SN 1990N using synthetic spectra, Jeffery et al. (1992) concluded that the unidentified absorption feature at 6300Å, and an additional unidentified feature at 6900Å, were probably due to C II at 6580Å and 7243Å .

Polcaro & Viotti (1991) identified a broad H_α absorption feature in SNIa 1990M at four days after maximum light. This was later convincingly ruled out by Della Valle et al. (1996), who showed from a spectrum obtained a few days past maximum light that the absorption feature was due solely to observational bias. They found no evidence of H_α in SN 1990M. Using an upper limit to the H_α equivalent width and a measurement of the Si II 6350Å equivalent width, they set an upper limit in the supernova atmosphere for H/Si of 2.0×10^{-6}, relative to solar. By assuming perfect mixing and using the abundances of the standard W7 model (Nomoto et al. 1984), they derived the upper limit to the mass fraction, X(H), of 0.007. However, they pointed out that if the hydrogen is buried deep within the supernova ejecta instead of being perfectly mixed, the integral mass fraction could be much higher. Likewise, if the hydrogen is restricted to the outer layers, the mass fraction could be much lower. Scaling X(H) by the ratio of the mass in the atmosphere to the total mass and assuming that 20 days past the explosion only 1/20 of the ejecta are revealed, they derived an X(H) of $\sim 0.007\ M_{atm}/M_{tot} \approx 3 \times 10^{-4}$.

A similar argument was made earlier by Applegate & Terman (1989) to place an upper limit on the hydrogen mass fraction in SN 1981B. Using the upper limit of [H/Si] < -4.0 in the LTE spectral fit to the maximum light observations of SN 1981B of Branch et al. (1982), Applegate & Terman (1989) derived an upper limit on the hydrogen mass fraction near maximum light in SN 1981B of 0.02. To find

a lower limit to the hydrogen contamination due to the impact of the supernova ejecta on the secondary star, Applegate & Terman used the analytic prescription developed by Wheeler et al. (1975). They focused on a cataclysmic variable system with a 0.2 $M_{\odot}$ main sequence companion, represented by an n=3/2 polytrope, that was close enough to the primary to be in Roche lobe overflow. If the Type Ia progenitors are cataclysmic variables, Applegate & Terman 1989 concluded that X(H) > 0.01. This is just below the Applegate & Terman upper limit of X(H) < 0.02. In contrast, if the companion is a low-mass red giant with an envelope mass of 0.5 $M_{\odot}$, then X(H) > 0.20, which clearly would exceed the upper limit they deduced from observations of SN 1981B. Applegate & Terman (1989) conclude that binary scenarios with hydrogen-rich companions are not likely candidates for Type Ia progenitors. However, to directly compare their lower limit with their upper limit based on maximum light observations of SN 1981B, they implicitly assumed that the stripped hydrogen from either the low-mass main sequence star or the red giant companion was ejected at high velocities.

It is currently believed, based on the work of Chugai (1986) and Livne et al. (1992), that any material stripped from a red giant companion will have a characteristic velocity $\lesssim 10^3$ km s^{-1}, much lower than that of the supernova ejecta. As we show below, we agree with this general conclusion. If any hydrogen is embedded within the supernova ejecta, narrow hydrogen emission lines will appear only after the photosphere retreats into the iron layer. Thus, a critical test of the presence of a secondary star is the detection of low-velocity hydrogen lines in the late-time spectrum (Ruiz-Lapuente et al. 1993). However, such a detection is difficult because of the number of Fe lines that overwhelm the spectrum. To date, there has been only one claim of a detection of a low-velocity hydrogen line, ostensibly from a stripped companion. Ruiz-Lapuente et al. (1993) initially

identified a weak H_α line in a spectrum of SNIa 1991bg, a peculiar underluminous Type Ia supernova, 197 days after maximum light. However, this was not verified by Turatto et al. (1996). Turatto et al. were not able to associate any emission lines with H_α in their observations of SN 1991bg, although they suggested a possible blend with [Co III] at 6578Å or numerous Fe II and [Fe II] lines in that region of the spectrum. Garnavich & Challis (1997), in a reanalysis of a spectrum of SN 1991bg at 200 days after maximum light, confirmed the existence of the the narrow emission lines of Ruiz-Lapuente et al. (1993), but they could not unambiguously identify them.

A key question for theoreticians is how much contaminating hydrogen and helium, whether of circumstellar or companion origin, can be hidden within the supernova ejecta. Very few theoretical upper limits have been set (Wheeler & Harkness 1990; Wheeler 1992). Wheeler (1992) claimed that, if the hydrogen is in LTE in the outer layers of the supernova ejecta, as much as 0.1 $M_\odot$ could be present without contributing to the spectrum at maximum light. Branch et al. (1991) found a tighter upper limit of 1% by mass ($\sim$ 0.01 $M_\odot$) in a non-LTE calculation. By adding hydrogen to a synthetic spectrum and comparing with the maximum-light optical spectrum of SN 1981B, they concluded that 1% by mass is an upper limit on the hydrogen contamination for a layer of hydrogen uniformly mixed in the line-forming layer at maximum light. They found that, not only would a weak H_α line be visible, but, as an indirect consequence of hydrogen contamination, that the optical depth in the Lyman continuum would change the ultraviolet radiation field, the ionization structure in the line-forming layer, and, hence, the strengths of many of the non-hydrogen lines. Because Applegate & Terman (1989) estimated X(H) $>$ 0.01, Branch et al. (1991) concluded that accreting white dwarfs with hydrogen-rich companions are unlikely to be progenitors of Type Ia supernovae.

However, there are several caveats. First, the synthetic spectra employed for these investigations were done only near maximum light, when only high-velocity hydrogen would be visible. If most of the contaminating hydrogen is at low velocities, synthetic spectra need to be calculated at much later times when the photosphere has receded into the inner ejecta. Second, the hydrogen buried within the supernova ejecta may not be uniformly mixed in angle. Because non-uniform mixing may act to hide the embedded hydrogen, the angular dependence of the spectra needs to be considered.

1.3. Outline of This Paper

In this paper, we explore in detail the theoretical expectations for the distribution of hydrogen and helium in Type Ia debris, the hydrodynamic character of the impact, the kick to the secondary, and the nature of the post-impact structure. In §2, we review the numerical methods used. In §3, we describe the classes of supernova Type Ia progenitor scenarios and the criteria for selecting the candidate scenarios. In §4, we discuss details of the main sequence simulations, including the hydrodynamics of the impact, the stripped mass, the velocity and solid angle distributions of the stripped material, and the kick received by the companion. In §5, we present a sequence of simulations with the main sequence secondary to determine systematic trends in the quantity of stripped hydrogen and its velocity and solid angle distributions as the binary separation increases. In §6, we discuss details of the subgiant simulations, including a description of the impact, the stripped mass, the velocity and solid angle distributions of the stripped material, and the kick received by the companion. Section 7 contains similar details for the red giant simulations. In §8, we explore the implications of the revealed velocity distributions of the stripped material and the possibility that contaminating

hydrogen may be observable in a Type Ia supernova spectrum. In §9, we speculate on the effect of the impact on the future evolution of the secondary, and in §10 we summarize our conclusions and suggest directions for future work. Postscript images, MPEG movies, and a selection of figures presented in this paper, are posted at http://www.astrophysics.arizona.edu and are available via anonymous FTP at www.astrophysics.arizona.edu, in directory pub/marietta.

CHAPTER 2

NUMERICAL METHODS AND TECHNIQUES

The hydrodynamics code we employ for these simulations is an extension of the code, *Prometheus* (Arnett, Fryxell & Müller 1989), which is based on the Piecewise-Parabolic Method (PPM) pioneered by Woodward & Colella (1984). Our version of PPM is a non-relativistic, explicit, automatically conservative, Eulerian scheme that achieves second-order spatial and temporal accuracy. Fluxes at interfaces are obtained by solving the Riemann shock-tube problem and shocks are resolved to one or two zones.

A simple equation of state, including just radiation and ideal gas, is employed for all the calculations involving the main sequence companion and the envelope of the red giant; the degenerate core of the red giant is added only as a gravitational point mass. For the calculations involving subgiant companions, where degenerate electrons are required, we use a tabulated equation of state with arbitrary degeneracy and relativity. We tabulate the pressure, energy, and entropy of the ionization electrons, and any pair-produced electrons and positrons, by directly integrating the appropriate Fermi-Dirac integrals, following the prescription of Cox & Giuli (1968). Using the ionization electron density ($n_e = \rho Y_e N_{av}$, where ρ is the density, Y_e is the electron fraction, and N_{av} is Avogadro's number) and

the temperature (T) as independent variables, we use an iterative technique to solve for the degeneracy factor ($\eta = \mu/k_B T$, where μ is the chemical potential, and k_B is Boltzmann's constant), which can be used to directly integrate the Fermi-Dirac integrals for pressure and energy. This method, although laborious, is thermodynamically consistent. The table, once generated, is accessed by a second-order interpolation routine. We estimate the pressures and energies to be accurate to better than $\sim 10^{-4}$.

We incorporate into PPM an integral Poisson solver created by Müller & Steinmetz (1995) to calculate the gravitational potential for an arbitrary 2-D mass distribution. Having found the gravitational potential, the gravitational force can be calculated using a finite difference approximation to the gradient. In the simulations involving the red giant companions, the gravitational point mass of the compact core is added directly to the force. In our implementation the solver expands the gravitational potential in Legendre polynomials. Up to twenty moments can be employed, including the dipole moment which we include to allow the secondary to move freely down the hydrodynamic grid in response to the impact of the blast. With the addition of an interpolation routine, the hydrodynamical equations can be differenced in spherical (r, θ), Cartesian (x, y), or cylindrical coordinates (ρ, z) while the gravitational potential can be constructed in spherical coordinates (r, θ). To improve accuracy, the gravitational potential can be centered on the center of mass at each cycle, in effect following the star as it moves down the grid. This decreases errors, notably in the stellar core, that over the long timescale of the simulation can otherwise slowly decrease the star's terminal velocity. Even with this improvement, the terminal velocity slowly decreases at an average rate of $\sim 2.8\%$ per stellar sound crossing time in a typical simulation with a low-mass main sequence companion. Thus, as will be seen in §4.6, we determine

the kick after the terminal velocity is reached ($4000 - 5000$ seconds), but before the small errors have time to grow appreciably.

For simplicity, we use all the mass on the hydrodynamic grid, stellar and supernova, to calculate the gravitational potential. Because the grid is so large, typically 6R (R = the stellar radius) in the ρ direction, and, since the explosion is $\sim$ 1R away from the upper boundary, about 42% of the supernova debris passes through the grid. Only a small fraction of the ejecta directly collide with the secondary. The characteristic velocity of the supernova ejecta is so fast that the error to the kick from including the supernova material on the grid is only $\sim$ 4 km s^{-1}, which is an error of $\sim$ 5%.

For this project, a selection of low-mass stellar models were evolved by Chaboyer (1998). A well-known difficulty with PPM is its unwillingness to maintain a star in hydrostatic equilibrium. Following the lead of Sills et al. (1997), we reintegrate the main sequence and subgiant secondaries using a 1-D fourth-order Runge-Kutta program, the entropy and composition profiles, and the same equation of state used in our PPM code. We do not attempt to reproduce the distortions in the secondary due to the Roche lobe geometry.

The weakly-bound envelope of the red giant requires special treatment. We reintegrate its entropy profile with a softened potential ($\phi(r) = -GM_c/(r + r_c)$) to help stabilize it. Even with this adaptation, we find it necessary to switch to spherical coordinates for the red giant impacts. We surround each secondary star with a high-entropy, very low-density hydrostatic envelope which serves to fill the Eulerian grid with a background medium. In later sections we refer to this background material as the "circumstellar" medium to distinguish it from the stellar envelope. The new 1-D models with their hydrostatic envelopes are

interpolated onto a 2-D cylindrical grid (main sequence or subgiant models) or a 2-D spherical grid (red giant envelopes). We use 2-D cylindrical coordinates whenever possible in order to efficiently follow the stripped material. To stabilize the envelope of the red giant, we must use 2-D spherical coordinates.

We verify that each secondary star remains in hydrostatic equilibrium by running a simulation without the supernova explosion. Figure 2.1 shows the result of the hydrostatic equilibrium tests for the main sequence, the subgiant, and the red giant secondaries. The main sequence and subgiant simulations were run for three sound crossing times. Because the envelope of the red giant will be completely disrupted in less than one sound crossing time, the red giant simulation was run for only one sound crossing time. In addition, we estimate the fractional change in radius by the fractional change in gravitational energy for the main sequence and subgiant secondaries. We find that the radius changes by at most $\sim 1\%$. In the red giant case, the radius changes by at most $\sim 8\%$.

We perform all of the simulations with the main sequence and subgiant secondaries in 2-D using cylindrical coordinates (ρ, z), with the z-axis defined to be the direction joining the primary and secondary of the original binary system. We estimate that the error in neglecting the orbital motion of the secondary, necessary for a 2-D calculation, is $\sim 10^{-2}$, the ratio of a typical orbital velocity of 10^2 km s^{-1} to a characteristic velocity of the supernova ejecta of 10^4 km s^{-1}. The thermonuclear explosion of the white dwarf occurs exterior to the grid and the supernova ejecta, specified by a realistic density and velocity profile, flows onto the grid via time-dependent boundary conditions in assumed spherical homologous flow. Before the supernova reaches the top edge of the grid, the boundary is transmitting, but subject to the constraint that material is allowed only to leave the

grid. All of the exterior boundaries share this constraint. The interior boundary ($\rho = 0$) is reflecting.

We switch to spherical coordinates for the red giant companions because only in these coordinates is the loosely-bound envelope of the red giant stable. We position the red giant envelope at the origin and add a gravitational point mass to the force to represent the degenerate core. We assume throughout the simulation that the degenerate core does not move as a result of the impact. We justify this by noting that, because of the extremely small solid angle subtended by the degenerate core and its very high areal density, it can receive only a negligible ($\ll 1$ km s^{-1}) kick. The supernova explosion, which in this case occurs on the grid, is interpolated onto the grid from a post-explosion ejecta profile. To avoid numerical problems associated with high-Mach flows, we assume an initial temperature in the supernova ejecta high enough that the internal energy is $\sim 7.7\%$ of the specific kinetic energy.[1] To minimize numerical problems at the center of the supernova where the expansion leaves a low-density interior, we employ a minimum temperature which decreases linearly with time to mimic the cooling of the interior. Outside of the supernova ejecta at the interface between the supernova ejecta and the "circumstellar" medium, a minimum temperature of 100 K is enforced. These numerical problems appear only in the spherical calculations. The cylindrical calculations in which the supernova is added by time-dependent boundary conditions are always well-behaved.

With the change to spherical coordinates, we alter the boundary conditions. The outer boundary is straightforward. As in cylindrical coordinates, the outer

---

[1]Our initial temperature is a factor of $1.0 - 4.0$ higher than the temperature provided in the supernova ejecta model hedtb11 (Woosley & Weaver 1994).

radial boundary is transmitting, but subject to the constraint that material is allowed only to leave the grid. In spherical coordinates, the Courant condition, the maximum timestep, is generally $\Delta t < r\Delta\theta/v$ near the origin, where $r\Delta\theta$ is usually less than Δr which can be problematic if the resulting timestep becomes unreasonably small. The inner radial boundary is fixed at a small, but non-zero, radius. This helps to stabilize the interior of the envelope and, in addition, helps to avoid Courant problems. The inner boundary is non-transmitting (no mass flux allowed) with a zero-velocity condition. The inner boundary seems to affect the flow only after the envelope has been stripped. After the mass-stripping phase of the interaction, we regrid the calculation by removing the innermost zones, usually the first 25, in effect moving the inner boundary outward about a factor of 10 in radius, which increases the timestep by the same factor, allowing us to continue the simulations efficiently. The mass enclosed in the innermost zones is added to the gravitational point mass. The region removed is typically only 1% in radius, and therefore, only 10^{-4}% in computational volume. The inner and outer angular boundaries are both reflecting. For high-velocity flow, the angular boundaries, which are along the axis of symmetry, manifest minor numerical artifacts which, however, do not affect the results of the simulations.

In addition to determining the stripped mass and the kick given to the companion, we find the distribution of the stripped material in both velocity and solid angle. The velocity distribution can in principle be used with a radiative transfer code to predict when, and if, the contaminating hydrogen is observable in the supernova Type Ia spectrum and to place useful constraints on the type of binary scenarios likely to be responsible for Type Ia supernovae. The solid angle distribution can be used to determine by how much the stellar material lags behind the supernova ejecta and the size of the solid angle contaminated

by the stellar hydrogen and helium. It may also be relevant for estimates of the polarization of the emergent light. As stripped stellar material flows through the outer boundary, we record its mass, velocity, entropy, and composition. We advect the electron fraction Y_e and ion fraction Y_i along with ten general composition labels, five of which are reserved for the Type I supernova ejecta ("hydrogen", "helium", "oxygen-group", "silicon", and "iron-group"), four for the companion star ("hydrogen", "helium", "oxygen-group", and "silicon/iron-group"), and one for the "circumstellar" medium. The Y_i and Y_e are required by the equation of state, but we advect the composition labels as mass fractions so we can keep track of the origin of the stripped companion material and can distinguish it from the supernova and "circumstellar" material with which it is intermixed. To find the velocity and solid angle distributions, we include the distribution of the stripped companion material on the grid, as well as the stripped material that has left the grid. The stripped mass left on the grid is usually extremely small, given the length of a typical simulation.

For the main sequence and subgiant simulations we generally employ a $\sim 300(\rho) \times 600(z)$ cylindrical grid, and for the red giant a $\sim 600(r) \times 300(\theta)$ spherical grid, with nonuniform zoning that is finest in the region surrounding the secondary and coarsest near the edge of the grid. To cover 6 stellar radii around the secondary and still resolve the center of the star well enough to maintain hydrostatic equilibrium, nonuniform zoning is necessary. This nonuniform zoning, although efficient, creates difficulties in quantifying the effect of increasing or decreasing the resolution.

To test the effect of the resolution we employ a cylindrical grid that has uniform zoning in a rectangular region enclosing the secondary. Outside this

region, the zones are slowly increased in size to keep the calculation tractable. For the main sequence calculation, we performed two simulations: one with a spacing of 8.0×10^3 km requiring a $300(\rho) \times 550(z)$ grid and one with a slightly smaller spacing of 6.0×10^3 km requiring a $320(\rho) \times 845(z)$ grid. We can not vary the "resolution" by a large factor because greatly decreasing the resolution destabilizes the secondary while greatly increasing the resolution creates enormous Courant and data storage problems.

Nevertheless, we find that changing the resolution in the region around the secondary can affect the results in several systematic ways. First, the amount of mass stripped increases, but only very slightly, as the resolution increases. In the high-resolution simulation the secondary lost almost $\sim 0.1\%$ more mass than in the low-resolution simulation. Second, as the resolution increases, the kick to the remainder of the secondary increases. The velocity of the center of mass follows the same overall profile, the only difference being a slight increase of 1.1% in the terminal velocity. An increase in momentum transfer with higher resolution was noted by Taam & Fryxell (1984). They attributed this trend to a more accurate description of the momentum transfer in the outer layers of the star, where the shock energy is deposited, because of the steep density gradient there. Third, as the resolution increases, the velocity of the stripped material systematically shifts to slightly lower velocities. The velocity at the half-mass point shifts from 861 km s^{-1} to 848 km s^{-1}. If with higher resolution the transfer of momentum to the remainder of the secondary is more efficient, then less momentum is available for the stripped material. Apart from the subtle systematic shift as the resolution changes, the features in the moderate-velocity region ($1000 - 3000$ km s^{-1}), which we associate in §4.1 with the composition transitions in the supernova ejecta, vary in position and amplitude. However, the velocity distributions of the low- and

high-resolution calculations show the same overall profile, especially at the low- and high-velocity tails. Above 3×10^3 km s^{-1}, the low-resolution distribution has 12% more mass than the high-resolution simulation. To reprise, as the resolution increases, the amount of stripped mass and the kick imparted to the secondary increase slightly, and the half-mass velocity of the stripped material decreases slightly.

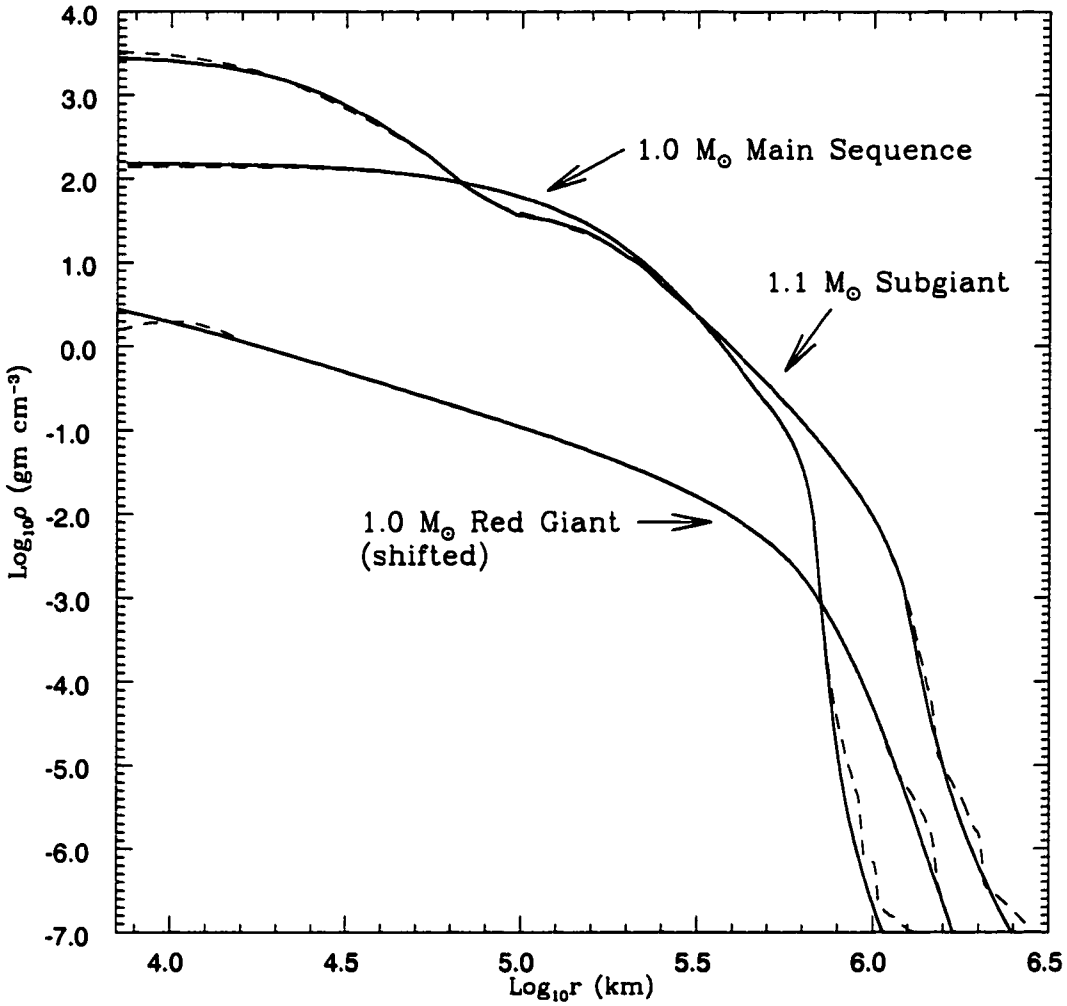

Figure 2.1 Hydrostatic equilibrium tests for the 1.0 $M_\odot$ main sequence star, the 1.1 $M_\odot$ subgiant, and the 1.0 $M_\odot$ red giant secondaries. To show the red giant profile on the same plot, we shift it to the left 100 km and upwards by 10^4 gm cm^{-3}. The solid lines show the initial density profile. The dashed lines for the main sequence and subgiant cases show the density profile 3 sound crossing times later, while the dashed line for the red giant shows the density profile 1 sound crossing time later.

CHAPTER 3

STANDARD TYPE IA SUPERNOVA BINARY SCENARIOS

A Type Ia supernova could be the product of a merger of CO white dwarf with a He or CO white dwarf (double-degenerate scenario), or the explosion of a white dwarf which has reached its Chandrasekhar mass by accreting hydrogen or helium from a nondegenerate companion (single-degenerate scenario) (Iben & Tutukov 1984). These two competing binary scenarios originate from very different evolutionary paths and naturally have different predictions for the Type Ia supernova rates. Binary population synthesis, a statistical tool for exploring the possible phases of binary evolution, can be used to estimate rates for progenitor scenarios to discriminate between progenitor models (cf. Iben & Tutukov 1984; Tutukov et al. 1992; Branch et al. 1995). However, the Type Ia supernova rates from population synthesis calculations suffer from serious uncertainties. Common envelope evolution is not well-understood. It is parameterized by α_{CE}, the efficiency with which the orbital energy is used to eject the common envelope, whose value is uncertain. The realization frequencies are dependent on the stellar population and age. Another complication arises from the different models for the thermonuclear explosion of the white dwarf. In a Chandrasekhar explosion (the standard model), the CO white dwarf accretes material until it approaches

the Chandrasekhar mass and carbon ignites in the center (Woosley & Weaver 1986). In sub-Chandrasekhar explosions, the ignition occurs in a helium layer around the CO white dwarf before the Chandrasekhar mass is reached (Nomoto et al. 1982). In general, binary population synthesis calculations favor the double-degenerate scenario over the single-degenerate scenario (Branch et al. 1995). Recent calculations by Branch et al. (1995) for a young population (10^8 yr) find double-degenerate rates of $\sim 10^{-3}$ yr^{-1}. This is closer to the current galactic Type Ia supernova rate of 4.0×10^{-3} yr^{-1} than the rates of $10^{-4} - 10^{-6}$ yr^{-1} for each of the many possible single-degenerate scenarios. But, for an older population (10^{10} yr) the double-degenerate rate drops to $\sim 10^{-4}$ yr^{-1} which can be matched by the realization frequency for symbiotic systems, a single-degenerate scenario in which the white dwarf accretes hydrogen from the wind of its red giant companion. Likewise, Ruiz-Lapuente (1996) finds that for an Sb galaxy the double-degenerate rate is $\sim 10^{-4}$ yr^{-1}, but that several single-degenerate scenarios have rates similar to this. Because of the complexity of the population synthesis calculations, it is difficult to exclude any Type Ia progenitor scenario outright just on the basis of realization frequencies. The presence of hydrogen in Type Ia supernova spectra is a stronger indication of a single-degenerate progenitor system because any Type Ia explosion in a double-degenerate binary system is expected to be hydrogen-free. In this paper, we examine only the single-degenerate scenarios for Type Ia supernova explosions.

Single-degenerate Type Ia models can be coarsely subdivided (see Table 3.1) into Hydrogen Cataclysmic Variables (H CV), Hydrogen Cataclysmic-Like Variables (H CVL), Symbiotic Stars (SS), Hydrogen Algols (H Algols), Helium Cataclysmic Variables (He CV), and Helium Algols (He Algols), based on the evolutionary stage of the secondary, method of mass transfer, and composition of

the secondary's envelope (Branch et al. 1995; Ruiz-Lapuente 1996). The secondary can be a low-mass main sequence, subgiant, or red giant star that slowly loses its envelope to the primary by Roche lobe overflow for close binaries or by stellar winds for wider binaries. The mass transferred can be hydrogen or helium in cases where the hydrogen layer has already been lost by earlier phases of mass transfer.

In the H CV scenario, a CO white dwarf, left in a close binary orbit by an earlier episode of common envelope evolution in its AGB phase, accretes hydrogen by Roche lobe overflow from a lower-mass main sequence secondary. The mass transfer is maintained by magnetic braking and has a characteristic rate of $\dot{M} > 1.0 \times 10^{-8}\ M_{\odot}\ \mathrm{yr}^{-1}$ (Verbunt & Zwaan 1981). Not all H CV systems end as Type Ia supernova progenitors. Only the largest white dwarfs with the highest mass transfer rates, high enough to suppress hydrogen flashes, can accrete enough mass to reach the Chandrasekhar mass. Livio & Truran (1992) associated these binaries with recurrent nova systems. When the Chandrasekhar mass is reached, the white dwarf explodes as a Type Ia supernova, but only if it can avoid accretion-induced collapse (Nomoto & Kondo 1990). Della Valle & Livio (1994) suggested these binaries could be responsible for Type Ia events in late-type galaxies while another progenitor from an older stellar population could be responsible for Type Ia events in early-type galaxies.

The H CVL systems have an evolutionary path like that of the H CV systems. After an episode of common envelope evolution, a white dwarf is left in a close binary orbit with a slightly higher-mass main sequence or subgiant secondary. Because of the mass ratio, the mass transfer is unstable and proceeds on a thermal timescale. This higher mass transfer rate ($\dot{M} \sim 10^{-6}\ M_{\odot}\ \mathrm{yr}^{-1}$) is responsible for the steady burning of hydrogen to helium on the surface of the white dwarf.

Eventually, the Chandrasekhar mass is reached and the star explodes (Rappaport et al. 1994; Hachisu et al. 1996; see also Hachisu et al. 1999b).

We use the H Algol and Symbiotic classification, following the path of Branch et al. (1995), as a general term to describe binaries in which the donor is a red giant that slowly loses mass to the white dwarf. In these scenarios, after a common envelope phase, a CO white dwarf is left in a binary orbit with a main sequence star. In the H Algol scenario, the main sequence secondary evolves all the way to the red giant phase before filling its Roche lobe for the first time (Whelan & Iben 1973; Iben & Tutukov 1984). Mass transfer to the white dwarf is by Roche lobe overflow, like the other Type Ia progenitor scenarios. In the symbiotic scenario, the red giant is too distant to fill its Roche lobe in the course of its evolution. Mass loss will occur by stellar winds. Many evolutionary paths can lead to the symbiotic scenario, the simplest being a wide binary whose stars evolve independently. Other possible paths include prior phases of common envelope evolution or conservative mass transfer during the primary's evolution, which leaves the binary separation too wide for the secondary to ever fill its Roche lobe (Yungelson et al. 1995). Until recently, symbiotics were considered as viable Type Ia candidates only for sub-Chandrasekhar explosions (Kenyon et al. 1993; Yungelson et al. 1995). However, recently Hachisu et al. (1999a) have proposed that symbiotic systems with Chandrasekhar explosions can account for the Type Ia rate.

The He CV and He Algol classes are analogous to the H CV and H Algol classes, the primary difference being that the mass transferred is helium instead of hydrogen. This complicated evolutionary path begins with the creation of a white dwarf in a close binary orbit, following a phase of common envelope evolution with a main sequence star, as in the previous scenarios. The secondary evolves

though the red giant phase. However, unlike the earlier scenarios, the secondary catastrophically loses its hydrogen envelope in another common envelope phase. The secondary, now a helium star, continues to evolve. For the He CV scenarios, mass transfer begins when the helium star goes into Roche lobe overflow. Stable mass transfer ($q < 1$) is maintained by gravitational wave radiation and proceeds on a nuclear timescale. For these binaries, helium star masses are typically in the range of $0.3 - 1.0\ M_{\odot}$ and white dwarf masses are in the range of $0.6 - 1.0\ M_{\odot}$. These are Type Ia supernova Chandrasekhar and sub-Chandrasekhar explosions (Iben & Tutukov 1991). For the He Algol scenarios, mass transfer begins during the secondary's expansion to a helium giant. Mass transfer is quasi-stationary ($\mathrm{M}\sim 10^{-6}\ M_{\odot}\ \mathrm{yr}^{-1}$) with secondary masses in the range of $0.75 - 2.3\ M_{\odot}$ and with white dwarf masses in the range of $0.9 - 1.4\ M_{\odot}$. The He Algol systems are candidates for Type Ia Chandrasekhar explosions (Iben & Tutukov 1994). Branch et al. (1995) finds that the realization frequencies for these scenarios are $10^{-4} - 10^{-5}$ yr^{-1} for young populations and are negligible for old populations.

In this paper, we focus on exploring the supernova-secondary interaction for the four hydrogen-rich scenarios in Table 3.1. To simulate each impact, we select a representative binary system from the literature for each of the four scenarios and estimate the binary separation and the companion's mass at the time of explosion. We use a stellar model in the simulation that is reasonably close in mass and evolutionary stage. We use either SNIa W7 (Nomoto et al. 1984) to represent a Chandrasekhar explosion or SNIa Hedt (Woosley & Weaver 1994, hedtb11) to represent a sub-Chandrasekhar explosion, depending on which is more likely for each binary scenario. The secondary models are listed in Table 3.2 with the masses and radii provided. Information on the supernova ejecta models is given in Table 3.3.

To represent the H CV class, we construct a prototype binary, based on the Type Ia supernova progenitor candidates of Livio & Truran (1992), consisting of a 1.0 $M_{\odot}$ main sequence secondary that lost 0.1 $M_{\odot}$ to a massive 1.3 $M_{\odot}$ white dwarf primary, allowing it to reach the Chandrasekhar mass. Assuming that the binary is in Roche lobe overflow at the time of explosion and that the secondary just fills its Roche lobe, from Eggleton's relation (Eggleton 1983) for $q = 1.0/1.4$ we estimate a binary separation of a $\sim$ 3R. For this simulation, we represent the secondary by a 1.0 $M_{\odot}$ solar model (Chaboyer 1998), the exploded white dwarf by the SNIa W7 (Nomoto et al. 1984) ejecta profile, and employ a binary separation of 3R.

We use the work of Li & van den Heuvel (1997) on supersoft X-ray sources as Type Ia supernova progenitor candidates to construct sample scenarios for both the H CVL and H Algol classes, one for each candidate proposed by Li & van den Heuvel (1997). Although H CVL binary systems have been included in the past as part of population synthesis studies (Rappaport et al. 1994), they are now the subject of renewed interest due to the suggestion by Hachisu et al. (1996) that a white dwarf fed by an optically thick wind can experience a much higher mass transfer rate than previously thought. Hachisu et al. (1996) have suggested that these binary systems are the progenitors of some supersoft X-ray sources, as well as potential Type Ia supernova progenitors, although the realization frequency is in dispute (Yungelson & Livio 1998).

As prototypes for our H CVL and H Algol classes, we select the two Li & van den Heuvel (1997) scenarios: the first scenario with a 2.5 $M_{\odot}$ subgiant companion and the second with a 1.0 $M_{\odot}$ red giant companion, prior to mass transfer. We represent the subgiant companion just prior to mass transfer with a 2.1 $M_{\odot}$ subgiant star having a radius of 2.3 $R_{\odot}$ (Chaboyer 1998). To simulate the

effect of binary mass transfer, which was not included when the star was evolved, we adjust the entropy profile to decrease the mass and radius of our secondary to 1.13 $M_{\odot}$ and 1.7 $R_{\odot}$, respectively, which reproduces the mass and radius of the secondary at the time of explosion as estimated from Li & van den Heuvel (1997). We do not attempt to reproduce the effect of the mass transfer on the red giant secondary. We represent the red giant companion with a 0.98 $M_{\odot}$ red giant with a radius of 170 $R_{\odot}$ (Chaboyer 1998). Because we can not include binary mass transfer in the stellar evolution code, our stellar models can not be exact recreations of the secondaries used in the binary evolution calculations of Li & van den Heuvel (1997). However, as we shall see, the stripped fraction and the velocity distribution of the stripped material are fairly robust and predictable.

To represent the Symbiotic (SS) class, we construct a prototype system based on the work of Yungelson et al. (1995), who concluded that symbiotic systems could be the progenitors of up to 1/3 of Type Ia events in young and intermediate age ($t \lesssim 6 \times 10^9$ yr) stellar populations. We select the same 0.98 $M_{\odot}$ red giant secondary as in the H Algol case, but to ensure that mass transfer takes place by stellar winds we increase the binary separation so that the red giant could not have filled its Roche lobe. Because these systems are good candidates for Type Ia sub-Chandrasekhar explosions, we select the ejecta model SNIa Hedt (hedtb11, Woosley & Weaver 1994) to represent the exploded white dwarf.

Table 3.4 lists the key simulations performed for this paper, with the stellar model, supernova ejecta model, and binary separation that were used in each simulation. The four simulations, representing the four hydrogen-rich classes of single-degenerate progenitor models, are labeled after their respective class as HCV, HCVL, HALGOLa, and SYMB. Additional calculations were performed

(HCVa, HCVb, HCVc, and HCVd) to gauge the trends with separation in the mass stripped, the kick, and the velocity distribution of the stripped hydrogen. We include a simulation using a 2.1 $M_{\odot}$ subgiant (HCVLa) secondary, which we compare to the HCVL simulation, whose secondary suffered substantial mass loss prior to the supernova explosion.

Our choice of reference binary scenarios is motivated in part by the likelihood that a particular progenitor can be responsible for a significant fraction of Type Ia events, and in part by the desire to cover the range of parameter space likely to be encountered by any Type Ia explosion in a single-degenerate binary system. We expect that the four binary scenarios HCV, HCVL, HALGOLa, and SYMB will cover the basic range of secondary stars, supernova explosion models, and binary separations expected for Type Ia supernova progenitors with a minimum of overlap. For example, the HCV, HCVL, and the HALGOLa simulations represent low-mass main sequence, subgiant, and red giant companions in Roche lobe overflow, in order to cover the range of compactness in the the evolution of a low-mass star. The mass profile of each secondary model is shown in Figure 3.1, and the binding energy profile is shown in Figure 3.2. The kinetic energy of the supernova blast is roughly 11, 10, 2300, and 1300 times the binding energy of the secondaries for the HCV, HCVL, HALGOLa, and SYMB simulations, the difference being the large difference in binding energy between the tightly-bound main sequence and subgiants and the loosely-bound envelope of the red giant. To explore the role of the supernova debris profiles, we employ two Type Ia models (see Table 3.3): W7, a standard Chandrasekhar explosion model, and Hedt, a sub-Chandrasekhar model with 78% of the momentum of W7. The HALGOLa and SYMB simulations represent the red giant companion with the same secondary model, but the HALGOLa simulation represents the supernova ejecta with W7.

The SYMB simulation represents the ejecta with Hedt at a slightly greater binary separation. Because the mass transfer is wind-driven, the solid angle subtended by the red giant in the SYMB simulation is therefore slightly smaller. The solid angle subtended determines the fraction of the supernova momentum incident on the secondary. For any low-mass companion in Roche lobe overflow the fraction of the sky subtended is typically $(1/4)(R/a)^2 \sim 1/36$ because a$\sim$ 3R, independent of the companion's stellar type.

Table 3.1. Single Degenerate Type Ia Models

Single Degenerate SNIa	Secondary	Mass Transfer
Hydrogen Cataclysmic Variables	Main Sequence/Subgiant	RLOF, H
Hydrogen Cataclysmic-Like Variables	Main Sequence/Subgiant	RLOF, H
Symbiotic Stars	Red Giant	Wind, H
Hydrogen Algols	Red Giant	RLOF, H
Helium Cataclysmic Variables	He Star	RLOF, He
Helium Algols	He Giant	RLOF, He

Table 3.2. Secondary Models

Evolutionary Stage	M ($M_\odot$)	R (km)	t_{dyn} (s) [a]	t_{cross} (s) [b]
Main Sequence	1.017	6.80×10^5	1.5×10^3	2.6×10^3
Subgiant	2.118	1.62×10^6	4.0×10^3	5.8×10^3
Subgiant, mass loss	1.132	1.22×10^6	3.5×10^3	5.5×10^3
Red Giant [c]	0.977	1.19×10^8	6.4×10^6	5.5×10^6

[a]Dynamical time, $t_{dyn} = \frac{1}{2}\left(G\langle\rho\rangle\right)^{-1/2}$

[b]Sound crossing time, $t_{cross} = R/\langle c_s \rangle$, integrated over star

[c]Softened $\phi(r) = -GM_c/(r + r_c)$, $M_c = 0.424\ M_\odot$, $R_c = 5 \times 10^5$ km

Table 3.3. Supernova Ejecta Models

Model	M ($M_\odot$)	E (10^{51} ergs)	P ($M_\odot$ V_c) [a]	$\langle V \rangle$ [b]	$V_{\frac{1}{2}M}$ [c]
SNIa W7 [d]	1.378	1.233	1.175	8.527×10^3	7.836×10^3
SNIa Hedtb11 [e]	0.899	1.079	0.912	1.014×10^4	1.006×10^4

[a]Momentum of supernova ejecta, specified in units of $M_\odot$ and divided by $V_c = 10^9$ cm s^{-1}

[b]Average speed of the supernova ejecta, km s^{-1}

[c]Speed of the supernova ejecta at the half-mass point, km s^{-1}

[d]Nomoto et al. 1984

[e]Woosley & Weaver 1994

Table 3.4. Simulations

Simulations		M ($M_\odot$)	a (km)	a/R	SN Model
HCV		1.017 (MS)	2.04×10^6	3.00	W7
	Additional Separations				
	HCVa	1.017 (MS)	1.75×10^6	2.57	W7
	HCVb	1.017 (MS)	2.72×10^6	4.00	W7
	HCVc	1.017 (MS)	4.08×10^6	6.00	W7
	HCVd	1.017 (MS)	8.16×10^6	12.00	W7
HCVL		1.132 (SG)	3.39×10^6	2.78	W7
	No Mass Loss				
	HCVLa	2.118 (SG)	4.50×10^6	2.78	W7
HALGOLa		0.977 (Red Giant)	3.00×10^8	2.52	W7
SYMB		0.977 (Red Giant)	3.76×10^8	3.16	Hedt

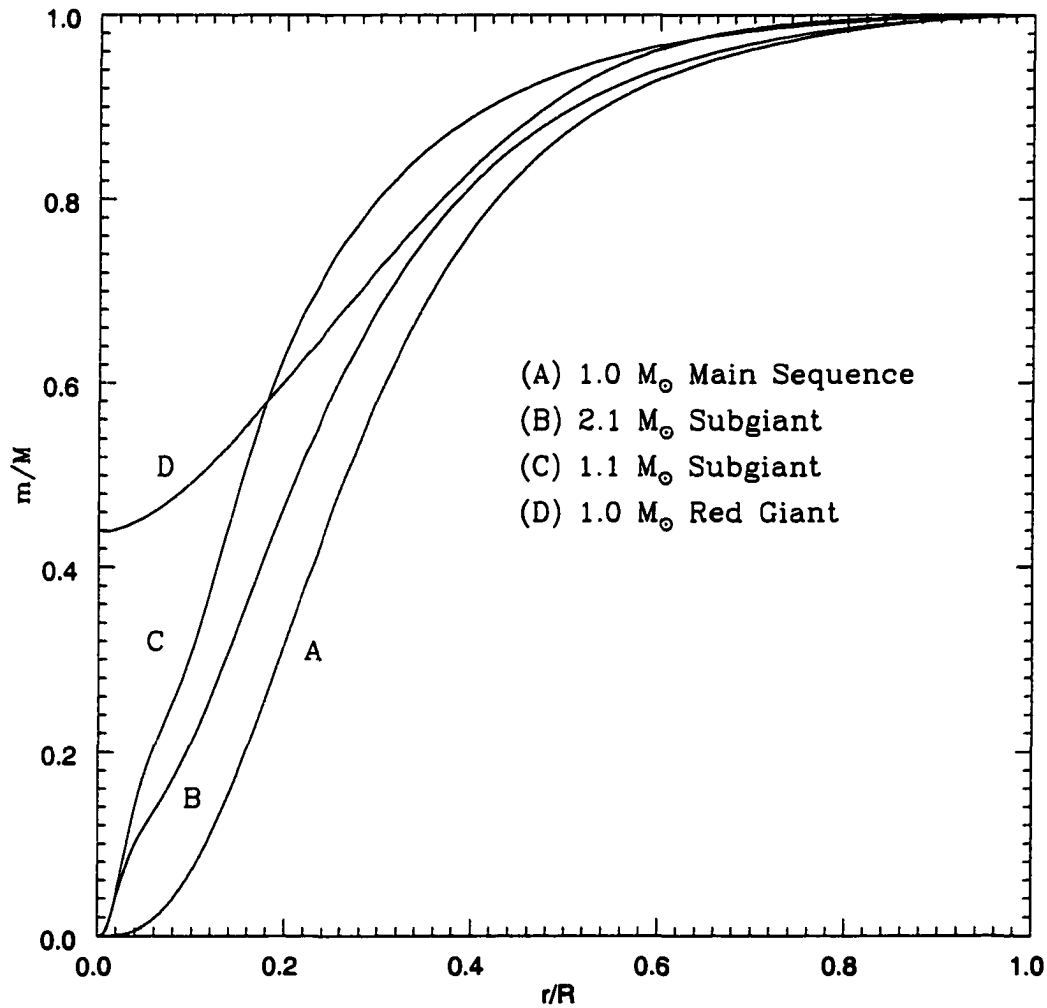

Figure 3.1 Mass vs. radius for the main sequence, subgiant, and red giant secondaries.

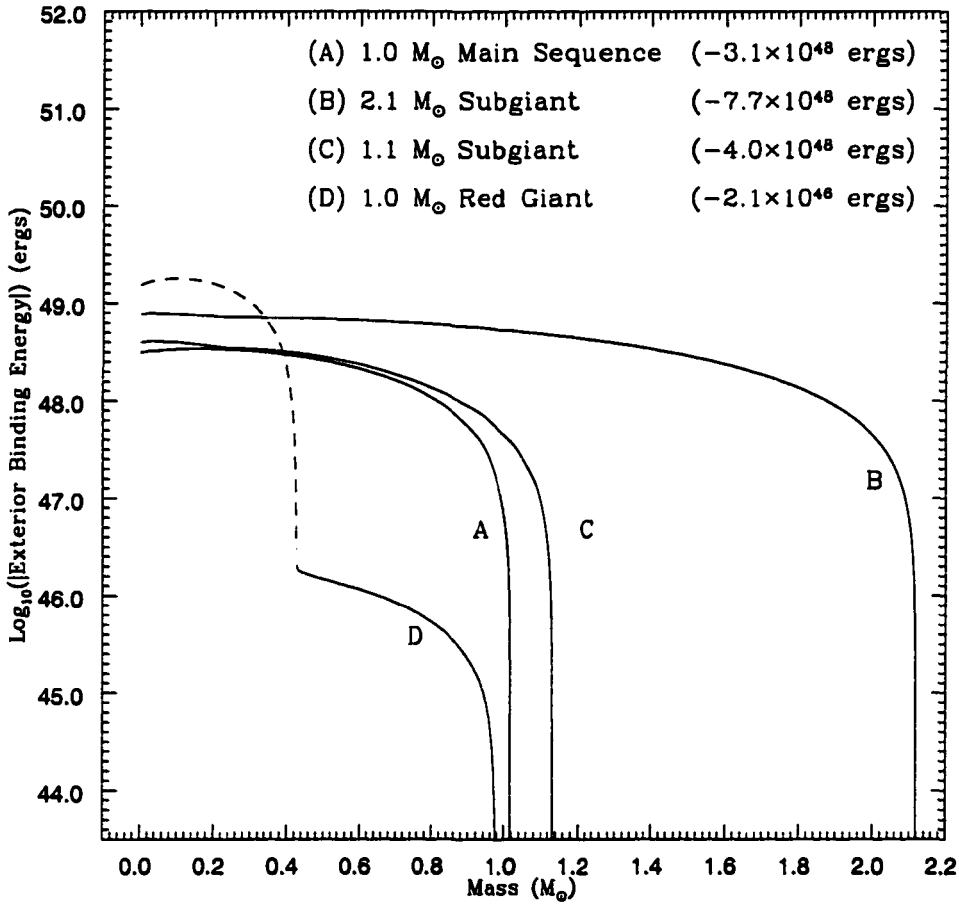

Figure 3.2 Absolute value of the exterior binding energy of the main sequence, subgiant, and red giant secondaries. The binding energy of each secondary is provided next to its legend. The value listed for the red giant secondaries is the binding energy of the envelope only. The dashed line indicates the binding energy profile of the red giant core.

CHAPTER 4

THE MAIN SEQUENCE COMPANION

In this section, we describe the impact of the blast wave on a main sequence star, our HCV scenario. As in the subgiant and red giant cases, we neglect any changes to the structure of the star from the Roche potential. Likewise, we do not add an accretion disk, magnetic field, or any other intrinsic features of cataclysmic variables which would introduce complications. For this simulation, we use a $300(\rho) \times 575(z)$ cylindrical grid with the 1.0 $M_{\odot}$ main sequence secondary, centered on the origin. Approximately $161(\rho) \times 322(z)$ zones are allocated to the secondary. The grid extends 6 stellar radii in the ρ direction, 12 stellar radii in the downstream (negative z) direction and 2 stellar radii in the upstream (positive z) direction. The white dwarf primary explodes just off the grid in the upstream direction, and the supernova debris flows through the upper boundary onto the grid by time-dependent boundary conditions. The density and velocity, which characterize the debris structure, energy, and momentum, are scaled with time: the Eulerian velocity as t^{-1} and the Lagrangian density as t^{-3}.

The HCV was run for 2.0×10^4 seconds, slightly more than 7 of the companion's sound crossing times and much longer than the 1.4×10^3 seconds that it takes for the trailing edge of the supernova to sweep past the back of the companion.

The length of the calculation is chosen to be sufficiently long, and the size of the grid sufficiently large, that we can follow the progress of the shock-heated material ejected from the companion in both velocity and solid angle and can construct a distribution for each. In addition, the long simulation time allows the companion star to begin to reestablish hydrostatic equilibrium. Although we can not follow the companion's Kelvin-Helmholtz evolution, its post-impact structure may provide us with some insight into the possible consequences of the impact for the companion's future evolution.

For clarity, this section is subdivided into distinct topics. In §4.1, we describe the debris structure of the impact, and in §4.2 we consider the consequences of the impact for hydrogen burning. In §4.3, we present and describe the stripped mass for this scenario. In §4.4, we qualitatively discuss the possibility that the main sequence companion may accrete supernova material and contaminate its envelope with heavy metals. In §4.5, we discuss the velocity and solid angle distributions of the stripped companion material and possible observational implications. In §4.6, we discuss the kick received by what remains of the companion.

4.1. Hydrodynamics of the Impact on the Main Sequence Companion

The impact of a blast wave on a main sequence star begins a sequence of events common to all supernova-companion interactions. The initial impact of the supernova shell on the surface of the star drives a shock into the stellar envelope. A reverse shock propagates back into the ejecta. A contact discontinuity marks the interface between the supernova ejecta and the shocked stellar material. The shock propagating through the envelope decelerates as it runs up the steep density gradient of the star. After the shock passes through the stellar core, it

accelerates down the decreasing gradient. The shock front, highly curved because of the density gradients, converges in the back of the star. The reverse shock develops into a bow shock around the companion star that smoothly deflects the rest of the incoming supernova debris around the companion. After most of the supernova debris has passed by, the outer layers of the stellar envelope, which have been shock-heated to such an extent that the new speed of sound exceeds the companion's escape velocity, are ejected, often corrugated by Kelvin-Helmholtz and Rayleigh-Taylor instabilities. The stripped material flows slowly away from the star, embedded within the inner layer of the supernova ejecta. The stellar core expands and cools in response to the initial compression by the shock. The star now has an extended, asymmetrical envelope and begins to pulsate to bring the envelope back into hydrostatic equilibrium. Figures A.1 - A.2 illustrate the sequence of the interaction in a series of 2-D images from the initial impact to the reestablishment of hydrostatic equilibrium. Figures A.3 illustrate the mass stripping of the companion in a series of 2-D cartoon images, with each color indicating the dominant element in that region.

Figure A.1a shows the companion centered at the origin of the cylindrical grid at the beginning of the simulation. Figure A.1b shows the initial impact of the blast at $\sim$ 100 seconds after the explosion. The supernova ejecta can be seen flowing onto the grid, sweeping up "circumstellar" material as the leading edge begins to flow around the secondary star. There is a region of high pressure at the site of the impact on the companion's surface where a shock is being driven into the star, and a bow shock is beginning to develop that will divert the flow of the supernova ejecta around the companion. The back of the companion is still undisturbed.

The density variations in the ejecta that are visible as spherical rings in Figure A.1b can be directly identified with the density variations in Figure 4.1 by their velocity. For example, the first strong ring striking the surface of the companion star in Figure A.1b has a velocity of 1.59×10^4 km s^{-1} and can be identified with the first sharp density spike in Figure 4.1. The second ring has a velocity of 1.36×10^4 km s^{-1} and can be identified with the second density spike in Figure 4.1. These features are associated with changes in the composition of the ejecta: the transitions between the "oxygen", "silicon", and "iron" layers. (see Figure A.3a).

Figure A.1c shows the impact 179 seconds after the explosion. The reflection shock and bow shock dominate this image. By this time, the collision of the supernova ejecta with the "circumstellar" medium has created a curved shock front which has converged along the downstream axis after flowing around the companion. The shock front reflects at the axis and begins to move outward. The reflection shock is visible in Figure A.1c as the flared vertical discontinuity along the downstream axis. The upstream axis is dominated by the bow shock which wraps smoothly around the top of the companion, but becomes distorted farther down as a consequence of the impact of the density variations of the ejecta. The material between the bow shock and the shocked surface of the star is primarily supernova debris mixed with "circumstellar" medium. The pressure in this region now rivals the pressure in the interior of the star (see Figure 4.2).

At 329 seconds (Figure A.1d), the shock front passing through the companion has a strong curvature caused by the density gradient of the star. The center of the shock decelerates as it encounters the rising density near the stellar core, while the wing of the shock accelerates through the back half of the companion where the density is decreasing. The shock-heated envelope of the companion starts to suffer

mass loss; escaping material is now visible in the flow that passes around the star behind the bow shock. Kelvin-Helmholtz and Rayleigh-Taylor instabilities in the shocked envelope are just barely visible in this image.

The ejected companion material is confined to a torus around the back of the companion - with the inside of the torus filled with "circumstellar" material that has been compressed behind the companion. There, the flow is almost directly parallel to the downstream axis (see Figure A.3c). This material is the first to be ejected from the star and is mixed with the oxygen layer of the supernova debris. This will form the high-velocity tail of the velocity distribution of the stripped companion material. In Figure A.3c, the iron shell has expanded to enclose the star, the silicon shell is just below the back of the star, and the oxygen shell is everywhere exterior to the silicon shell. More than 90% of the supernova's mass and momentum that will collide with the companion is now represented on the grid.

Figures A.2a and A.2b show the interaction at 529 and 755 seconds after the explosion (see also Figures A.3d and A.3e). By 529 seconds, the collision is effectively finished. Only a negligible mass and momentum will collide with the companion after this time. The shock within the companion has just passed through the stellar core and will begin to accelerate down the density gradient of the back of the companion. Kelvin-Helmholtz and Rayleigh-Taylor instabilities, the fingers of swirling material in the shocked envelope, are very visible by this time. As yet, only 0.07 $M_{\odot}$ has been ejected. By 755 seconds, the shock within the companion has converged along the downstream axis. In subsequent frames, a reflection shock can be seen progressing back through the remnant of the companion.

Figure A.2c shows the end of the mass stripping phase. By 2027 seconds, the star has expanded and pushed the bow shock back towards the site of the explosion. About 93% of the companion's mass that will be ejected has been ejected by this time. The velocity field around the star is now more spherical. This can be inferred from Figure A.3f by the change in the distribution of the stellar hydrogen, which is no longer confined along the downstream axis. About 1000 seconds later, the first in a series of shocks is driven into the envelope marking the beginning of a global stellar pulsation phase.

Figure A.2d shows the remnant after three oscillations, 2×10^4 seconds after the supernova explosion. The star is almost spherical again, but it is surrounded by a complicated system of shocks. The shock structures can be qualitatively explained in terms of the overtaking of each shock front by the subsequent shock front. Add to this mixture of shocks the reflected shock from the original shock through the companion, and the structure becomes difficult to disentangle.

Exactly what happens to the structure of the companion as the shock is driven through the star? To reliably follow the companion from the impact to the reestablishment of hydrostatic equilibrium, we ran a slightly different simulation, with the same binary scenario, but with a uniform grid and the gravity solver centered on the center of mass at each timestep, which is more suitable for long simulation times. Figures 4.2 - 4.4 show the evolution of the secondary's pressure profile from the beginning to the end of that simulation. Figure 4.2 shows the shock climbing the density gradient towards the stellar core. At $\sim$ 400 seconds, the shock passes through the stellar core and begins to descend down the density gradient. Also, as a result of the impact, a reverse shock is formed at the interface between the star and supernova that propagates back into the supernova material.

Eventually, the reverse shock becomes the bow shock.

As Taam & Fryxell (1984) discussed in their work on impacts on low-mass main sequence secondaries, the ram pressure of the ejecta is roughly equal to the central pressure of the main sequence secondary. The typical ram pressure of the ejecta is $P = \rho v^2 \approx M_{ej} v^2/(4\pi a^3/3)$, (N.B., a $\sim 3R$ when it hits a low-mass secondary in Roche lobe overflow). For our main sequence simulation this is $\sim 10^{17}$ dynes cm^{-2}, very close to the central pressure of 2.37×10^{17} dynes cm^{-2}. The ram pressure of the ejecta is close to the central pressure of the secondary only in the simulation with the main sequence companion. The more evolved subgiant and red giant have larger radii, which increases the binary separation and, thereby, decreases the incoming density and the ram pressure at first impact. For our subgiant and red giant secondaries, the expected ram pressures are roughly 10^{16} and 10^{10} dynes cm^{-2}, respectively, which is too low to significantly affect the subgiant's core by 2 orders of magnitude and the red giant's core by 7 orders of magnitude. In our HCV calculation, we find that the central pressure changes by a factor of only 2.5 as the shock passes through the core, which makes it a weak shock. The central density rises by only a factor of ~ 1.7, the temperature by ~ 1.5 and the entropy by 2.5 k_B^{-1} baryon^{-1}.

After the initial pressure rise, the star expands and the central pressure begins to drop. The shock accelerates down the density gradient in the back of the star until at ~ 700 seconds it passes through the limb of the star and converges on the downstream axis. Figure 4.3 illustrates the dramatic pressure rise at the back of the star as the curved shock fronts converge. The high back-pressure exerts a force on the secondary which decreases the kick received from the impact. As part of the shock-heated envelope escapes from the star, the back-pressure drops, until

after approximately 2000 seconds, the mass stripping phase is complete and the remainder of the secondary reaches its terminal velocity. At this stage, the star is slowly expanding. However, the passage of the shock and the ejection of part of the envelope begin a phase of radial pulsations during which shocks are sent out through the extended envelope. It is during this phase that the post-impact secondary recovers hydrostatic equilibrium.

Figure 4.4 shows the pressure profile from the end of the mass stripping phase to the reestablishment of hydrostatic equilibrium. As slow moving material begins to settle back onto the star, a bounce occurs ($\sim$ 4000 seconds) and a shock is driven into the outer envelope. Every $3000 - 4000$ seconds, roughly a sound crossing time, another pulsation with a smaller amplitude is seen moving through the extended envelope. Despite the dramatic appearance of the shocks in the extended envelope, little or no mass ejection takes place as a result. As shown in Figure 4.5, the stellar core also pulsates, with a period of $\sim$ 2600 seconds. In the last pressure profile shown in Figure 4.4, the central pressure has stabilized.

The changes in the central pressure, density, temperature, and entropy are listed in Table 4.1. All quantities but the entropy, which increases by shock-heating, have dropped significantly due to the expansion. Even after the interior of the star stops expanding and the infalling material compresses the core, the central pressure and density are not restored to their original values. Although such pulsations were not noted in earlier numerical simulations, probably due to much lower resolution and shorter simulation times, Taam & Fryxell (1984) did find that some of their low-mass main sequence companions suffered an abrupt rise in central density followed by a severe drop as the star began to expand. The density and entropy profiles of the pre- and post-impact companion are shown in Figures 4.6 and 4.7.

The radius of the remnant star, which we define as the radius that encloses about 90% of the remnant's mass, is approximately 7.4×10^5 km, a modest increase of less than 10%. The remaining 10% of the mass forms a low-density extended envelope out to 6.7×10^6 km ($\sim 10\ R_\odot$) with a composition similar to that of the original stellar envelope.

4.2. Quenching Hydrogen Burning in the Stellar Core

Do the abrupt rise and fall of the central temperature and density have any unique consequences for the energy generation rate and the luminosity of the companion during the impact? We expect that the energy generation rate, with its extreme temperature sensitivity, should rise and fall dramatically as the stellar core heats and cools. Figure 4.5 illustrates the rise and fall of the central temperature and density. The oscillations that the secondary experiences as hydrostatic equilibrium is reestablished are visible in both profiles. For a quick estimate of the energy generation rate, we calculate the hydrogen burning rate via the three pp chains and the CNO cycle (Clayton 1983; Kippenhahn & Weigert 1991) along a 1-D cut through the densest (and hottest) part of the companion. As can be seen in Figure 4.8, the energy generation rate shoots up by a factor of 1000 as a result of shock-heating, then drops precipitously as the star expands. Because the compression phase is so brief, despite the extremely high energy generation rate, only a small amount of additional energy is deposited in the center of the star. For the main sequence star an additional $\sim 10^{38}$ ergs has been deposited, which is extremely small in comparison with the binding energy of the star ($\sim 10^{48}$ ergs). However, because the timescale of the compression phase is close to the sound crossing time of the stellar core, the star may be able to expand and cool. Hence, 10^{38} ergs is an upper limit. By the end of the simulation, the energy generation

rate is only 0.07 $L_{\odot}$. The hydrogen burning has been quenched by the impact. The implications of this are discussed in §9.

4.3. The Stripped Mass of the Main Sequence Companion

The amount of mass stripped from the secondaries is shown in Table 4.2. The third column lists the stripped mass for each scenario based on the numerical calculation and the fourth column lists the stripped mass based on the analytic estimation of Wheeler et al. (1975). To determine the amount of material ejected by the impact and the passage of the shock through the star, we compare the velocity of the companion's material within each zone with its local escape velocity $\sqrt{2\phi}$, ϕ being the gravitational potential. If its velocity exceeds the escape velocity, we consider the mass unbound. If not, we consider the mass bound to the star, only displaced, although, because of the Eulerian nature of the code, we are not able to follow the calculation until the displaced stellar material falls back onto the companion. When any stellar material reaches the edge of the grid, we assume that if it is unbound at that time it will remain unbound. By the end of the simulation, 0.15 $M_{\odot}$ of the main sequence stars's envelope is unbound, and all but 2.4% of this material has left the grid. Although we run the simulation for 2×10^4 seconds, 93% of the stripped mass is ejected in the first 2×10^3 seconds, which is longer than the 1.4×10^3 seconds for the supernova to pass by the secondary.

Figure 4.9 shows the velocity distribution of all the stellar material $\sim 5 \times 10^3$ seconds after the supernova explosion. The distribution is clearly bimodal. The first peak indicates the distribution of the bound secondary and the second peak indicates the distribution of the stripped material. The vertical dashed line is the terminal velocity of the center of mass of the secondary, which we identify

with the kick received from the impact. Although the terminal velocity has been reached by this time, the secondary has not had time to reestablish hydrostatic equilibrium. The clearly bimodal distribution provides some comfort that our distinction between bound and unbound material is justified.

In Table 4.2 we compare the numerical stripped mass with an analytic estimate. The analytic estimate is within 10% of the numerical estimate, surprisingly close, although that changes as the binary separation increases. A detailed comparison of the numerical results with the analytic estimates is in §5. For now, we note that the analytic estimates do provide ballpark estimates of the stripped mass for the main sequence case. Because we use a smaller a/R ratio, consistent with Roche lobe overflow, our 0.15 $M_\odot$ of stripped material is substantially higher than the $0.013 - 0.052$ $M_\odot$ reported by Fryxell & Arnett (1981). However, we can compare our HCVc simulation to Fryxell & Arnett's CASE C, which has a similar a/R ratio, by scaling our stripped mass fraction by the new incident supernova momentum. After the scaling, our 0.022 $M_\odot$ of stripped material increases to 0.057 $M_\odot$ which is not inconsistent with the 0.052 $M_\odot$ they report.

4.4. Contamination of the Main Sequence Companion with Supernova Debris

It is possible that some supernova material may be mixed into the envelope of the secondary star, either as a direct consequence of the impact or as fallback. The enhancement of heavy elements in the atmosphere of the secondary star may be observable $10^3 - 10^4$ years (the Kelvin-Helmholtz timescale) after the impact or might change the course of the secondary's post-impact Kelvin-Helmholtz evolution by increasing the opacity of the stellar envelope. The question of how much

supernova material is likely to be accreted by the secondary star as a direct result of the explosion is of particular interest in connection with the overabundance of α-elements observed in the atmosphere of the secondary star in Nova Scorpii 1994 (GRO J1655-40) (Israelian et al. 1999). This binary X-ray source is believed to consist of a black hole primary in close orbit with a subgiant secondary. Israelian et al. (1999) have interpreted the anomalous abundances in the subgiant's atmosphere as contamination by fresh nucleosynthesis products ejected during a Type II supernova explosion that might have accompanied the formation of the black hole.

Our calculations imply that the stellar remnant is not contaminated by the supernova material as a direct result of the impact. At the end of our main sequence simulation, no significant amount of supernova material is within the original radius of the secondary. However, a trace amount ($1.3 \times 10^{-4}\ M_{\odot}$) of supernova material, predominately iron-rich ($\geq 90\%$) is bound by the secondary star, although the only supernova material in the immediate vicinity of the secondary star at the end of the main sequence simulation is physically located exterior to the bow shock. It is possible that the secondary may accrete this low-velocity iron and any additional iron mixed with the marginally-bound companion material when the displaced envelope, which is embedded within the iron layer of the supernova ejecta, begins to fall back. In addition, the slow trailing edge of the supernova ejecta could act as a source of iron-group elements long after the impact.

We can make a ballpark estimate of the amount of supernova debris that can contaminate the secondary star by finding the amount of mass of the supernova ejecta which can not escape the gravitational potential of the secondary. A typical escape velocity for a 1.0 $M_{\odot}$ main sequence star is $\sim$ 600 km s^{-1}. From the supernova ejecta model W7, we find that $\sim 1.5 \times 10^{-3}\ M_{\odot}$ has a velocity lower

than the escape velocity; we can use this as a crude and conservative upper limit for the degree of contamination.

4.5. Distribution in Velocity and Angle of the Material Stripped from the Main Sequence Companion

One of our key results is the velocity distribution of the stripped hydrogen material, shown in Figure 4.10, for the HCV simulation. Also plotted in this figure is the velocity distribution of W7, the supernova ejecta model. The first feature to catch the eye is the clear separation in velocity space between the stripped material and the supernova ejecta. The velocity at the half-mass point in the velocity profile of the main sequence secondary is 848 km s^{-1}, much less than the half-mass velocity of the supernova ejecta of 7836 km s^{-1}. Each half-mass velocity is marked with a vertical line and an arrow in Figure 4.10. The high-velocity tail shows three sharp spikes (clearly seen in Figure 4.11), which we identify with the three sharp density peaks at the composition transitions in SN W7. The composition groups for both the stripped material and supernova are shown; from this, it is clear that the bulk of the stripped material, predominately hydrogen, is embedded within the iron layer of the supernova ejecta. This result reinforces the belief that contaminating hydrogen and helium are most likely to be observed as late-time emission when the photosphere of the supernova moves to low-velocities, revealing the core. However, a high-velocity tail does exist, implying that a trace of companion hydrogen is swept up in the oxygen and silicon layers of the supernova ejecta. Given the upper limits on the hydrogen abundance from Type Ia observations near maximum light, this may provide a criterion for discriminating between Type Ia progenitor scenarios.

The sharp edge on the low-velocity side of the profile, unfortunately emphasized when dM/dV is used as the ordinate, marks the division between the stripped and the bound material. In reality, very little mass is associated with the low-velocity tail, as can be seen in Figure 4.12, which shows the same HCV profile as Figure 4.10 with VdM/dV as the ordinate. We can correct the low-velocity tail by allowing the stripped material to escape to infinity, free of the secondary's gravitational potential. If we assume the stripped material flows off the grid at high-Mach numbers (typically M$\sim$ 5 – 30), then the specific enthalpy $w = c_s^2/(\gamma - 1)$ is small in comparison with the kinetic energy, and we can neglect the enthalpy in Bernouilli's Equation $w + 1/2v^2 + \phi = C$, where C is a constant along a streamline. Therefore, we can estimate the velocity of the flow at infinity as $v_\infty^2 = v^2 - v_{esc}^2$. The asymptotic distribution would resemble the profile shown in Figure 4.11, where we have subtracted in quadrature a typical escape velocity $v_{esc} = \sqrt{2GM/r}$, with M $\sim$ 1 $M_\odot$ and the characteristic distance (r) is 12R, a typical grid size. The subtraction in quadrature affects only the low-velocity tail.

Figures 4.13 and 4.14 show the spatial distribution of the stripped mass. Figure 4.13 illustrates the distribution of the stripped material in solid angle (dM/dΩ) in the HCV simulation, expressed in terms of the angle, α, from the downstream axis. The half-mass point of the HCV distribution is $\sim$ 43°, so about half of the stripped material is confined in a cone within about $\sim$ 43° of the downstream axis and the other half extends out to $\sim$ 90°. The sudden rise along the axis for the HCV distribution is a consequence of the use of the differential element $d\Omega = 2\pi \sin\alpha d\alpha$ when $\alpha \to 0$. Figure 4.14 illustrates the same spatial distribution as a polar plot. The polar angle, α, once again represents the angle from the downstream axis, and the radial coordinate represents the magnitude of $dM/d\alpha$. The profile clearly shows that the preferred direction is along the 43° line. In addition, the majority of the

mass is exterior to the geometrical shadow, the shadow that the secondary would cast from the site of the explosion of the primary. Because of the compression of the "circumstellar" material along the downstream axis as the supernova sweeps around the star, very little stripped material is directly behind the secondary. In a 3-D calculation instabilities along the downstream axis are likely to mix the compressed "circumstellar" material with the stripped stellar material, filling in this region.

As shown in Figure 4.13, the collision of the supernova debris with the secondary will create a hole in the debris structure. The highest velocity debris will flow around the secondary, creating a cut-out region. The lower velocity material will flow around the bow shock, creating a wider hole in the inner ejecta. For the HCV simulation, the supernova debris will have a hole of $\sim 31°$ in the outer ejecta, which will widen to $\sim 40°$ in the inner ejecta. This corresponds to 7% and 12% of the surface of the supernova ejecta. Due to the supersonic nature of the flow, the hole will not close with time. Hence, the asymmetry in the supernova remnant may indicate the presence of a secondary star.

If the stripped hydrogen were ejected spherically and uniformly mixed with the (unperturbed) supernova ejecta, then the mass fraction of hydrogen would be 0.6 to 0.7, almost solar, in the low-velocity region ($\lesssim 10^3$ km s^{-1}). The hydrogen mass fraction, X(H), is shown as a function of supernova mass and velocity in Figures 4.15 and 4.16. The hydrogen mass fraction falls abruptly as the velocity increases. At 10^4 km s^{-1}, which is near the oxygen and silicon layers, X(H)$\sim 3 \times 10^{-3}$. Of course, we know from the numerical simulation that the ejected material contaminates a wide solid angle behind the secondary. For the HCV simulation, 90% of the stripped hydrogen lies within 65.7° of the downstream axis which

corresponds to a fractional solid angle of 29%. Figures 4.15 and 4.16 show the expected mass fraction within the contaminated solid angle. As expected, the mass fraction rises dramatically.

4.6. The Kick Received by the Main Sequence Companion

Table 4.3 lists the kicks given to the remnant companions in the main sequence and subgiant scenarios. We note that the red giant core, because of its extremely small size, receives a negligible kick. We calculate the kick from the supernova impact by finding the terminal velocity of the center of mass of the unstripped stellar material that remains on the grid. Although some material still bound to the star can flow off the grid, it is a negligible fraction ($\Delta M/M \leq 10^{-2}$), since the star reaches its terminal velocity very early in the simulation. For the main sequence simulation HCV, the companion receives a kick of ~ 86 km s^{-1}. Although substantial, this is still much less than its 227 km s^{-1} orbital velocity.

Figure 4.17 shows for the main sequence simulations the velocity of the center of mass of the companion for the first 5000 seconds after the explosion. Clearly, the terminal velocity is reached for all the simulations by 5000 seconds. In the HCV simulation the secondary receives a very strong kick (> 100 km s^{-1}) in the first ~ 500 seconds as the shock passes through the center of the companion. As the shock converges and reflects in the back half of the companion (~ 700 seconds), the pressure rises dramatically, and the companion, now elongated, decelerates. By 1500 seconds, part of the shock-heated envelope has escaped the star and the over-pressure behind the star begins to drop. As the mass-stripping phase nears completion, the companion is almost spherically symmetric and close to its terminal velocity.

Column three in Table 4.3 provides our ballpark estimate of the kick that we calculate by assuming an inelastic collision in which all the momentum of the supernova ejecta incident on the remnant of the companion is directly transferred to the remnant. That is, using $\Delta\Omega_{REM}$ and M_{REM} as the solid angle subtended by the remnant and the mass of the remnant, and M_{SN} and V_{SN} as the mass and velocity of the supernova ejecta, respectively, we estimate the kick as $v \lesssim \Delta\Omega_{REM} M_{SN} V_{SN} / M_{REM}$. This is clearly an overestimate because not all of the momentum will be directly transferred to the remnant. The momentum transferred to the remnant will depend on the details of the interaction, such as the changing geometrical area as mass loss decreases the surface area of the companion. Our estimate is directly related to the method of Wheeler et al. (1975), except that we drop the logarithmic factor because it was concluded (Fryxell & Arnett 1981; Taam & Fryxell 1984) that including ablation overestimated the momentum transfer.

Table 4.1. Pre- and Post-Impact Central Values for HCV Companion

	Initial	Final	Fractional Change
Pressure (dynes cm^{-2})	2.34×10^{17}	9.41×10^{16}	0.60
Density (gm cm^{-3})	1.54×10^{2}	7.95×10^{1}	0.48
Temperature (K)	1.56×10^{7}	9.68×10^{6}	0.38
Entropy (k_b^{-1} $baryon^{-1}$)	1.10×10^{1}	1.35×10^{1}	0.23

Table 4.2. Stripped Mass

Scenario	Time (s)	ΔM $(M_\odot)^a$	ΔM $(M_\odot)^b$
HCV	2.0×10^4	0.15	0.16
HCVa	2.0×10^4	0.23	0.20
HCVb	2.5×10^4	0.074	0.11
HCVc	3.0×10^4	0.022	0.063
HCVd	3.0×10^4	0.0018	0.021
HCVL	3.0×10^4	0.17	0.14
HCVLa	3.0×10^4	0.25	0.21
HALGOLa	6.0×10^6	0.54 (98%)	0.55 (100%)
SYMB	8.0×10^6	0.53 (96%)	0.55 (100%)

[a]Numerical Calculation of Stripped Mass

[b]Analytic Estimate of Stripped Mass, method of Wheeler et al. 1975

Table 4.3. Kicks

Scenario	M_{rem} $(M_\odot)$ [a]	V_{rem} [b]	V [c]	V_{orb} [d]	P_{rem}/P_{in} [e]
HCV	0.867	85.7	109.8	227.1	0.228
HCVa	0.787	99.2	137.1	245.2	0.176
HCVb	0.943	61.5	73.2	196.7	0.316
HCVc	0.995	35.2	41.7	160.6	0.429
HCVd	1.015	10.1	14.8	113.5	0.503
HCVL	0.962	49.4	70.4	172.1	0.125
HCVLa	1.868	54.4	65.4	126.5	0.267

[a]Numerical Calculation of the Mass of the Stellar Remnant

[b]Numerical Calculation of the Kick of the Stellar Remnant, km s^{-1}

[c]Ballpark Estimate of Kick from Inelastic Collision, km s^{-1}

[d]Orbital Velocity, km s^{-1}

[e]Ratio of Stellar Remnant Momentum (P_{rem}) to Incident Supernova Momentum (P_{in})

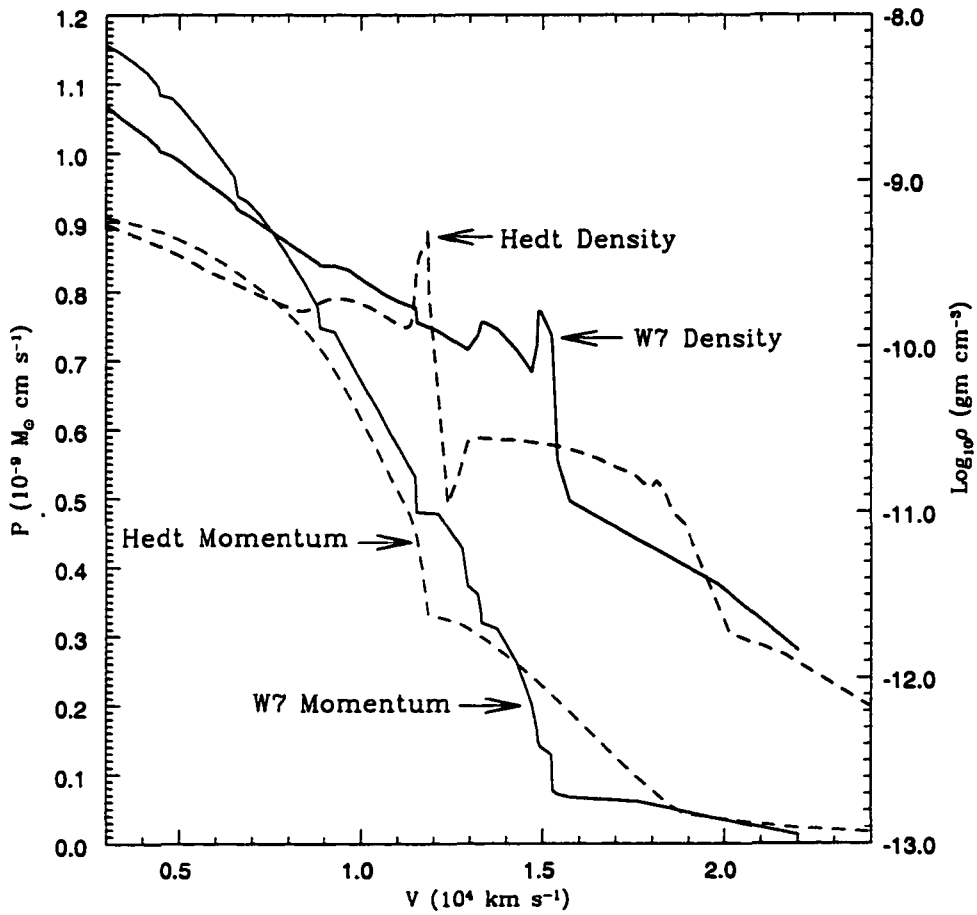

Figure 4.1 Momentum and density profile of SNIa W7 and SNIa Hedt. SNIa W7 is shown at 24 hrs while SNIa Hedt is shown at 27.87 hrs.

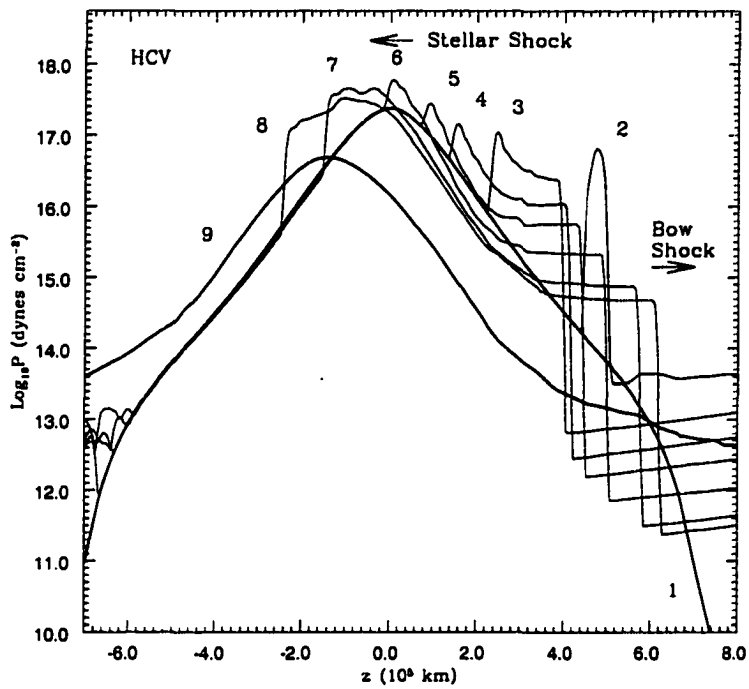

Figure 4.2 Pressure profile of the initial impact on the main sequence secondary (HCV) along the z axis, illustrating the propagation of the shock through the stellar core and the development of the bow shock. The profiles shown are at 29, 104, 179, 257, 332, 451, 601, 676, and 2030 seconds after the explosion and are labeled 1-9, respectively. The first and last timesteps are marked by thicker lines. They represent the undisturbed companion and the companion after the mass stripping is complete and are included for reference.

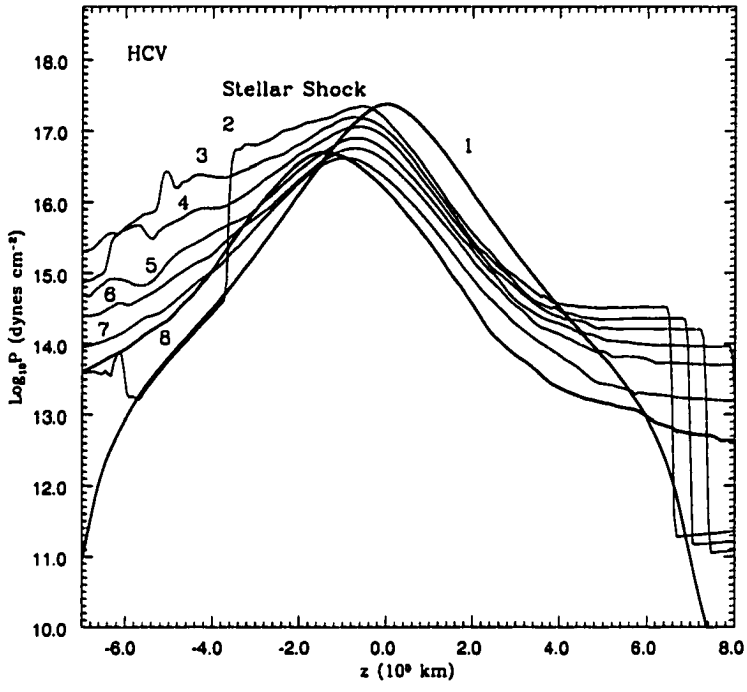

Figure 4.3 Pressure profile of the main sequence secondary (HCV) along the z axis, illustrating the abrupt pressure rise in the back of the star as the stellar shock converges along the axis. As the shock-heated material is ejected from the star, the back pressure drops. The profiles shown are at 29, 751, 827, 902, 1026, 1178, 1528, and 2030 seconds after the explosion and are labeled 1-8, respectively. The first and last timestep are marked by thicker lines. They represent the undisturbed companion and the companion after the mass stripping is complete.

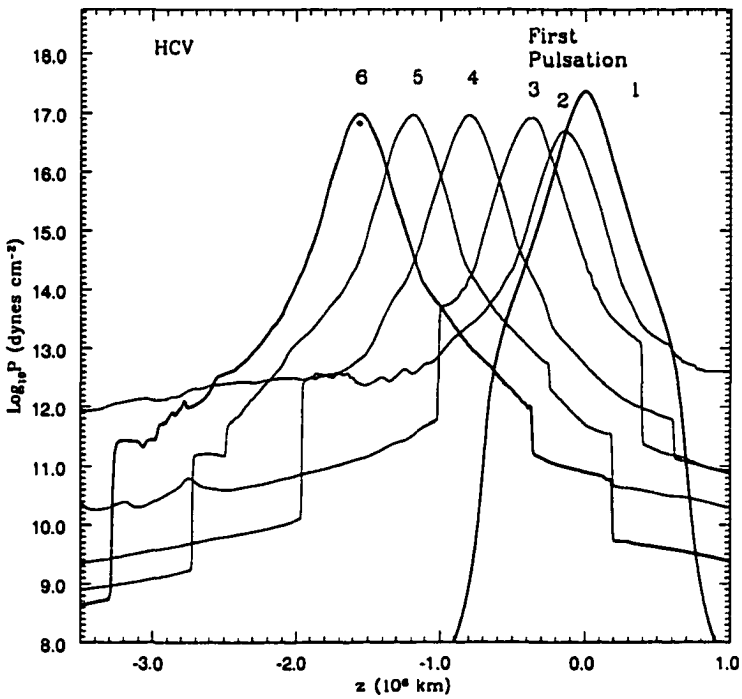

Figure 4.4 Pressure profile of the main sequence secondary (HCV) along the z axis as the star recovers hydrostatic equilibrium. The remnant is now moving down the axis with the kick received by the impact. The profiles shown are at 29, 2030, 5035, 10053, 15056, and 20032 seconds after the explosion and are labeled 1-6, respectively. The first and last timesteps are marked by thicker lines; they represent the undisturbed companion and the post-impact companion after several pulsations.

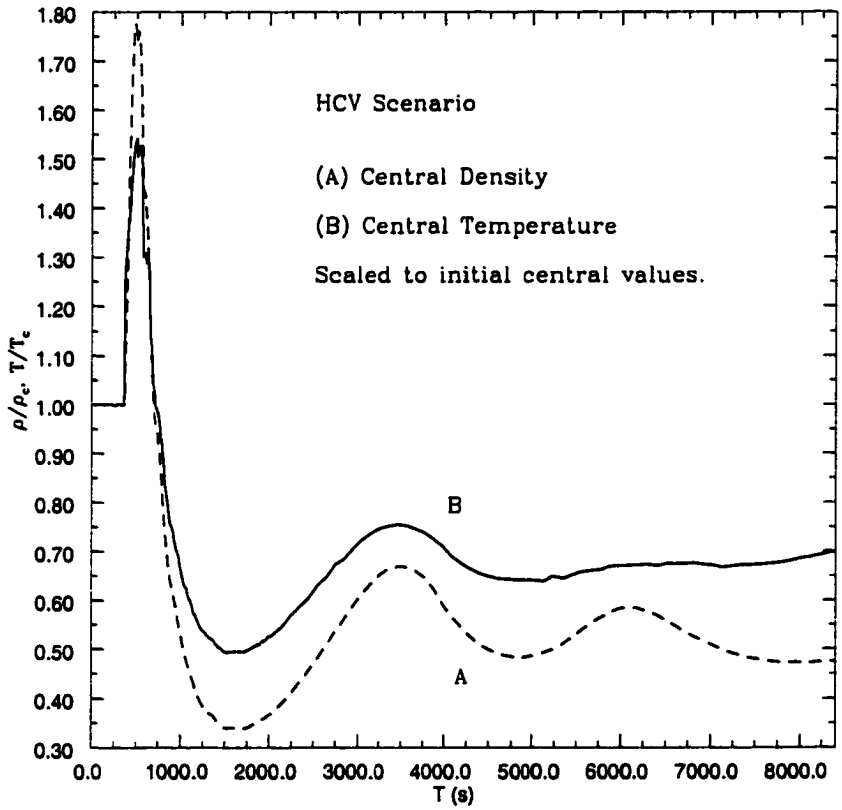

Figure 4.5 Central density and temperature as a function of time for the HCV scenario (1.0 $M_\odot$ secondary)

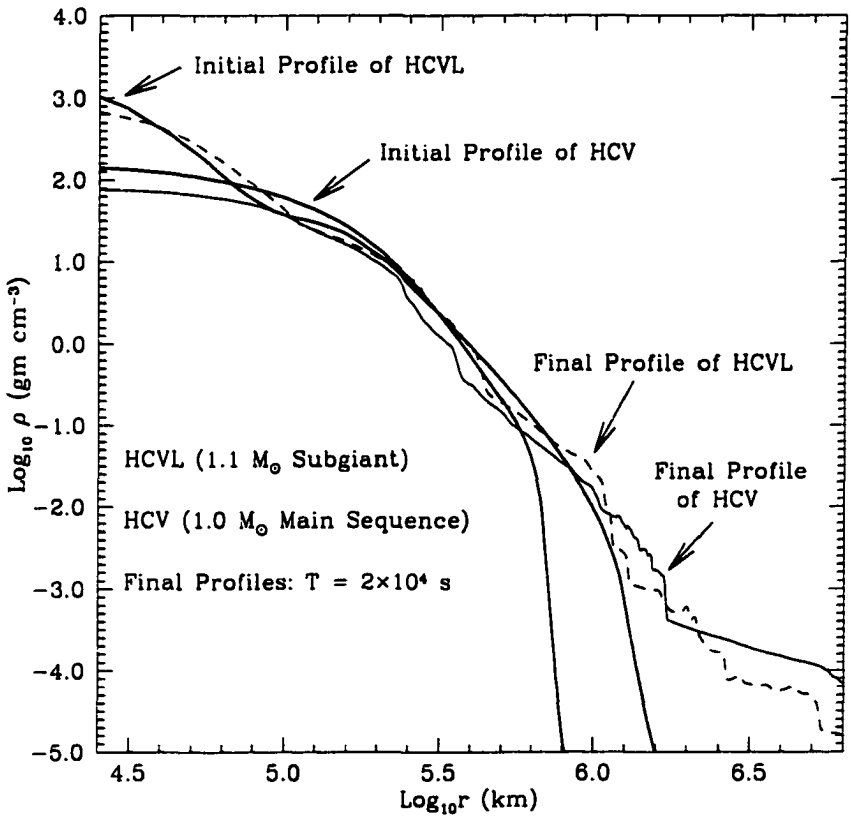

Figure 4.6 Pre- and Post-impact density profile of the the main sequence secondary (HCV) and the subgiant secondary (HCVL).

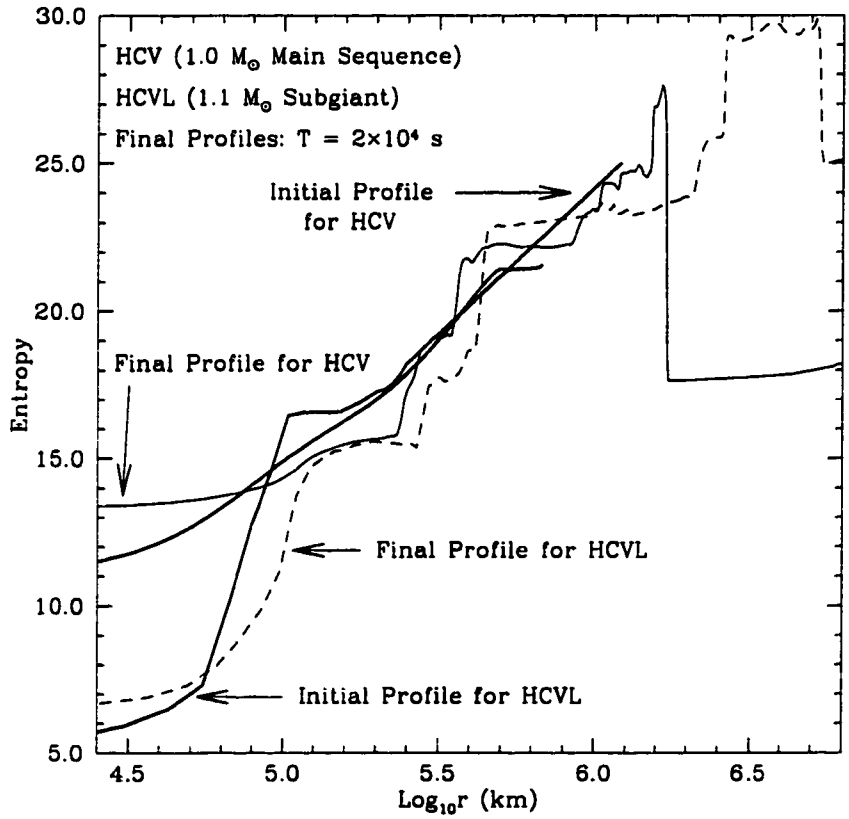

Figure 4.7 Pre- and Post-impact entropy profile (per Boltzmann's constant per baryon) of the main sequence secondary (HCV) and the subgiant secondary (HCVL).

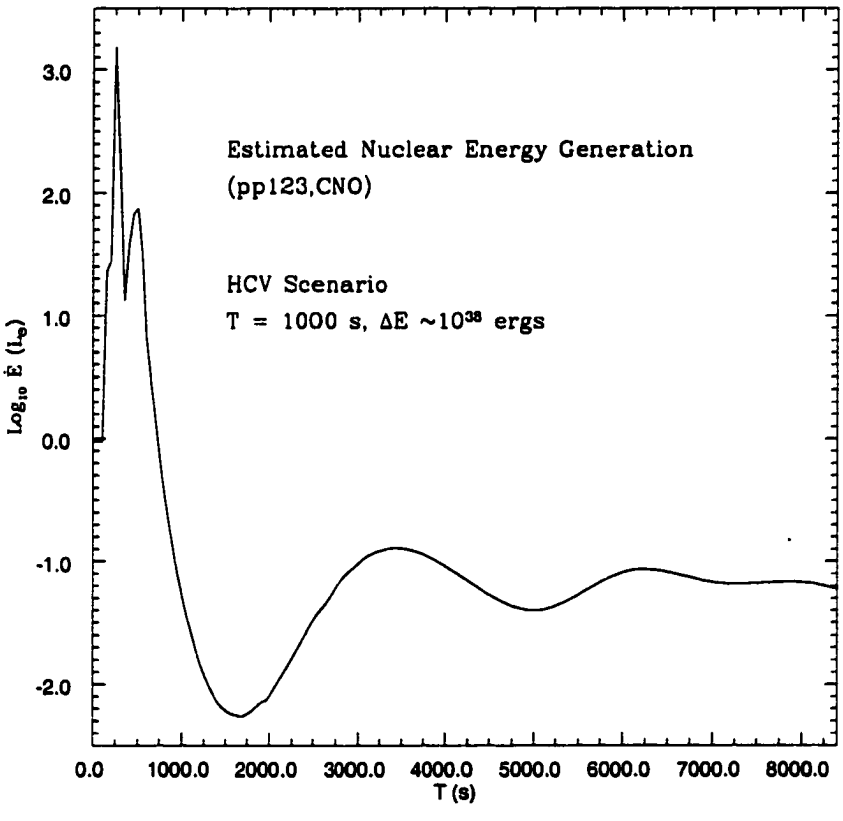

Figure 4.8 Estimate of nuclear energy generation from the pp chains and the CNO cycle for the HCV scenario (1.0 $M_{\odot}$ secondary) using a 1-D section with spherical symmetry. The compression and expansion of the stellar core releases $\sim 10^{38}$ ergs in the first 1000 seconds.

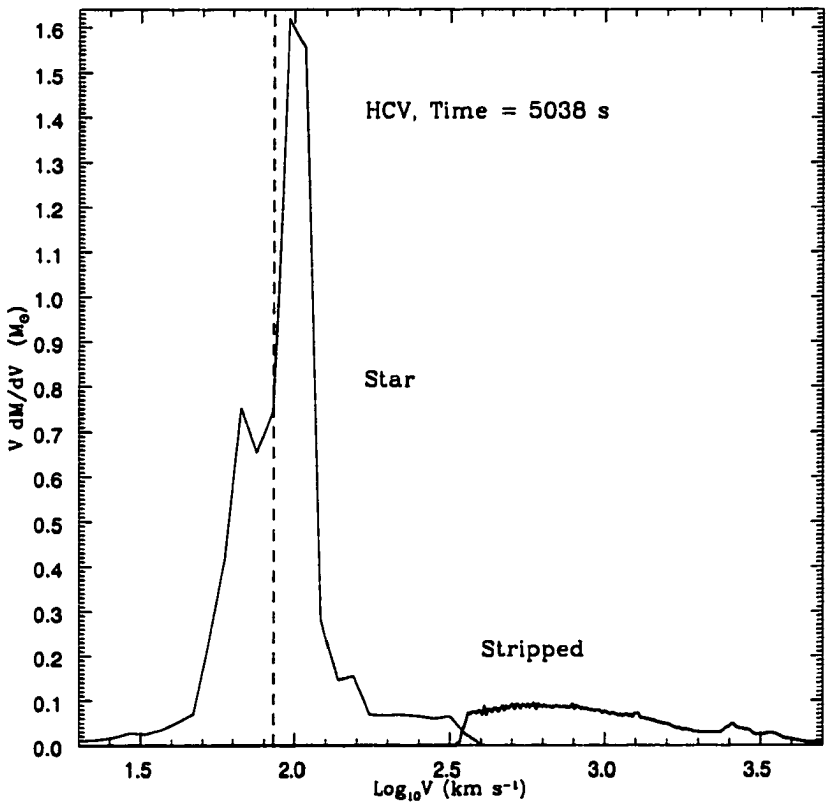

Figure 4.9 Velocity distribution of the stellar material for the HCV simulation at 5038 seconds after the supernova explosion. The solid line indicates the velocity distribution of the secondary. The dashed line indicates the velocity distribution of the stripped stellar material. The vertical dashed line indicates the kick received by the secondary.

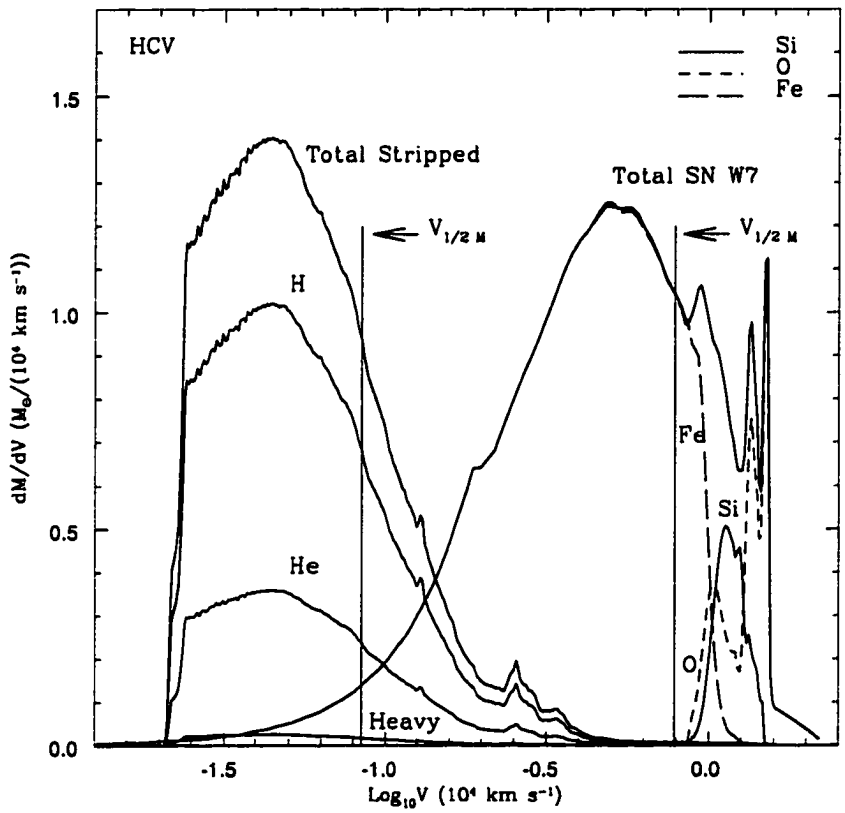

Figure 4.10 Velocity distribution dM/dV of the stripped stellar hydrogen and helium for the HCV binary scenario at the end of the simulation, along with the velocity distribution of SNIa W7. The velocity at the half-mass point of the HCV distribution, as indicated by the vertical line and the arrow, is 848 km s^{-1}. In contrast, the velocity at the half-mass point of the SN W7 distribution, also indicated in the plot, is 7836 km s^{-1}.

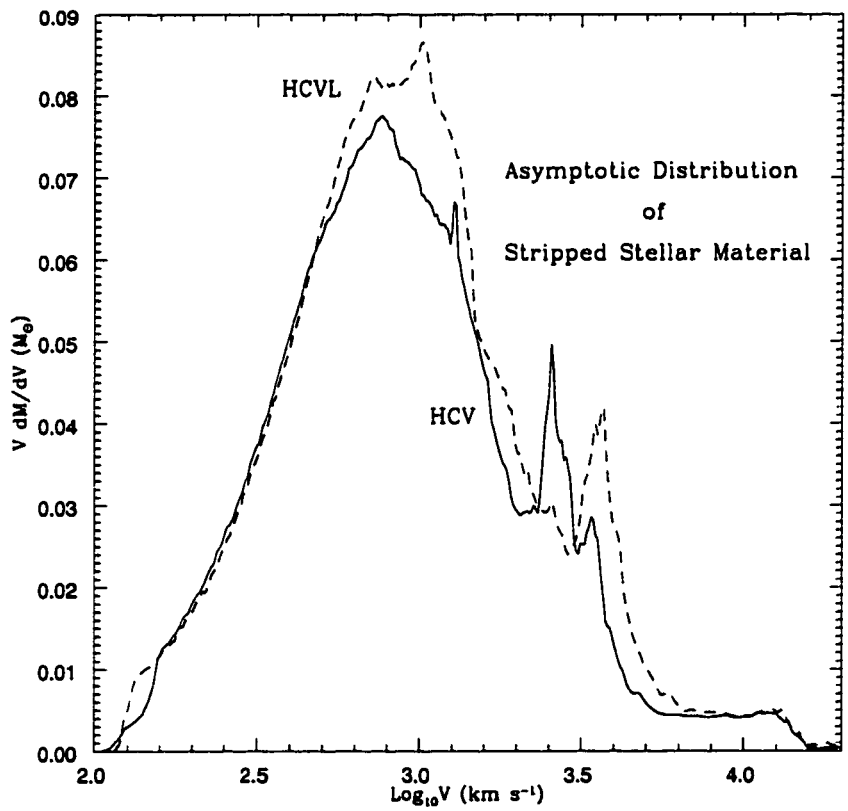

Figure 4.11 Estimate of asymptotic velocity distribution dM/dV of the stripped stellar material for the main sequence (HCV) and subgiant (HCVL) simulations after the stripped material escapes the the gravitational potential of the secondary star. The solid line indicates the main sequence simulation; the dashed line indicates the subgiant simulation. We calculate the profiles by subtracting in quadrature an estimate of the escape velocity as the stripped material leaves the grid.

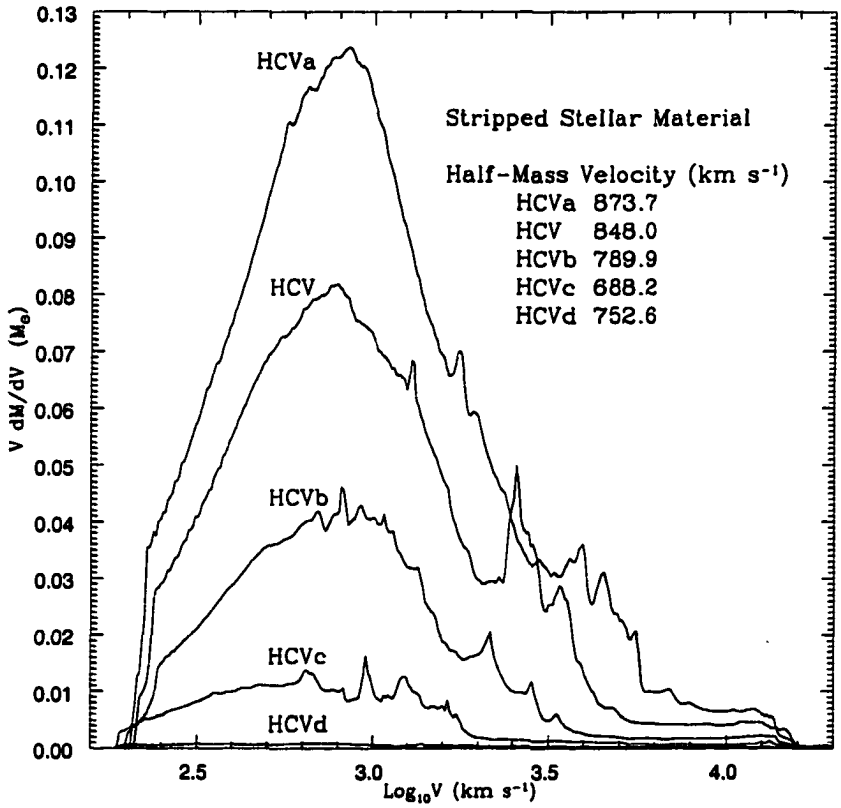

Figure 4.12 Velocity distribution of the stripped stellar material of the main sequence secondary for the HCV and test cases HCVa, HCVb, HCVc, and HCVd. The half-mass velocity of each distribution is listed.

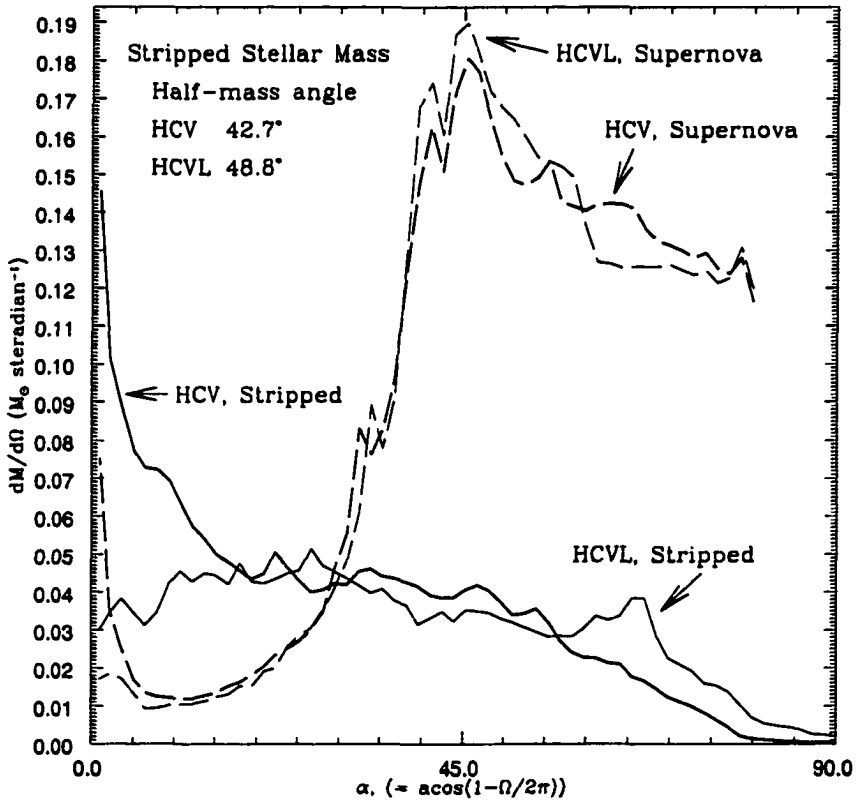

Figure 4.13 The solid angle distribution of the stripped envelope of the main sequence and subgiant simulations HCV and HCVL. The half-mass angle of each distribution is listed. The dashed lines indicate the distribution of supernova material for both simulations. The hole in the supernova debris created by the impact is visible between $0° - 40°$.

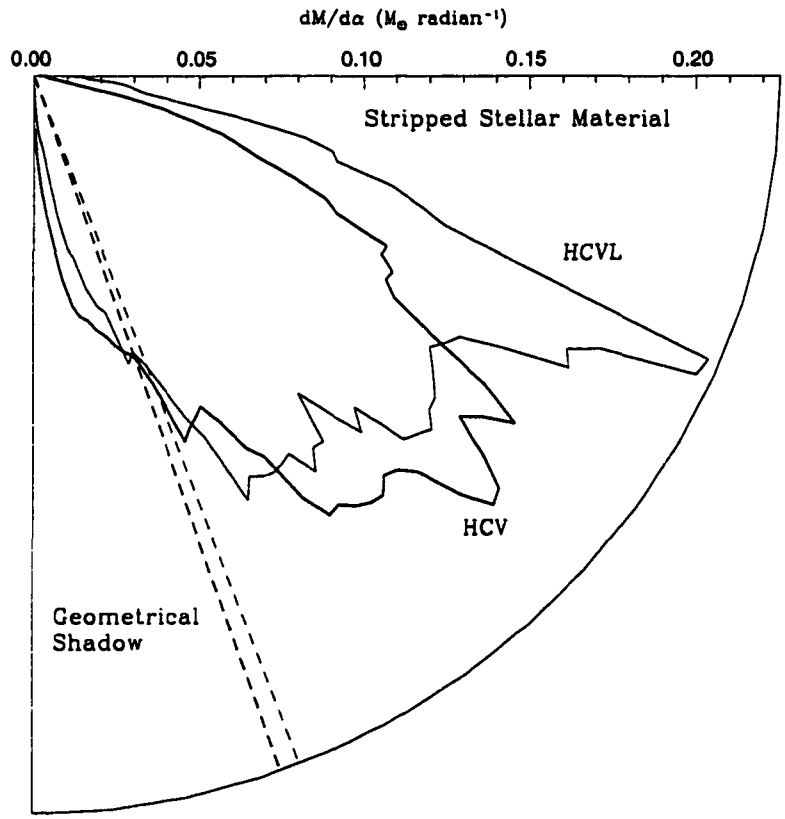

Figure 4.14 The magnitude of the angular distribution ($dM/d\alpha$) is plotted as the radial coordinate for the HCV and HCVL binary scenarios. The angular coordinate is the angle from the downstream axis. The geometrical shadow is shown for both simulations.

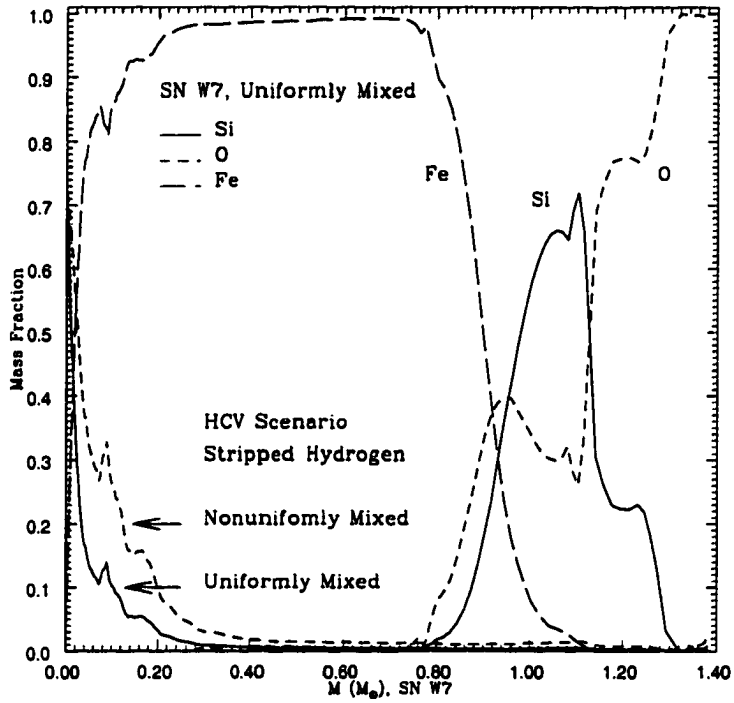

Figure 4.15 Hydrogen mass fraction of the contaminated supernova ejecta for the HCV scenario (1.0 $M_{\odot}$ main sequence secondary) vs. the mass of the original W7 supernova model. The solid line indicates the hydrogen mass fraction assuming that the stripped material is uniformly mixed in angle with Type Ia model W7. The mass fractions of the O, Si, and Fe-group elements are shown for comparison. Because the stripped material in this simulation contaminates only the supernova ejecta within 65.7° of the downstream axis, the dashed line indicates the hydrogen mass fraction assuming mixing only in this region.

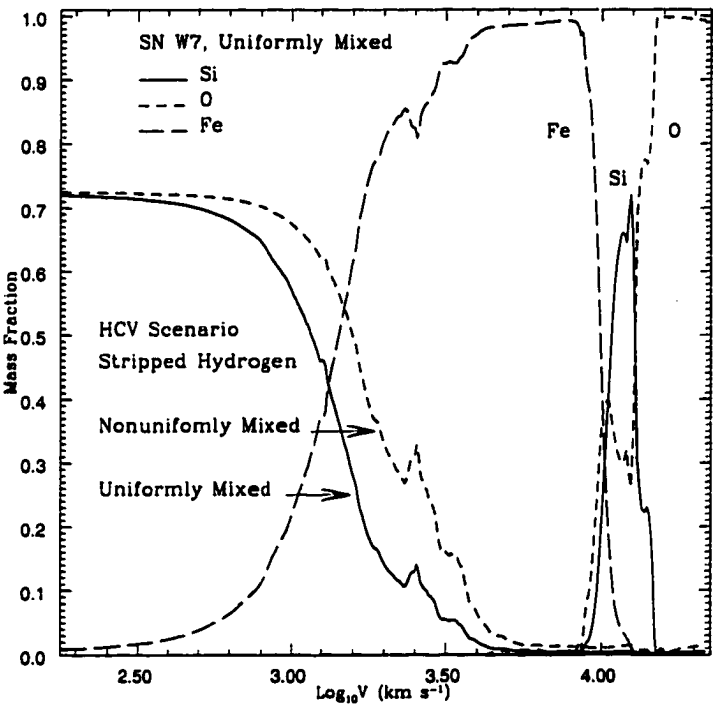

Figure 4.16 Hydrogen mass fraction of the contaminated supernova ejecta for the HCV scenario (1.0 $M_{\odot}$ main sequence secondary) vs. velocity. See the caption for Figure 4.15.

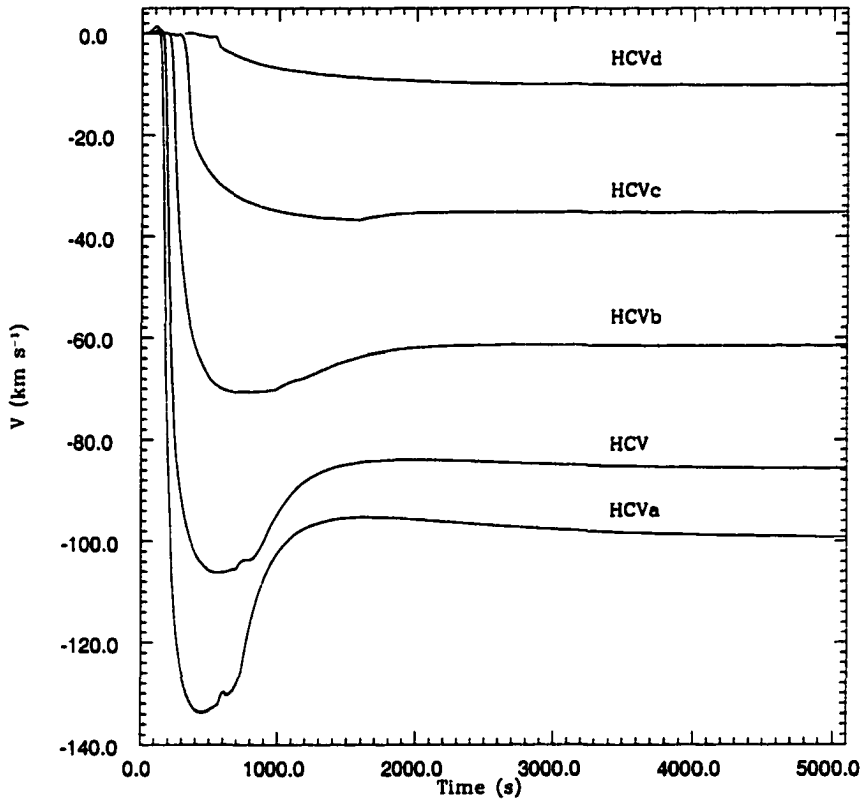

Figure 4.17 Velocity of the center of mass of the main sequence secondary for the HCV scenario and test cases HCVa, HCVb, HCVc, and HCVd, which differ only in their distance from the supernova explosion.

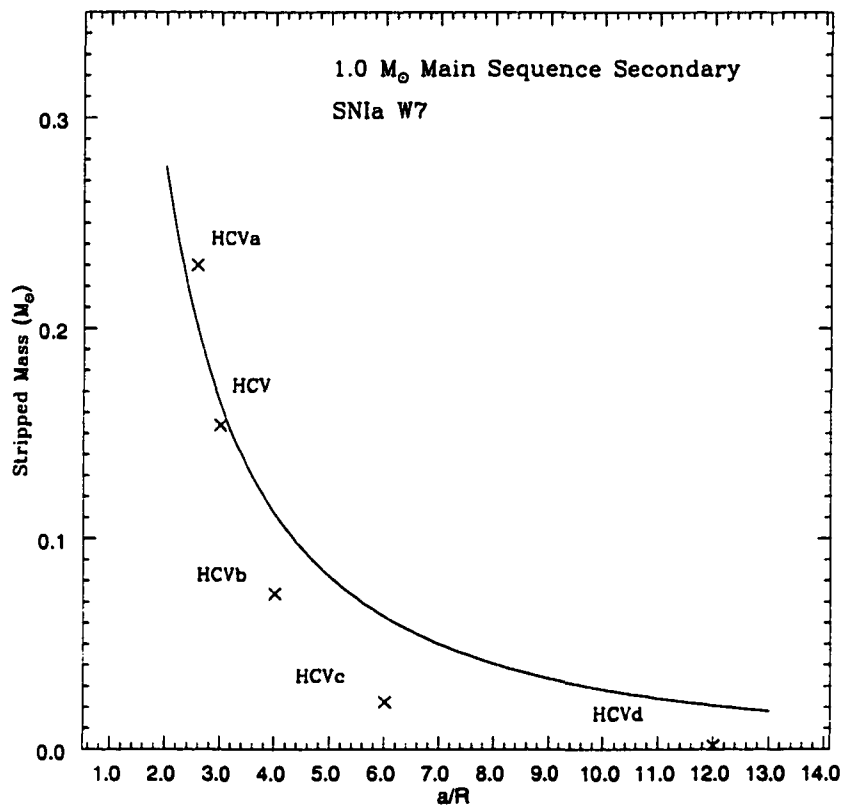

Figure 4.18 Analytic estimates of the mass stripping for the main sequence secondary as a function of a/R, the ratio of the binary to the stellar radius. The crosses indicate the numerical mass stripping of the of the main sequence secondary for the HCV and test cases HCVa, HCVb, HCVc, and HCVd, which differ only in their distance from the supernova explosion.

CHAPTER 5

SYSTEMATIC TRENDS WITH BINARY SEPARATION

To study the effect of changing the binary separation, we performed four test cases with the 1.0 $M_{\odot}$ main sequence secondary in addition to the HCV simulation: HCVa, HCVb, HCVc, and HCVd. The ratio of binary separation to stellar radius (a/R) is 2.57, 4.0, 6.0, and 12.0, respectively, with HCV having a ratio of 3.0, making it the second-closest secondary (see Table 3.4). Because the incident momentum scales as the inverse square of the separation, we expect a significant change in the amount of stripped mass and in the kick. From Tables 4.2 and 4.3 we see that over this range of orbital separation the stripped mass varies more than a factor of 100, from 0.23 $M_{\odot}$ to 0.0018 $M_{\odot}$, and the kick varies by a factor of 9, from 137 km s^{-1} to 15 km s^{-1}.

Figures 4.17 and A.4 visually demonstrate the change in the strength of the impact. Figure 4.17 shows the velocity of the stellar remnant with time for all five simulations. In the strongest impact, the companion experiences the strongest initial acceleration, followed by the strongest deceleration as the pressure rises in the back of the star. In the weakest impact, the companion experiences a very weak acceleration, which is not followed by a deceleration phase. In this case, the shock propagating through the companion is too weak to cause a pressure

rise in the back of the star. Figures A.4 illustrate the decrease in strength of the impacts with a series of 2-D images shown at $1000 - 1300$ seconds after the supernova explosion. In the HCV simulation (Figure A.4a), the shock has already passed through the companion. The bow shock is broad, within which we see well-developed Kelvin-Helmholtz and Rayleigh-Taylor instabilities trailing behind the companion that indicate mass loss is occurring. In the HCVb simulation (Figure A.4b), the interaction is at a comparable phase, except that the shock has just converged behind the star and the trailing instabilities are less developed. In the HCVc simulation (Figure A.4c), the shock is still passing through the star and the bow shock is noticeably much narrower than in the stronger impacts. In comparison with the other cases, the impact is almost mild in the HCVd simulation (Figure A.4d). Here, the bow shock is very narrow and the shock's propagation through the star is slow.

We use the separation study to compare our numerical stripped mass and kick with the analytic formulae of Wheeler et al. (1975). Figure 4.18 shows the numerical and analytic stripped mass as a function of (a/R). As expected, the stripped mass and kick are sensitive functions of (a/R). As shown in the figure, the analytic stripped mass usually overestimates the amount of mass loss by $5 - 50\%$ for separations in the range of $a/R = 3.0 - 4.0$. For greater separations, the mass loss is severely overestimated. For smaller separations, the mass loss is underestimated. Figure 5.1 shows a similar plot for the kick. Our analytic estimate of the kick is calculated from simple conservation of momentum and does not include a logarithmic factor to represent an additional kick from ablation because, as was shown by Fryxell & Arnett (1981), this would systematically overestimate the kick. The analytic method consistently overestimates the kick from the impact, by $18\% - 47\%$ in the range of our test cases. To conclude, we can say that the

analytic estimates of the stripped mass provide a good estimate (within 10%) for binaries near Roche lobe overflow ($a/R \approx 3$), but for closer and farther separations the estimates are substantially in error. Furthermore, the analytic estimates of the kicks provide a ballpark value for all separations, but are systematically high. The kicks are below the orbital velocity of the secondary for all orbital separations.

We can use the separation study to see how the average drag coefficient is likely to depend on the strength of the impact. The efficiency of the transfer of momentum is given by the ratio of stellar remnant momentum to the incident supernova momentum and can be equated to an average drag coefficient (Table 4.3). Typical coefficients lie in the range of $0.2 - 0.5$, rising systematically as the binary separation increases. We note that, as the binary separation increases, less mass is stripped from the companion and its geometrical area does not decrease as much. More of the incident supernova momentum can be intercepted by the remnant. In essence, the average drag rises for impacts in which less material is stripped.

We can use a similar argument to explain why the two subgiant scenarios, HCVL and HCVLa, have different drag coefficients. In the HCVLa simulation, the 2.1 $M_\odot$ subgiant companion loses 12% of its mass. In comparison, in the HCVL simulation the 1.1 $M_\odot$ subgiant loses 15% of its mass. In addition to losing a greater fraction of its mass, the 1.1 $M_\odot$ subgiant is more centrally concentrated, so a larger radial fraction of the star must have been ejected. With the decrease in geometrical area from the mass loss, the remnant of the 1.1 $M_\odot$ subgiant receives a smaller fraction of the incident momentum. In fact, because the 1.1 $M_\odot$ subgiant is so much more centrally concentrated than the 1.0 $M_\odot$ main sequence star, its coefficient is lower. Since the remnant masses are now comparable, the subgiant

remnant receives a smaller kick.

Despite the dramatic change in stripped mass and kick, the characteristic velocity of the stripped material stays between 870 km s^{-1} and 690 km s^{-1}, with the stripped material from the closest binaries having the highest characteristic velocities. Figures 4.12 show the original velocity distribution for all five main sequence simulations with the half-mass velocities listed. When a typical escape velocity is subtracted in quadrature, the characteristic velocities shift downwards only slightly from 850 km s^{-1} to 660 km s^{-1}. The fluctuations in the high-velocity end of the velocity distributions seem to reflect the density variations in the initial supernova ejecta model, and like the characteristic velocity, decrease in strength and velocity as the binary separation increases.

We can understand the characteristic velocity by noting that the companion's shocked material has a specific internal energy equal to its specific kinetic energy, which is determined by the speed of the shock. When the shock is strong, the envelope is heated enough that its new speed of sound exceeds the companion's escape velocity and the envelope is free to evaporate away from the star. As the shock decelerates, as it will when it climbs the steep density gradient of the star, less specific internal energy is deposited in the envelope and the new speed of sound will be lower. Eventually, the speed of sound will be lower than the escape velocity and the heated material will remain bound to the star. The material that escapes first will be the material shock-heated in the outer layers where most of the energy is deposited; this material will have the highest characteristic velocities. In time, the underlying layers of the envelope will evaporate off, leaving the marginally bound material clinging to the stellar surface. The amount of mass heated to sufficiently high temperatures is less for greater separations.

The closest companions will create the widest plume of stripped material. For an explosion in a close binary with a hydrogen-rich companion, the contaminating hydrogen can fill a solid angle of 2π steradians. A companion in a more distant binary will leave a narrower trail of contaminating hydrogen. This can been seen in Figures 5.2 and 5.3. Figure 5.2 shows the solid angle distribution $dM/d\Omega$ of the stripped material as a function of α, the angle from the downstream axis, and provides the half-mass angles for each distribution. These range from 10° to 45°. Figure 5.3 shows the same information plotted as a polar plot, with the radius being the magnitude of $dM/d\alpha$ and α once again being the angle from the downstream axis. Clearly, the closer the secondary is to the explosion, the wider in solid angle is the stripped material. As shown in Figure 5.3, most of the contaminating hydrogen is exterior to the geometrical shadow. The outer extent of the contamination is related to the amount of mass loss, which as can be seen in Figures A.4, is greatest for the strongest impacts.

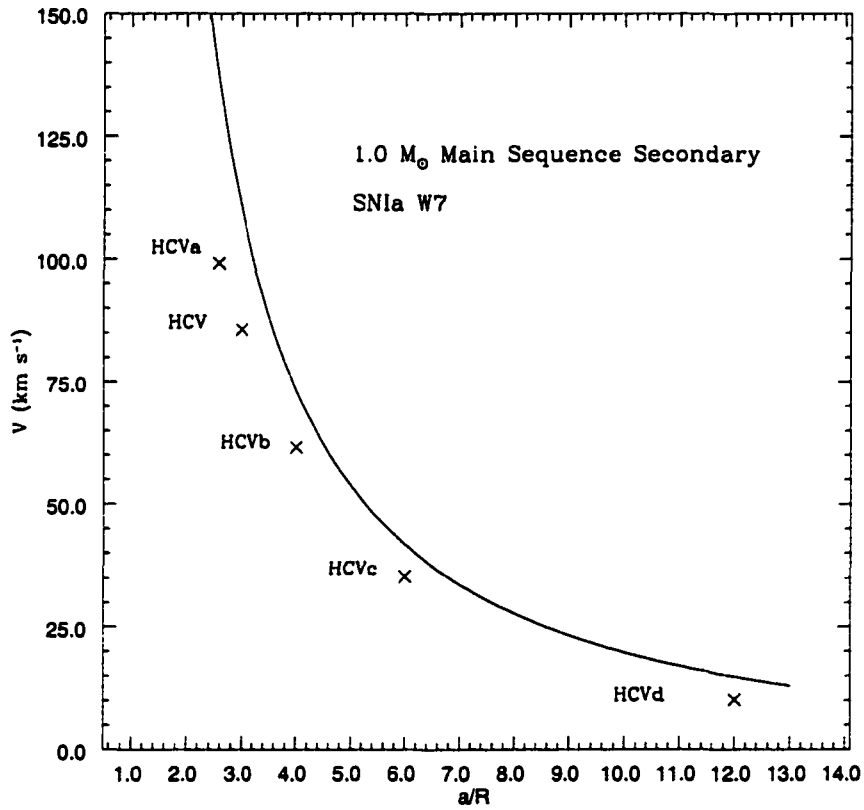

Figure 5.1 Analytic estimates of the impulses received by the impact for the main sequence secondary as a function of a/R, the ratio of the orbital separation to the stellar radius. The crosses indicate the numerical impulses of the main sequence secondary for the HCV and test cases HCVa, HCVb, HCVc, and HCVd, which differ only in their distance from the supernova explosion.

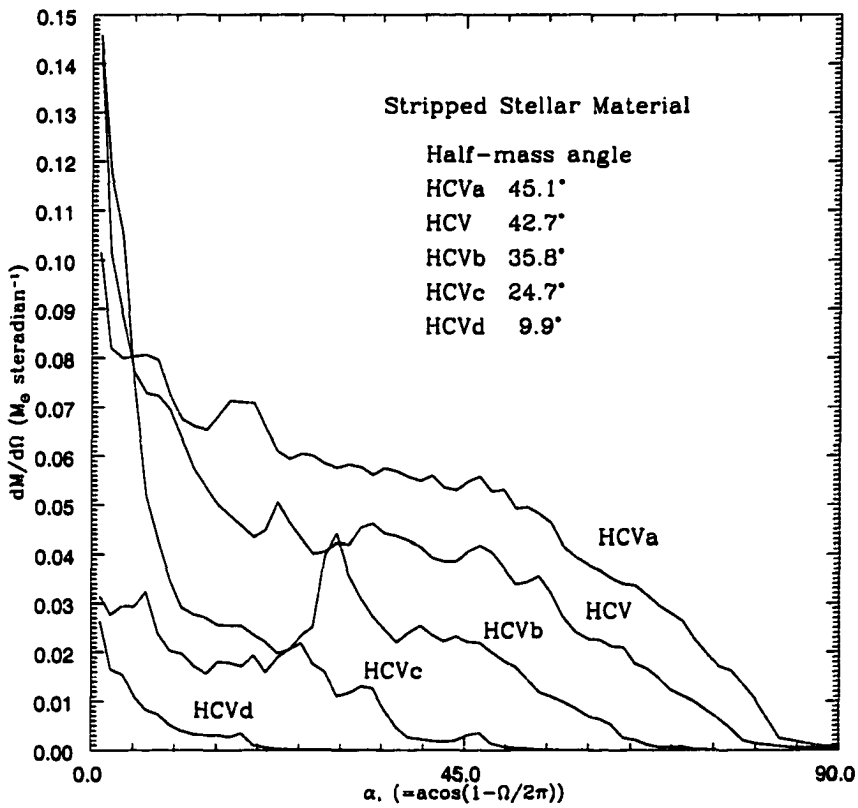

Figure 5.2 Solid angle distribution of the stripped material of the main sequence secondary for the HCV and test cases HCVa, HCVb, HCVc, and HCVd. The half-mass angle of each distribution is listed.

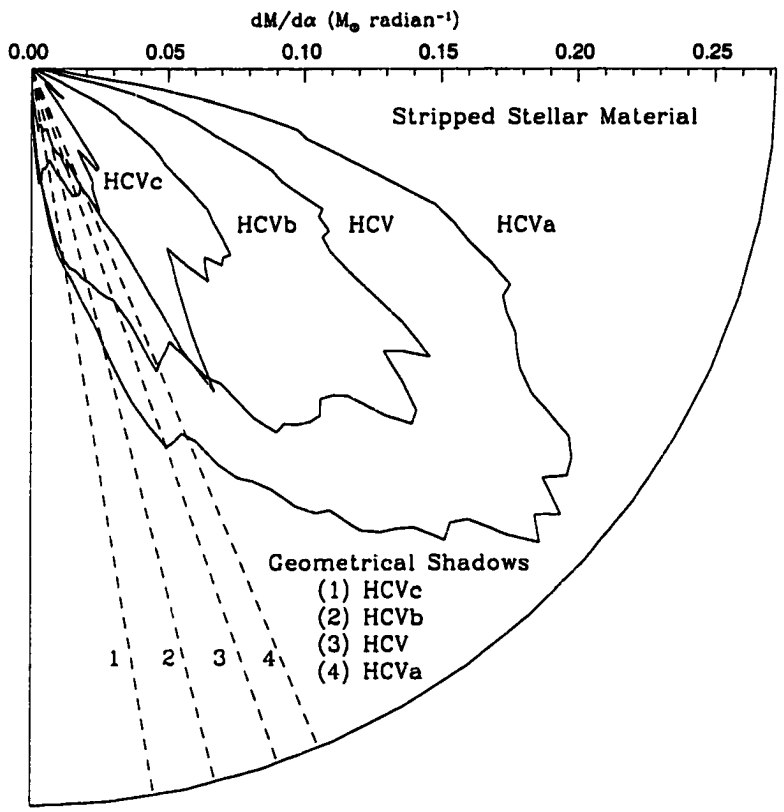

Figure 5.3 The magnitude of the angular distribution (dM/dα) is plotted as the radial coordinate for the main sequence simulation HCV and test cases HCVa, HCVb, and HCVc, which differ only in their distance from the supernova explosion.

CHAPTER 6

THE SUBGIANT COMPANION

Next, we describe the impact of the blast wave on a subgiant star, our HCVL scenario. As in the main sequence case, we neglect any changes to the structure of the star from the Roche potential or an optically thick wind from the white dwarf which would complicate the simulation. For this simulation we use a $330(\rho) \times 565(z)$ cylindrical grid with the 1.13 $M_{\odot}$ subgiant secondary centered on the origin. Approximately $200(\rho) \times 100(z)$ zones are allocated to the secondary. We use the same dimensions relative to the companion's radius as the main sequence simulation: 6 stellar radii in the ρ direction, 12 stellar radii in the downstream (negative z) direction and 2 stellar radii in the upstream (positive z) direction. The same supernova ejecta model (W7) is used and the debris flows onto the grid in the same way. We show time frames of this simulation up to 2.0×10^4 seconds, which is longer than the companion's dynamical time of 3.5×10^3 seconds and longer than the 2.5×10^3 seconds that it takes for the trailing edge of the supernova to sweep past the back of the companion.

For clarity, this section is subdivided into distinct topics. In §6.1 we describe the hydrodynamic stages of the impact and in §6.2 we describe the stripped mass for this scenario. In §6.3, we discuss the velocity and solid angle distributions of

the stripped companion material and the observational implications. Finally, in §6.4, we discuss the kick received by the remnant of the companion. To avoid repetition, we focus only on the important differences between the main sequence and subgiant simulations.

6.1. Hydrodynamics of the Impact on the Subgiant Companion

The impact of the supernova W7 on the subgiant follows the same sequence of events as the impact on the main sequence star. The subgiant subtends almost the same solid angle as the main sequence star (see Table 3.4), so the incident momentum is almost the same in both simulations. Given this, it is not surprising that the character of the impact has not changed. However, because of the increase in physical scale, which goes as the radius of the companion star, the sequence of events occurs at slightly different times. Also, the compact core of the subgiant alters the progress of the shock through the star, and the larger envelope increases the timescale required to bring the remnant back into hydrostatic equilibrium. The highlights of the impact on the subgiant are shown in several 2-D images in Figures A.5 and A.6.

Figure A.5a shows the impact of the supernova ejecta on the subgiant 343 seconds after the explosion. The leading shock front preceding the ejecta has converged along the downstream axis. The density jumps in the ejecta that are visible as spherical rings have already distorted the bow shock. More than 90% of the supernova's mass and momentum that will collide with the subgiant is now represented on the grid. At this early stage, only 0.06 $M_{\odot}$ of the secondary's envelope has been stripped and the stripped material is still in close proximity to the secondary.

Figure A.5b illustrates the curvature of the shock front at 945 seconds. As with the main sequence companion, the shock front driven through the center of the subgiant decelerates as it nears the subgiant's tightly-bound core. The shock front driven into the outer envelope propagates so much faster that it converges on the downstream axis just after the stellar core is shocked. As with the main sequence companion, a reflection shock passes back through the subgiant.

By Figure A.5c, 2044 seconds after the explosion, the supernova shell has swept by the secondary. Shock-heated material can be seen streaming from the subgiant within the cavity shaped by the bow shock. By this time, 0.15 $M_{\odot}$ of stellar material has been stripped. The Rayleigh-Taylor and Kelvin-Helmholtz instabilities can be seen easily in Figure A.6.

At 2×10^4 seconds (Figure A.5d), the companion is beginning to recover hydrostatic equilibrium. Like the main sequence companion, the star is surrounded by an extended envelope of low-density material. A complicated series of shocks formed during the stellar pulsation phase are propagating slowly through the outer envelope. By this time, 0.17 $M_{\odot}$ has been stripped and the subgiant has received a kick of 49 km s^{-1} from the impact.

The pressure and density of the subgiant fluctuate in the same way as in the main sequence case. The central pressure first rises rapidly as the shock passes through the stellar core at $600 - 700$ seconds, then slowly falls as the star expands. As in the main sequence impact, the material which is now only marginally bound begins to collapse back onto the subgiant and at $\sim$ 4000 seconds a shock is transmitted into the outer envelope. A pulsation phase follows.

The density and entropy profiles for the pre- and post-impact subgiant are shown in Figures 4.6 and 4.7. The radius of the remnant star, which we define as

the radius that encloses about 90% of the remnant's mass, is $\sim 0.9\ R_\odot$, which is a decrease of 48%. The remaining 10% of the mass forms a low-density extended envelope out to 5.9×10^6 km ($\sim 8\ R_\odot$).

6.2. The Stripped Mass of the Subgiant Companion

We determine the amount of mass stripped in the same way we did for the main sequence case and list it in Table 4.2. We include the mass stripped for two subgiant scenarios: HCVL and HCVLa. The HCVL binary scenario uses a 1.13 $M_\odot$ subgiant which was created from a 2.1 $M_\odot$ subgiant that was artificially stripped of its outer envelope to coarsely mimic mass transfer prior to the supernova explosion. The HCVLa binary scenario uses the original 2.1 $M_\odot$ subgiant with a slightly larger binary separation so that the same solid angle is subtended in order to ensure that both secondaries receive the same incident momentum from the blast. This scenario was included only as a test case. At the end of the HCVL simulation, 3×10^4 seconds after the supernova explosion ($\sim$ 5 sound crossing times), 0.17 $M_\odot$ of stellar material has become unbound, and of this material, about 97% has left the grid by the last timestep. The mass-stripping phase lasts roughly 3.7×10^3 seconds, long enough for 96% for the mass that will be stripped by the end of the simulation to be stripped, and much longer than the 2.5×10^3 seconds required for passage of the supernova blast around the secondary. In comparison, the original 2.1 $M_\odot$ subgiant in the HCVLa simulation loses 0.25 $M_\odot$.

Table 4.2 compares the numerical stripped mass with an analytic estimate. The analytic calculation, which underestimates the stripped mass for both the HCVL and HCVLa simulations, is nonetheless within 22% of the numerical result. We ran the HCVLa simulation as a test case to see if the stripped mass scales

directly with the companion's mass for the same subtended solid angle. We find that the mass loss almost scales directly with the mass of the companion. That is, the 2.1 $M_\odot$ subgiant loses 0.25 $M_\odot$, which is 12% of its mass. In comparison, the 1.13 $M_\odot$ subgiant loses 0.17 $M_\odot$, which is 15% of its mass.

6.3. Distribution in Velocity and Angle of the Material Stripped from the Subgiant Companion

Our key result for the subgiant simulation is the velocity distribution of the stripped hydrogen, shown in Figure 6.1 with the SN W7 velocity distribution. The velocity profile of the material stripped from the subgiant shows many of the same features seen in the main sequence star simulation. The half-mass point for the subgiant is just slightly faster: 900 km s^{-1} compared with 848 km s^{-1} for the main sequence case. Both characteristic velocities are much less than the half-mass velocity of the supernova ejecta of 7836 km s^{-1}. Figure 6.1 marks the characteristic velocities with a vertical line and an arrow. As in the main sequence case, the bulk of the stripped material, predominately hydrogen and helium, is embedded within the iron layer of the supernova ejecta. Once again, a high-velocity tail exists which implies that a trace of companion hydrogen is swept up into the oxygen and silicon layers of the supernova ejecta.

The differences between the main sequence and subgiant can be seen in Figure 4.11, which shows the asymptotic velocity profile. As discussed in §4.5, we subtract in quadrature an estimate for the local escape velocity that was used to distinguish between the stripped and the unstripped material. This approximates the velocity profile at infinity, when the stripped material is free of the secondary's gravitational potential. The velocity profile of the mass stripped from the subgiant

companion shows a subtle shift to higher velocities, and the high-velocity tail shows a single peak near 3×10^3 km s^{-1}. The velocity profile of mass stripped from the main sequence companion shows three peaks, which we identify with the three composition transitions in the W7 model; the other two peaks in the mass stripped from the subgiant are not clearly distinguishable.

Just as the velocity profile of the subgiant's stripped material is very similar to the velocity profile of the main sequence star's stripped material, the spatial distribution of the subgiant's stripped material shows a strong similarity to that in the main sequence case. Figure 4.13 illustrates the distribution in solid angle ($dM/d\Omega$) of the stripped material in the HCVL and HCV simulations, expressed in terms of the angle, α, from the downstream axis. The half-mass point of the HCVL distribution is $\sim 49°$, just slightly more extended in angle than in the main sequence case, which has a half-mass angle of 43°. In Figure 4.14, the polar angle, α, once again represents the angle from the downstream axis and the radial coordinate represents the magnitude of $dM/d\alpha$. The material stripped from the subgiant and the main sequence companions fills almost the same cone, with the subgiant filling in a slightly broader one. Once again, the majority of the stripped mass is exterior to the geometrical shadow, the shadow that the secondary would cast from the site of the explosion of the primary. The collision of the supernova debris with the subgiant secondary will create a hole in the debris structure of $\sim 32°$ in the high-velocity ejecta and of $\sim 40°$ in the low-velocity ejecta. The asymmetry of the supernova ejecta will be slightly larger at the highest velocities for the subgiant model than the main sequence model. The asymmetry at low velocities will be almost the same for both models. As in the main sequence model, the asymmetry of the supernova ejecta is a direct indication of the presence of a companion star.

The hydrogen mass fraction is shown as a function of supernova mass and velocity in Figures 6.2 and 6.3. The hydrogen mass fraction falls abruptly as the velocity increases. At 10^4 km s^{-1}, which is near the oxygen and silicon layers, X(H)$\sim 3 \times 10^{-3}$. Of course, we know from the numerical simulation that the ejected material contaminates a wide solid angle behind the secondary. For the HCVL simulation, 90% of the stripped hydrogen lies within 72.5° of the downstream axis, which corresponds to a fractional solid angle of 35%. Figures 6.2 and 6.3 show the expected mass fraction within the contaminated solid angle. As expected, the mass fraction rises dramatically. Of course, if the subgiant were of higher mass, then the hydrogen mass fraction in the supernova ejecta will rise accordingly. A higher mass secondary may be physically reasonable because our subgiant was initially 2.1 $M_\odot$ before its envelope was modified to mimic mass transfer prior to explosion.

6.4. The Kick Received by the Subgiant Companion

The net kicks for the HCVL and HCVLa subgiant scenarios are listed in Table 4.3 along with the kicks for the main sequence companions. For the HCVL simulation, we see the same qualitative behavior as in the main sequence simulations. The secondary receives a strong kick in the first 700 seconds after the explosion. A brief period of deceleration occurs until $\sim$ 1700 seconds, and the secondary is left with a terminal velocity of 49 km s^{-1} by 4000 seconds. The numerical velocity is only 70% of the analytic value of 70 km s^{-1}.

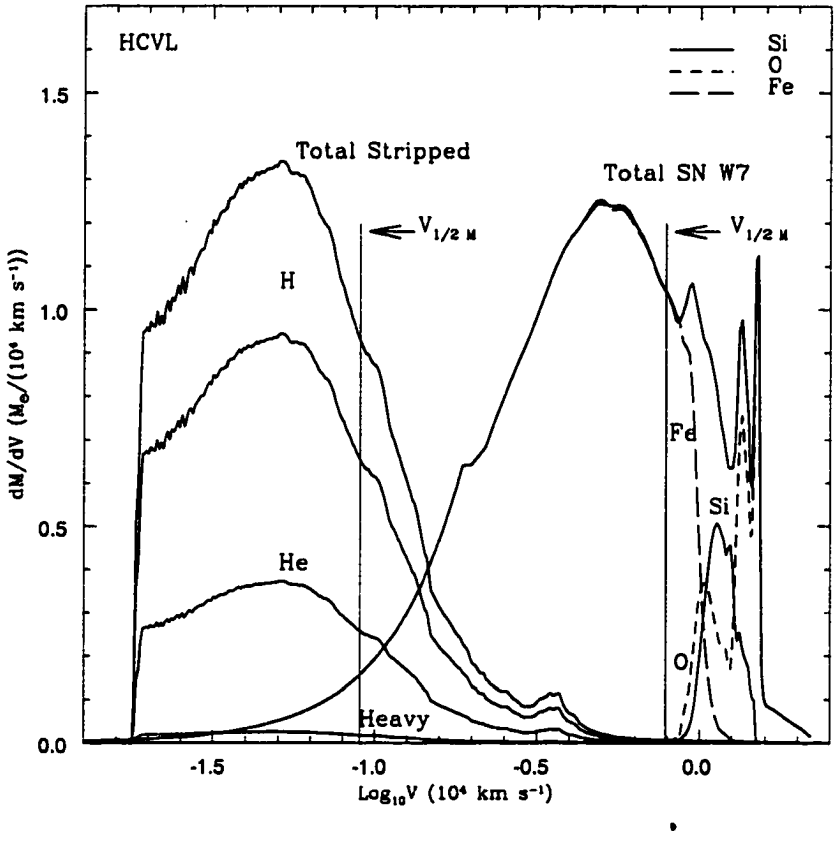

Figure 6.1 Velocity distribution dM/dV of the stripped stellar hydrogen and helium for the HCVL binary scenario at the end of the simulation, along with the velocity distribution of SNIa W7. The velocity at the half-mass point of the HCVL distribution, as indicated by the vertical line and the arrow, is 900 km s^{-1}. In contrast, the velocity at the half-mass point of the SN W7 distribution, also indicated in the plot, is 7836 km s^{-1}.

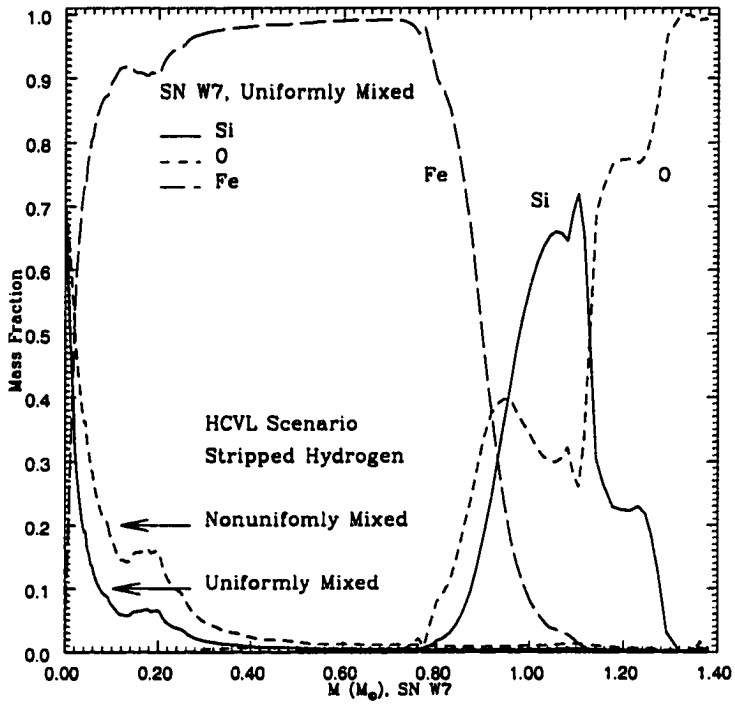

Figure 6.2 Hydrogen mass fraction of the contaminated supernova ejecta for the HCVL scenario (1.1 $M_{\odot}$ subgiant secondary) vs. the mass of the original W7 supernova model. The solid line indicates the hydrogen mass fraction assuming that the stripped material is uniformly mixed in angle with W7. The mass fractions of the O, Si, and Fe-group elements are shown for comparison. Because the stripped material in this simulation contaminates the supernova ejecta within only 72.5° of the downstream axis, the dashed line indicates the hydrogen mass fraction assuming mixing only in this region.

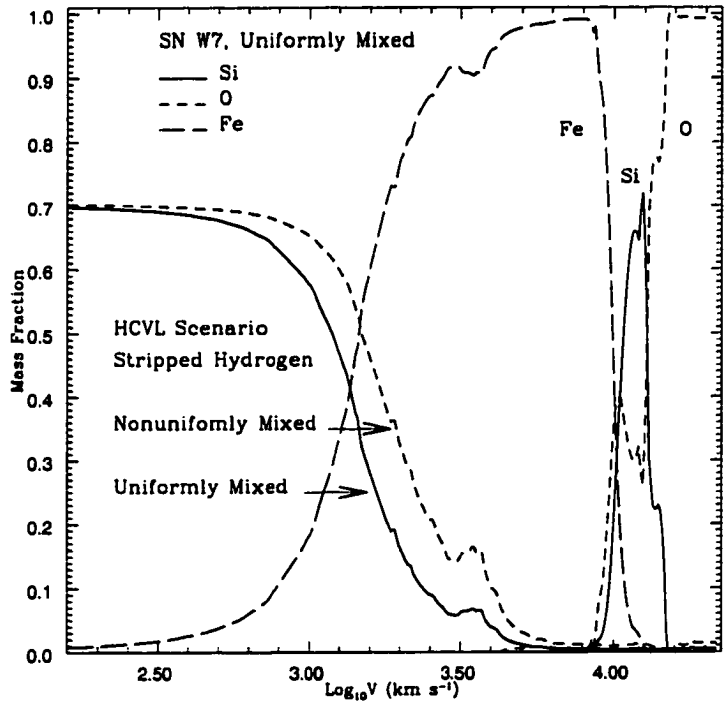

Figure 6.3 Hydrogen mass fraction of the contaminated supernova ejecta for the HCVL scenario (1.1 $M_{\odot}$ subgiant secondary) vs. velocity. See the caption for Figure 6.2.

CHAPTER 7

THE RED GIANT COMPANION

In this section, we describe the impact of a blast wave with a red giant star, our HALGOLa and SYMB scenarios. These scenarios differ in the explosion model and binary separation (see Table 3.4). The SYMB scenario has a slightly larger binary separation because the mass transfer is by wind accretion, and its white dwarf primary explodes as a sub-Chandrasekhar Type Ia. The HALGOLa scenario has a binary separation consistent with Roche lobe overflow, and its white dwarf explodes as a Chandrasekhar Type Ia. We use the same 0.98 $M_{\odot}$ red giant model for both simulations. As in the main sequence and subgiant cases, we neglect any complicating changes to the structure of the envelope from the Roche potential.

We change to spherical coordinates for all the red giant simulations. The grid extends 12 stellar radii and π radians. We use $585(r) \times 300(\theta)$ zones for the HALGOLa simulations and $653(r) \times 300(\theta)$ zones for the SYMB simulation, with $242(r) \times 300(\theta)$ and $247(r) \times 300(\theta)$ zones reserved for the red giant's envelope. The slight difference in the number of zones results from changing the grid to accommodate the different density and velocity profiles of the SN W7 (Nomoto et al. 1984) and SN Hedt (Woosley & Weaver 1994) ejecta models. We run the SYMB simulation for 8.0×10^6 seconds and the HALGOLa simulation for 6.0×10^6

seconds, which is only slightly more than one dynamical time, but still plenty of time for the stripped material to flow off the hydrodynamic grid. Because the loosely-bound envelope of the red giant is almost entirely stripped by the impact, there is no need to extend the calculation any further. We will concentrate on the SYMB simulation in this discussion, but will point out differences with the HALGOLa scenario when appropriate.

For clarity, this section is subdivided into distinct topics. Section 7.1 describes the character of the impact and §7.2 discusses the stripped mass for this scenario. In §7.3, the velocity and solid angle distributions of the stripped companion material and the observational implications are discussed. We focus only on the important differences with the main sequence and subgiant simulations discussed earlier.

7.1. Hydrodynamics of the Impact on the Red Giant Companion

Because of the lower binding energy of the envelope of the red giant (Figure 3.2), the impact of the supernova on the red giant companion is much more dramatic than the impact on the main sequence and subgiant companions. Unlike the main sequence and subgiant secondaries, the incident kinetic energy ($\sim 10^{49}$ ergs) is over 1000 times the envelope binding energy ($\sim 10^{46}$ ergs). The catastrophic effect of the blast on the weakly-bound envelope was pointed out by a number of authors (cf. Wheeler et al. 1975; Chugai 1986; Applegate & Terman 1989) and demonstrated numerically by Livne et al. (1992). Our simulations confirm the basic result of Livne et al. (1992): the envelope of the red giant is stripped and the velocity of the stripped material is less than 10^3 km s^{-1}. The half-mass point of our velocity distribution is 600 km s^{-1}. Like Livne et al. (1992), we select a binary

scenario with the red giant close enough to the white dwarf to be in Roche lobe overflow, our HALGOLa, and a scenario with a slightly larger binary separation, our SYMB. Unlike Livne et al. (1992), instead of a parameterized debris model, we use supernova Type Ia W7 for the blast for the HALGOLa and Type Ia sub-Chandrasekhar Hedt for the SYMB (Table 3.3). Figures A.7 and A.8 show highlights of the destruction of the red giant's envelope in a series of 2-D images from the SYMB simulation. However, Figures A.7 focus on the propagation of the shock through the envelope, while Figures A.8 show the entire grid.

To start the simulation, the red giant is centered at the origin, and the density and velocity profiles of the exploding white dwarf, scaled to 1.73 hours after the explosion, are positioned along the upstream axis. The impact begins at $\sim$ 3.0 hours after the explosion. Figures A.7a and A.8a show the interaction 5.67 hours later, at 8.68 hours after the explosion. The initial impact has driven a shock into the companion. The shock front in the "circumstellar" medium joins smoothly with the shock propagating through the red giant's envelope. The supernova material has not yet converged on the downstream axis.

By 14.23 hours, the bow shock has formed and the supernova ejecta have converged on the downstream axis right behind the star (Figures A.7b and A.8b). The shock passing through the companion is extremely curved. Kelvin-Helmholtz and Rayleigh-Taylor instabilities are clearly visible in the shock-heated material. The faint line of low-density material that is along the upstream axis and just outside the bow shock is a numerical artifact caused by the reflecting boundary.

After 2.10 days (Figures A.7c and A.8c), the shock moving through the envelope converges in the back of the star. The entire star has been shocked, and

almost the entire envelope has now been stripped down to the degenerate core. The slight distortion of the bow shock is due to the numerical artifact along the upstream axis. A reflection shock will soon be created that will pass back through the star.

By 5.86 days, pressure behind the bow shock has pushed it back towards the site of the explosion (Figure A.7d and A.8d). Although the velocity of the stripped material near the core is almost spherical, the bulk of the stripped material is moving downstream. In this simulation the bow shock is showing distortions as the density drops in the post-shock region. At this point, we regrid to increase the timestep and continue the simulation for an additional $\sim$ 86.7 days, or 92.6 days after the explosion, which is time enough for $\sim$ 85% of the stripped material to flow off the grid. Only a trace amount of material, at most 4% of the original envelope ($\sim$ 0.02 $M_{\odot}$), is left clinging to the degenerate core.

Unlike the main sequence and subgiant companions, which are done in cylindrical coordinates with the supernova debris added to the grid by the boundary conditions, the red giant simulations require the density and velocity profiles to be placed directly on the grid, off-center, as part of the initial conditions. The supersonic flow must propagate across radial lines and maintain its spherical structure. Figures A.8 show that the spherical structure of the debris is maintained. But does placing the spherical explosion off-center have any consequences for the amount of stripped mass or the velocity distribution? To test this and to address a concern that the numerical artifact along the axis might have unexpected consequences, we inverted the position of the supernova and the secondary for the HALGOLa simulation. Although there are small differences between the two simulations, in both cases over 0.54 $M_{\odot}$ of the red giant's envelope is ejected by the

blast. For the original HALGOLa simulation the half-mass point of the velocity distribution of the stripped material is 593 km s^{-1}, and for the inverted simulation the half-mass velocity is 584 km s^{-1}.

After the red giant's envelope is ejected, the degenerate core, now a single low-mass He pre-white dwarf, is left surrounded by a hot, entropized atmosphere. Although the blast strips most of the envelope, a small residual fraction (a few percent) may form an extended, hydrogen-rich envelope around the star. Although about $\sim 75\%$ of this envelope is within 4.4×10^7 km and has typical temperatures of $10^4 - 10^5$ K, the remaining $\sim 25\%$ is cooling adiabatically, and extends out as far as 2.4×10^8 km. Typical entropies in the envelope are $35 - 40$ in units of k_B^{-1} baryon^{-1}. In time, this extended envelope will settle onto the star, adding ~ 0.02 $M_\odot$ of hydrogen-rich material to the hydrogen burning layer. We speculate on the fate of the low-mass He pre-white dwarf in §9.

7.2. The Stripped Mass of the Red Giant Companion

We determine the mass lost in the same way we did for the main sequence and the subgiant cases. The stripped mass for the red giant simulations is shown in Table 4.2 with the results from the other simulations. Like Livne et al. (1992), we find that almost the entire envelope is removed by the impact, for all the red giant binary scenarios. For the HALGOLa simulation, the mass-stripping phase lasts roughly 10^5 seconds (or 1.2 days). After 6.0×10^6 seconds (or 69.5 days), 0.54 $M_\odot$ (98% of the stellar envelope) of stellar material has become unbound, and of this material, about 85% has left the grid. The stripped mass for the SYMB simulation is similar. The mass-stripping phase for the SYMB simulation lasts roughly 1.3×10^5 seconds (or 1.5 days). After 8.0×10^6 seconds (or 92.6 days), 0.53

$M_\odot$ (96% of the stellar envelope) of stellar material has become unbound, and of this material about 85% has left the grid.

7.3. Distribution in Velocity and Angle of the Material Stripped from the Red Giant Companion

Figures 7.1 and 7.2 show the velocity distribution of the stripped envelopes; both are shown with the original velocity distribution of the supernova ejecta, W7 for the HALGOLa simulation and Hedt for the SYMB simulation. The velocity distributions from the red giant simulations, which have the same basic shape as the distributions from the main sequence and subgiant simulations, have systematically shifted to lower velocities. The half-mass velocity of HALGOLa is 593 km s^{-1} compared with 421 km s^{-1} for the SYMB case.

To compare the red giant velocity distributions directly, we show in Figure 7.3 the asymptotic velocity distribution for both simulations. As discussed in §4.5, we subtract in quadrature an estimate of the local escape velocity to approximate the velocity distribution when the stripped material is free of the degenerate core, which now resembles a lone pre-white dwarf, surrounded by a residual layer of hydrogen and helium. Because the Hedt debris profile has only 78% of the momentum of the W7 profile, we expect the SYMB scenario to have a lower characteristic velocity. In fact, the SYMB stripped material has a half-mass velocity of 71% of the HALGOLa case. However, the SYMB scenario has a slightly greater separation. By repeating the SYMB simulation with the same binary separation as the HALGOLa simulation, we find that the solid angle distribution remains almost unchanged, but the new velocity profile is almost, but not quite, identical to the HALGOLa profile. As in the HALGOLa distribution, the new half-mass velocity is

593 km s^{-1}. The only distinct difference between the velocity profiles is the slight bump in the high-velocity tail (near $\sim 3.0 \times 10^3$ km s^{-1} in Figure 7.3), which is visible in the HALGOLa case and not visible in either the old or the new SYMB case. We conclude from this that the slight increase in the high-velocity tail reflects the different supernova ejecta models used and that the shift to lower velocities in the SYMB case reflects the slightly greater binary separation.

The solid angle distribution for both of the red giant scenarios is shown in Figure 7.4 and as a polar plot in Figure 7.5. In Figure 7.4, the U-shaped profile indicates the solid angle distribution if the red giant's envelope is ejected uniformly in all directions. Because the U-shaped profile reflects the change in the solid angle differential, $d\Omega$, we include this for reference. This shows that although the $dM/d\Omega$ profiles appear to be rising along the downstream axis, the amount of mass ejected in that direction is actually less than would be expected if the envelope had been uniformly stripped. In fact, the half-mass angles are 61° and 66°, with that for the SYMB scenario being slightly more extended. As in the main sequence and subgiant cases, the majority of the stripped mass is exterior to the solid angle enclosed by the geometrical shadow of the secondary as seen from the site of the explosion. In addition, there is now a substantial amount of mass that has been ejected past the 90° point.

The impact of the supernova ejecta onto the secondary creates a hole in the supernova debris (Figure 7.6). For the HALGOLa model, the supernova debris has a hole of $\sim 34°$ in the outer ejecta, which widens to $\sim 40°$ in the inner ejecta. This corresponds to $9\% - 12\%$ of the surface of the ejecta. The SYMB model has a slightly smaller hole of $\sim 32°$ in the outer ejecta, which widens to $\sim 37°$ in the inner ejecta. This corresponds to $8\% - 12\%$ of the surface of the ejecta.

The HALGOL model clearly creates more asymmetry in the supernova ejecta at the highest velocities than the SYMB model or the main sequence and subgiant models.

Figures 7.7 and 7.8 illustrate X(H), the hydrogen mass fraction in the contaminated supernova ejecta (assuming uniform angular mixing in the unperturbed supernova model) for the HALGOLa scenario. X(H) is generally higher in the red giant simulations than in the main sequence or subgiant simulations simply because of the larger mass ejected. However, because most of the hydrogen stripped from the red giant is at lower velocities, for the red giant case the hydrogen mass fraction at high velocities is slightly lower than in the main sequence and subgiant cases in that X(H) $\sim 2 \times 10^{-3}$ at velocities of 10^4 km s^{-1}, compared with X(H) $\sim 3 \times 10^{-3}$ for the main sequence and subgiant cases. If we constrain the mixing to just the contaminated solid angle behind the secondary, X(H) does rise, but not dramatically, because the contaminated solid angle is now so much larger that this correction becomes small. For the HALGOLa simulation, 90% of the stripped hydrogen lies within 115.4° of the downstream axis which corresponds to a fractional solid angle of 71%.

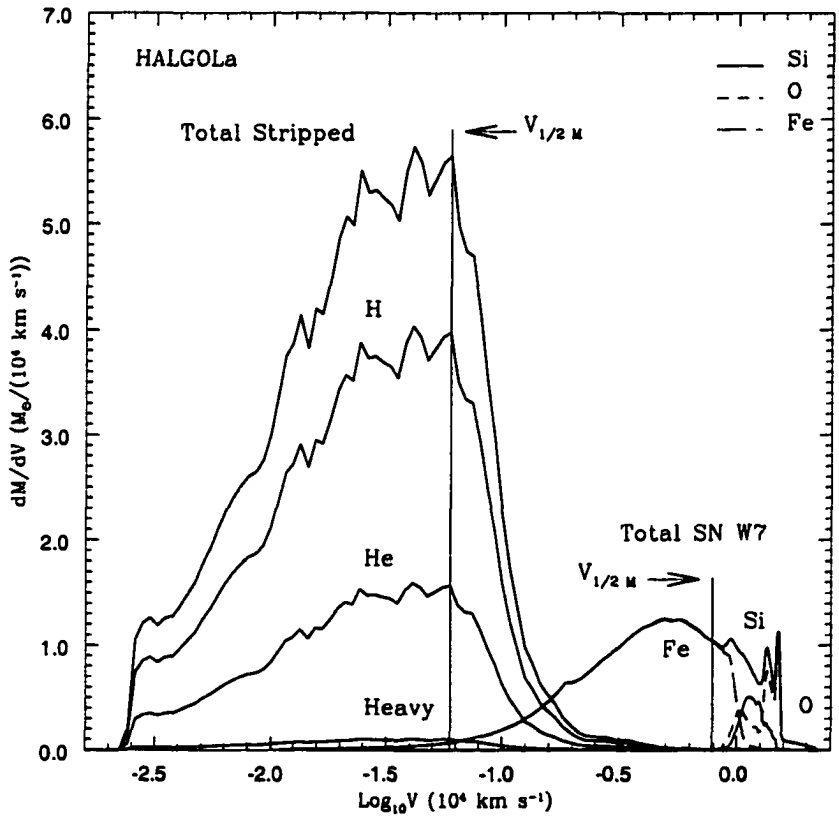

Figure 7.1 Velocity distribution dM/dV of the stripped stellar hydrogen and helium for the HALGOLa binary scenario at the end of the simulation, along with the velocity distribution of SNIa W7.

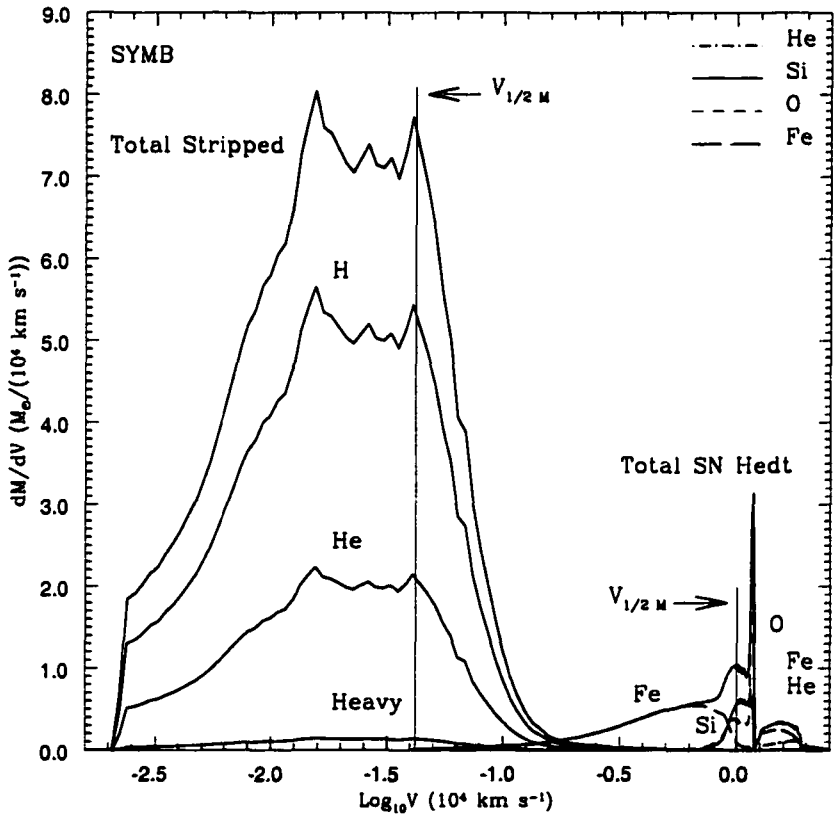

Figure 7.2 Velocity distribution dM/dV of the stripped stellar hydrogen and helium for the SYMB binary scenario at the end of the simulation, along with the velocity distribution of SNIa Hedt.

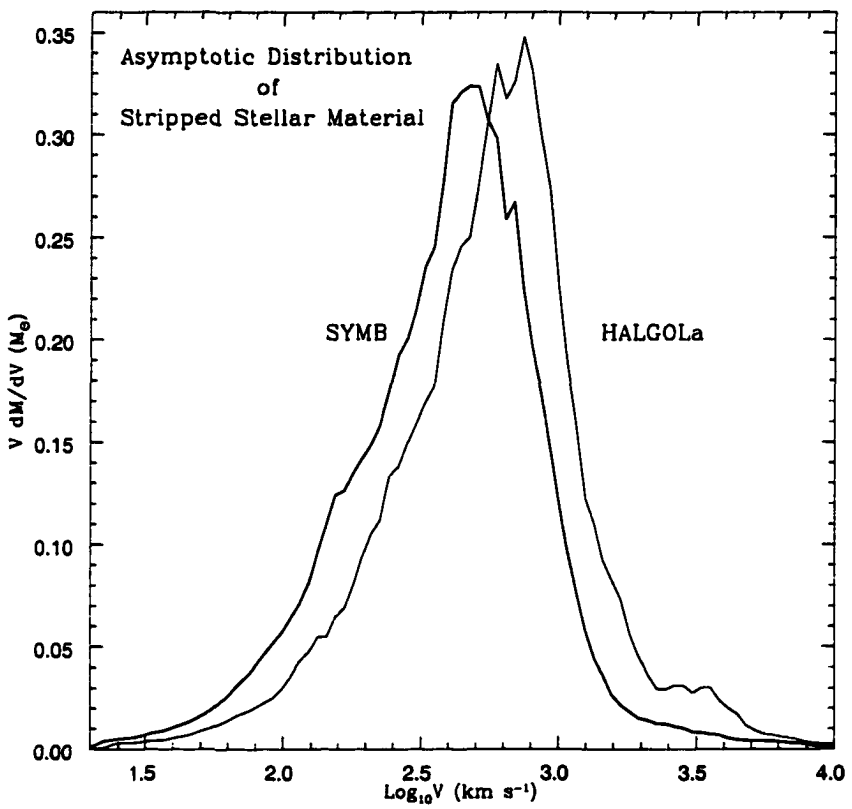

Figure 7.3 Estimate of the asymptotic velocity distribution dM/dV of the stripped stellar material of the red giant secondary from the SYMB and HALGOLa binary scenario, after the stripped material escapes the gravitational potential of the secondary star. We calculate the profiles by subtracting in quadrature an estimate of the escape velocity as the stripped material leaves the grid.

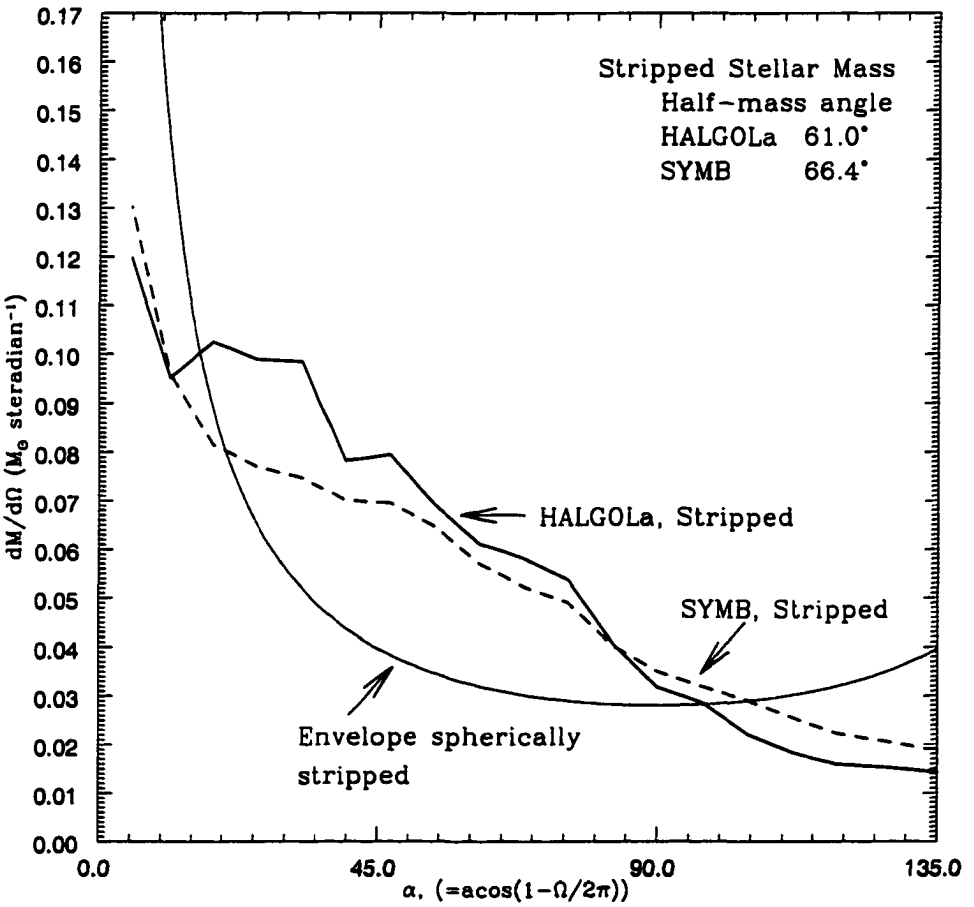

Figure 7.4 Solid angle distribution of the stripped envelope of the red giant simulations HALGOLa and SYMB. The vertical line indicates the half-mass angle of the distribution. For comparison, we also include the solid angle distribution that is expected if the red giant envelope is stripped spherically symmetrically.

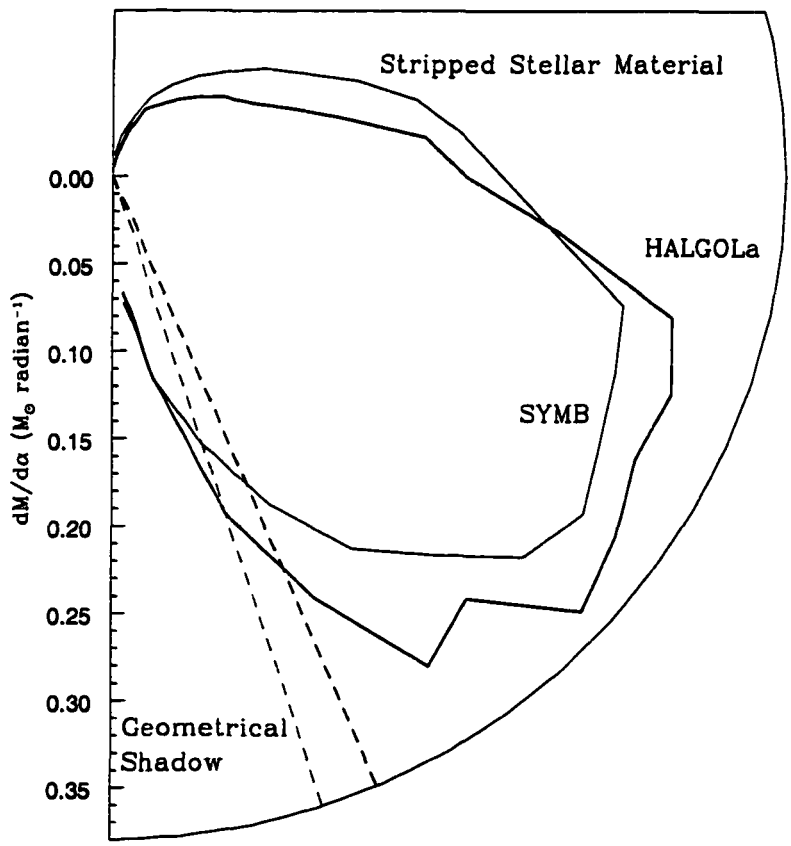

Figure 7.5 The magnitude of the angular distribution ($dM/d\alpha$) is plotted as the radial coordinate for the red giant simulations (HALGOLa and SYMB).

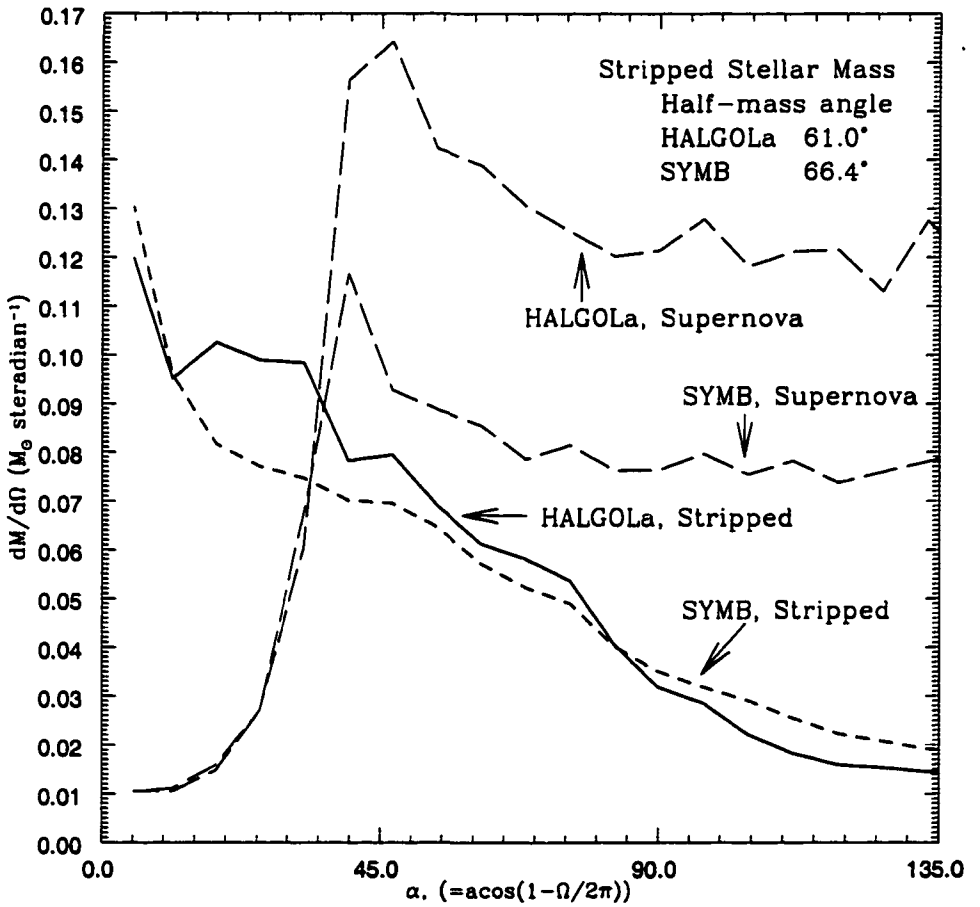

Figure 7.6 Solid angle distribution of the stripped envelope of the red giant simulations HALGOLa and SYMB. The vertical line indicates the half-mass angle of the distribution. The dashed lines indicate the distribution of supernova material. The gap between $0° - 40°$ illustrates the hole in the supernova ejecta created by the impact.

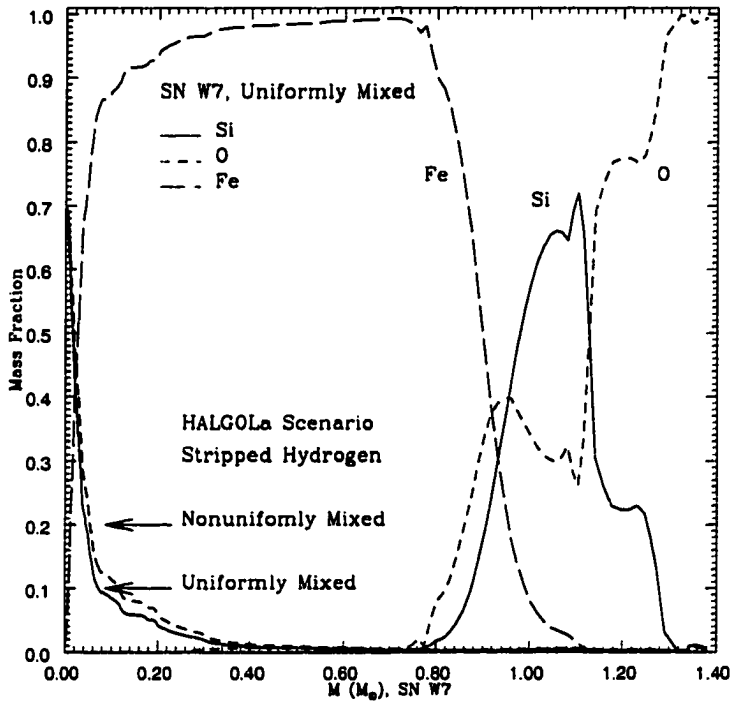

Figure 7.7 Hydrogen mass fraction of the contaminated supernova ejecta for the HALGOLa scenario (0.98 $M_{\odot}$ red giant secondary) vs. the mass of the original W7 supernova model. The solid line indicates the hydrogen mass fraction assuming that the stripped material is uniformly mixed in angle with Type Ia model W7. The mass fractions of the O, Si, and Fe-group elements are shown for comparison. Because the stripped material in this simulation contaminates the supernova ejecta within only 115.4° of the downstream axis, the dashed line indicates the hydrogen mass fraction assuming mixing only in this region.

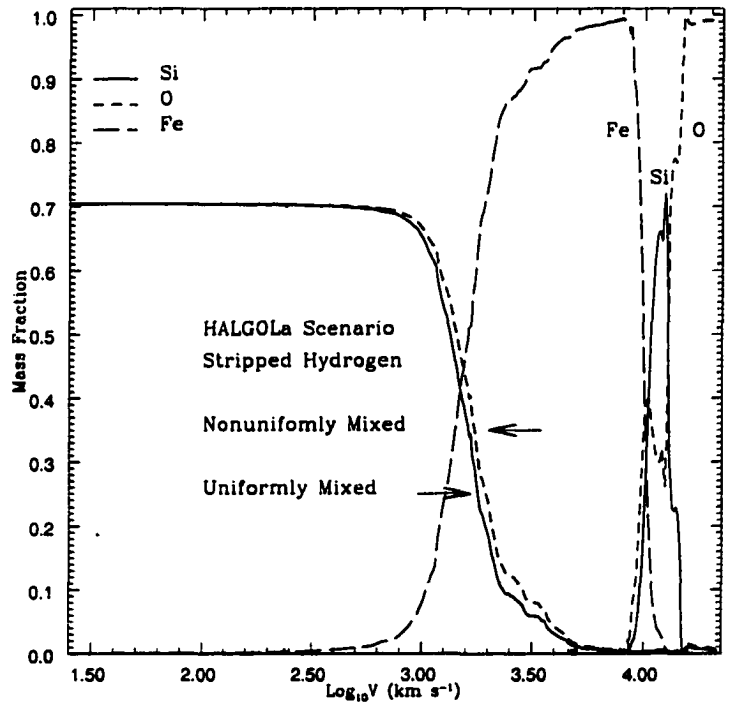

Figure 7.8 Hydrogen mass fraction of the contaminated supernova ejecta for the HALGOLa scenario (0.98 $M_{\odot}$ subgiant secondary) vs. velocity. See the caption for Figure 7.7.

CHAPTER 8

UPPER LIMIT ON HIGH-VELOCITY HYDROGEN

Ideally, we would like a firm upper limit on the amount of hydrogen that can be mixed with the supernova debris at high and low velocities without being detected in the spectrum. The low-velocity upper limit requires a non-LTE radiative transfer study (Pinto et al. 1999). For the high-velocity upper limit we can use upper limits from Type Ia observations near maximum light. Although most of the stripped material is ejected at low velocities, for all the binary scenarios we have considered, there is a small high-velocity tail, as shown in Figure 8.1. In Table 8.1, selected points are tabulated. We present the velocity distribution as the total amount of hydrogen exterior to each velocity.[1]

Above 3.0×10^3 km s^{-1}, the left-hand edge of Figure 8.1, all four scenarios have less than $\sim 0.014\ M_\odot$ of high-velocity hydrogen. The HCVL simulation has $0.014\ M_\odot$, followed by the HALGOLa with $0.012\ M_\odot$, the HCV with 0.010

[1]In §2, we discuss the effect of resolution on the high-velocity profile. In the HCV simulation there is 15% more mass above 3×10^3 km s^{-1} and 26% less mass above 1.5×10^4 km s^{-1} than in the high-resolution simulation. Hence, at the higher velocities we conclude that changes in mass greater than $\sim 30\%$ are meaningful.

$M_\odot$, and lastly, the SYMB simulation with only 0.004 $M_\odot$. By 10^4 km s^{-1}, the amount of high-velocity hydrogen for all four scenarios has dropped by almost a factor of 10. The HCVL, HCV, and the HALGOLa scenarios are very similar up to this velocity. Because of the greater binary separation and smaller impact momentum and energy, the SYMB scenario has less than half the hydrogen of the other scenarios. When the SYMB scenario has the same binary separation as the HALGOLa scenario, it too has a velocity distribution like the others in this range ($3 \times 10^3 - 10^4$ km s^{-1}). It would be difficult to discriminate between the main sequence, the subgiant, and the HALGOLa red giant scenarios in this velocity range. However, we can easily discriminate between the companions in Roche lobe overflow and a model in which the red giant that is too distant to be in Roche lobe overflow, our SYMB scenario.

For 1.5×10^4 km s^{-1}, the HALGOLa and the SYMB scenarios have the most high-velocity hydrogen, the HALGOLa with 3.3×10^{-4} $M_\odot$ and the SYMB with 3.0×10^{-4} $M_\odot$. In Figure 8.1, the hydrogen distribution for the SYMB and HALGOLa scenarios converge at higher velocities, implying that the HALGOLa and the SYMB scenarios have almost the same amount of hydrogen at the highest velocities. We attribute this convergence to the momentum profile of Hedt (sub-Chandrasekhar model), which has more overall momentum at velocities greater than 1.5×10^4 km s^{-1} than SN W7 (Chandrasekhar model) (Figure 4.1). We note that the amount of high-velocity hydrogen above 1.5×10^4 km s^{-1} could be a direct indicator of the momentum profile of the supernova ejecta at the highest velocities.

Above 1.5×10^4 km s^{-1}, the HCVL and HCV scenarios have much less high-velocity hydrogen than in the red giant scenarios. The HCVL scenario has

only $1.7 \times 10^{-4}\ M_{\odot}$, which is only 53% of the high-velocity hydrogen of HALGOLa. The HCV has even less, only $1.3 \times 10^{-4}\ M_{\odot}$. We note that even if the red giant companions have more low-velocity hydrogen, they have more hydrogen above 1.5×10^{4} km s^{-1} than the main sequence or subgiant models. Because the HCVL has more high-velocity hydrogen than the HCV scenario, in principle we can discriminate between the subgiant and main sequence companion at 1.5×10^{4} km s^{-1}.

The upper limit of H/Si $\leq 2.0 \times 10^{-6}$ (relative to solar) from SN 1990M, which, assuming perfect mixing of the silicon in an ejecta profile like W7, corresponds to a total hydrogen mass of $\sim 3 \times 10^{-4}\ M_{\odot}$ (Della Valle et al. 1996) and is indicated by a horizontal line in Figure 8.1. Because Della Valle et al. (1996) estimated the error in the upper limit to be a factor of $2-3$, we also include horizontal lines to indicate this range. The vertical line indicates the velocity in SNIa W7 that corresponds to the outer 0.04 $M_{\odot}$ of the ejecta, which they estimated to be the mass in the photosphere at the time of the observations. If $3 \times 10^{-4}\ M_{\odot}$ is a reasonable upper limit to the total amount of hydrogen, and if it is mixed only within the observable photosphere, then we can compare our mass profiles with this upper limit at the edge of the observable photosphere. We see from the figure that none of the binary scenarios we have considered exceeds this upper limit. However, if the upper limit were reduced by only a factor of 3, the red giant and subgiant models would clearly exceed this limit, while the main sequence model is marginal. Because the supernova photosphere is non-LTE and the upper limit of Della Valle et al. (1996) is based on an LTE atmosphere, the hydrogen abundance in the supernova could be much higher than their upper limit indicates.

Table 8.1. Mass of Stripped Hydrogen with Velocity $\geq$ V at four chosen points: $V_A = 3.0 \times 10^3$ km s^{-1}, $V_B = 1.0 \times 10^4$ km s^{-1}, $V_C = 1.2 \times 10^4$ km s^{-1}, and $V_D = 1.5 \times 10^4$ km s^{-1}.

Scenario	A	B	C	D
HCV	$9.7 \times 10^{-3}\ M_\odot$	$1.3 \times 10^{-3}\ M_\odot$	$6.9 \times 10^{-4}\ M_\odot$	$1.3 \times 10^{-4}\ M_\odot$
HCVL	$1.4 \times 10^{-2}\ M_\odot$	$1.4 \times 10^{-3}\ M_\odot$	$7.8 \times 10^{-4}\ M_\odot$	$1.7 \times 10^{-4}\ M_\odot$
HALGOLa	$1.2 \times 10^{-2}\ M_\odot$	$1.4 \times 10^{-3}\ M_\odot$	$8.9 \times 10^{-4}\ M_\odot$	$3.3 \times 10^{-4}\ M_\odot$
SYMB	$4.3 \times 10^{-3}\ M_\odot$	$6.2 \times 10^{-4}\ M_\odot$	$4.8 \times 10^{-4}\ M_\odot$	$3.0 \times 10^{-4}\ M_\odot$

Figure 8.1 Mass of stripped hydrogen with velocity $\geq$ V for the HCV (1.0 main sequence), HCVL (1.13 $M_{\odot}$ subgiant), SYMB and HALGOLa (1.0 $M_{\odot}$ red giant) simulations. To compare the mass profiles to Type Ia supernova observations near maximum light, we indicate with a horizontal line the Della Valle et al. (1996) upper limit of 3×10^{-4} $M_{\odot}$ of hydrogen in the spectrum of SN 1990M. This assumes perfect radial mixing of the silicon and hydrogen. Because Della Valle et al. (1996) estimated the error in the upper limit to be a factor of $2 - 3$, we also include horizontal lines to indicate this range. Della Valle et al. (1996) estimated that the size of the photosphere was 0.04 $M_{\odot}$ at the time of the observation. The velocity corresponding to this mass is estimated from SNIa W7 and shown in the figure as a vertical line.

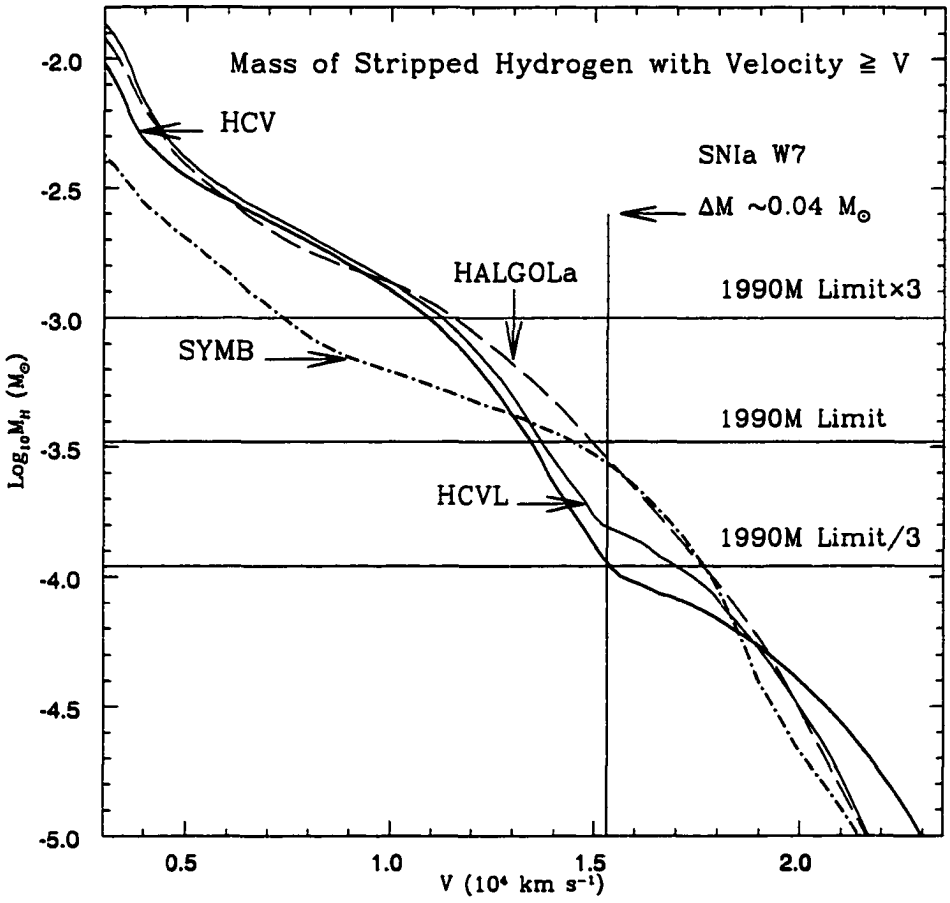
Mass of Stripped Hydrogen with Velocity ≧ V
HCV
SNIa W7
ΔM ~0.04 M⊙
HALGOLa
1990M Limit×3
SYMB
1990M Limit
HCVL
1990M Limit/3
-2.0
-2.5
-3.0
-3.5
-4.0
-4.5
-5.0
0.5
1.0
1.5
2.0
Log10MH (M⊙)
V (10⁴ km s⁻¹)

CHAPTER 9

THE FUTURE OF THE COMPANION STAR

The post-impact evolution of the main sequence and subgiant secondaries is a separate calculation requiring a 2-D stellar evolution code that is capable of handling initial models that are slightly asymmetric in density and temperature and completely out of thermal equilibrium. For example, although the main sequence star is recovering hydrostatic equilibrium by the end of the simulation, the density in the outer envelope of the star still varies by as much as a factor of 2 in different directions. The temperature and entropy profiles are also highly asymmetric, reflecting the shock history of the impact. Without attempting to follow the secondary's post-impact evolution in detail, we can only speculate about the secondary's future evolution.

Immediately after the impact, the main sequence star is puffed up, much like a pre-main sequence star. Although the nuclear energy generation in the core has been extinguished, the luminosity of the residue will be dramatically brighter for this extended envelope that is out of thermal equilbrium. Chaboyer (1998) estimated that with the asymmetrical temperature distribution the luminosity could vary from 500 $L_\odot$ to 5000 $L_\odot$ after the impact, with a Kelvin-Helmholtz timescale of 1400 years to 11000 years. After thermal equilibrium is reestablished, the

remnant will return to the main sequence along a Kelvin-Helmholtz track and then will continue its evolution at a rate prescribed by its new mass. Without mixing in the stellar core to refresh the hydrogen supply, the born-again star will appear near the middle of its main sequence lifetime. Using the main sequence relations R $\propto M^{2/3}$ and L $\propto M^5$, the 1.0 $M_\odot$ main sequence secondary will eventually return to the main sequence with a mass of 0.85 $M_\odot$(having lost 0.15 $M_\odot$ by the impact), with a slightly smaller radius of 0.9 $R_\odot$, and a luminosity near 0.4 $L_\odot$.

The subgiant puffs up after the impact and must contract to re-ignite hydrogen shell-burning, which will have been extinguished during the subgiant's expansion. As in the main sequence case, the luminosity will be extremely high during this phase. After thermal equilibrium is established and burning is reignited, the star will be back on a post-main sequence track with a slightly lower luminosity.

After the red giant's envelope is stripped by the impact of the supernova, the degenerate core, now a single low-mass He pre-white dwarf, is left surrounded by a hot, entropized hydrogen/helium atmosphere. The structure of the core is only minimally affected by the impact because the converging shock was weakened by the extremely strong pressure and density gradients in the interior of the red giant. Although the blast strips most of the envelope, a small residual fraction ($\sim$ 0.02 $M_\odot$) may form an extended, hydrogen-rich envelope. Although the impact may temporarily disrupt the hydrogen-burning layer, it is possible that the star may recommence shell burning as the envelope settles back down into a thin layer. As the degenerate core and hydrogen-rich envelope contracts, the star will evolve away from the red giant branch, along a track of constant luminosity ($\sim 10^3$ $L_\odot$) and rising effective temperature on a timescale of $10^5 - 10^6$ years for a 0.42 $M_\odot$ He core (Iben & Tutukov 1986; Iben & Livio 1993; Iben & Tutukov 1993). After the

effective temperature rises to greater than $\sim 3 \times 10^4$K, the star may appear as an underluminous main sequence O or B star. At the end of the contraction phase, the luminosity begins to drop. When the luminosity drops to $\sim 10\ L_{\odot}$, it will appear as a subluminous hot star; an sdO star if the temperature exceeds 3.5×10^4K or an sdB star if it does not (Iben & Livio 1993; Green 1999). The star will then continue to cool along a standard He white dwarf cooling track (Benvenuto 1999). This scenario could be a possible pathway for the formation of a subset of single, low-mass He white dwarfs.

CHAPTER 10

SUMMARY AND CONCLUSIONS

In this paper, we have presented numerous hydrodynamic simulations of the impact of a Type Ia supernova explosion with hydrogen-rich main sequence, subgiant, and red giant companions. The binary parameters were chosen to represent several classes of single-degenerate Type Ia progenitor models that have been suggested in the literature. All of the simulations involved low-mass ($1.0 - 2.0\ M_{\odot}$) companions that are close enough, or almost close enough, to be in Roche lobe overflow when the white dwarf primary explodes.

We described the supernova-secondary interaction for a main sequence, subgiant, and red giant companions with 2-D illustrations from the simulations. The collision follows the same basic pattern for the main sequence and subgiant because of their similar structure. The initial impact of the supernova shell with the surface of the main sequence star drives a shockwave into the stellar envelope. A reverse shock propagates back into the ejecta. A contact discontinuity marks the interface between the supernova ejecta and the shocked stellar material. The shock propagating through the stellar envelope decelerates as it runs up the steep stellar density gradient. The shock front, highly curved because of the density gradients, converges in the back of the star. A bow shock develops in front of

the companion star. After most of the supernova debris has passed by, the outer layers of the stellar envelope are ejected because they have been shock-heated to such an extent that the new speed of sound exceeds the companion's escape velocity. Kelvin-Helmholtz and Rayleigh-Taylor instabilities are very visible at this stage. The outer shocked material evaporates away from the star, embedded within the inner layer of the supernova ejecta. The stellar core expands and cools in response to the compression by the shock's passage through the core. The star has an extended, asymmetrical envelope and begins to pulsate as it settles back into hydrostatic equilibrium.

The subgiant follows a similar sequence, except that its more compact core alters the progress of the shock through the star and its larger envelope increases the timescale required to bring the remnant back into hydrostatic equilibrium. Because of its weakly-bound envelope, the impact on the red giant is quite different. The shock propagates through its more tenuous envelope and converges on its rearward side. All but a small fraction of the entire envelope is ejected, leaving a He pre-white dwarf surrounded by a halo of high-entropy hydrogen and helium.

We can summarize our results by stating that as a result of the impact of the supernova shell the main sequence companion loses 0.15 $M_{\odot}$ and the subgiant companion loses 0.17 $M_{\odot}$. In contrast, the red giant companions lose almost their entire envelopes, at least 0.53 $M_{\odot}$. The main sequence companion receives a kick of 86 km s^{-1}, the subgiant 49 km s^{-1}. In all cases, the kick received by the remnant is smaller than the original orbital velocity. Because it is too small to intercept more than a negligible amount of momentum, the red giant core will not receive an appreciable kick.

The characteristic velocity of the stripped hydrogen (half-mass point in the

distribution) is less than 10^3 km s^{-1} for all the scenarios. For the red giant case, the characteristic velocity is in the range $420 - 590$ km s^{-1}, depending on the scenario. For the main sequence and subgiant cases, the characteristic velocities are 850 km s^{-1} and 900 km s^{-1}, respectively. With such low velocities, the bulk of the stripped hydrogen and helium is embedded within the low-velocity iron of the supernova ejecta. The region behind the stellar remnant that is contaminated with stripped hydrogen is always much larger than the geometrical shadow, the solid angle subtended by the companion as seen from the site of the explosion. For the main sequence companions the stripped hydrogen extends as far as 66° away from the downstream axis and for the subgiant case as far as 72°. The hydrogen from the red giant contaminates a much larger solid angle, as far as 115° from the downstream axis. These angles correspond to fractions of the sky of 29%, 35%, and 71%. This is one distinction between the main sequence, the subgiant, and the red giant scenarios. The stripped hydrogen and helium is distributed over a much wider solid angle for the red giant scenarios. Despite the change in distribution of the stripped material, the hole in the supernova debris (of angular size $31° - 34°$) caused by the impact with the secondary is similar for all the scenarios.

If we define the efficiency of momentum transfer as the ratio of the momentum transferred to the stellar remnant to the incident momentum, then typical values for the main sequence simulations lie in the range of $0.2 - 0.5$, with the highest efficiency belonging to the secondary with the greatest binary separation. The characteristic velocity of the stripped material stays within $690 - 870$ km s^{-1}, with the material from the closest binary companions having the highest velocities. The closest binaries will also create the widest plume of stripped material.

One motivation for this project is the possibility of using the velocity

distribution of the stripped hydrogen and helium to discriminate between Type Ia progenitor models. However, to make any definitive predictions requires non-LTE radiative transfer calculations using the low-velocity distribution of the stripped material to determine the effect of hydrogen/helium contamination on the late-time supernova spectrum. Such calculations can determine the hydrogen and helium line strengths and ratios of narrow emission lines that will emerge months after the impact, as the photosphere recedes to reveal the low-velocity supernova ejecta where the bulk of the stripped material is located. Unfortunately, H_α is blended with numerous Fe and Co lines, especially [Co III] at 6578 Å, and will be difficult to identify. Because of atmospheric water absorption, a search for P_α ($1.87\mu m$) can not easily be conducted from the ground. Searches for P_β ($1.28\mu m$) can be conducted from the ground, but telluric absorption and a P_β emission line from the Earth's atmosphere require careful subtraction. Also, P_β is likely to be blended with a broad supernova Fe line at $1.26\mu m$. Other lines to look for are He lines at 5876 Å, $1.083\mu m$, and $2.05\mu m$ that will be distributed in velocity and angle like the hydrogen, but note that high-velocity helium is also present in sub-Chandrasekhar explosion models. With a complete study of the emergence of the narrow hydrogen and helium lines and the competing Fe and Co lines in the late-time supernova spectrum, an optimum time may be found when the hydrogen may be detected and used to distinguish one Type Ia supernova scenario from another.

Although most of the stripped material is ejected at low velocities, all the numerical simulations yield a small high-velocity tail. Above 3.0×10^3 km s^{-1}, all four scenarios have no more than $\sim 0.014\ M_\odot$ of high-velocity hydrogen. The HCVL simulation has $0.014\ M_\odot$, followed by the HALGOLa with $0.012\ M_\odot$, the HCV with $0.010\ M_\odot$, and lastly, the SYMB simulation with only $0.004\ M_\odot$. Above

10^4 km s^{-1}, the amount of high-velocity hydrogen has dropped by a factor of 10 for all four scenarios. In this velocity range ($3.0 \times 10^4 - 10^4$ km s^{-1}), we can easily discriminate between the companions in Roche lobe overflow and a model in which the red giant that is too distant to be in Roche lobe overflow, our SYMB scenario. Above 1.5×10^4 km s^{-1}, the HALGOLa and the SYMB scenario have the most high-velocity hydrogen: the HALGOLa with 3.3×10^{-4} $M_\odot$ and the SYMB with 3.0×10^{-4} $M_\odot$. We note that even if the red giant companions have more low-velocity hydrogen, they have substantially more hydrogen above 1.5×10^4 km s^{-1} than the main sequence or subgiant models. Because the HCVL has more high-velocity hydrogen than the HCV scenario, we can discriminate between the subgiant and main sequence companions at 1.5×10^4 km s^{-1}.

The Della Valle et al. (1996) observational upper limit from SN 1990M corresponds to a total hydrogen mass of $\sim 3 \times 10^{-4}$ $M_\odot$. If this hydrogen is mixed only within the observable photosphere, then the main sequence, subgiant, and the red giant models are just under this upper limit. However, if the upper limit were reduced by only a factor of 3, the red giant and subgiant models would clearly exceed this limit, while the main sequence model is marginal. With this interpretation, the high-velocity tail of SN 1990M can not yet be used to exclude any progenitor models with hydrogen-rich companions.

The impact of the supernova ejecta on the secondary star creates a oddly shaped, small gap in the supernova debris. The highest velocity debris flows around the secondary, creating a narrow gap of angle $\sim 31 - 34°$. The lower velocity supernova material flows through the bow shock, creating a wider gap in the inner ejecta of angle $\sim 40°$. Therefore, the hole in the supernova is narrow at the outside of the shell, broad at the inside of the shell, and filled with high-velocity

stripped material from the companion. As discussed above, most of the stripped material fills a wide solid angle and trails behind the supernova debris. Because the supernova flow is supersonic, the hole in the debris will not close with time. However, the orbital motion of the main sequence and subgiant secondaries will add a small component of velocity ($100 - 200$ km s^{-1}) tangential to the axis of the original binary system that will slowly distort the shape of the slow-moving contaminated region behind most of the supernova debris. The evolution and mixing of the hydrogen-filled region become a 3-D problem.

We use the angular size of the hole as an estimate of the region of asymmetry in the supernova ejecta caused by the impact on the companion star. The angular size of the gap in the supernova debris depends on the binary scenario. A typical angular size for the gap in the high-velocity material is $31° - 34°$, which corresponds to only $7 - 8\%$ of the ejecta's surface. The main sequence model has the smallest gap, the subgiant has a slightly larger gap, and the red giant has the largest gap. The typical angular size for the gap in the low-velocity ejecta is $\sim 40°$, independent of the model. This corresponds to 12% of the surface area of the ejecta. Because the binary scenarios we explore are all close enough, or almost close enough, to be in Roche lobe overflow, the degree of asymmetry is similar for all the models. Asymmetry in the supernova ejecta will indicate the presence of a companion star, but it will be difficult to use the degree of asymmetry alone to discriminate between main sequence, subgiant, and red giant companions.

The asymmetry in the supernova debris could have observational consequences beyond the change in morphology of the supernova remnant. In the early-time spectra, subtle distortions may appear in the P Cygni lines that are dependent on the orientation of the hole in the supernova debris relative to the observer.

For example, if the gap lies towards the observer, the P Cygni lines may have a distorted blue wing. If the gap lies at some angle away from the observer, the P Cygni lines may have a distorted red wing. However, because the hole in the supernova debris subtends such a small solid angle, its effect on the spectra will be equally small. The asymmetry may also affect the polarization of the supernova debris to some degree.

The impact of the supernova shell will also have consequences for the future evolution of secondary star. After the impact, the main sequence star is puffed up, much like a pre-main sequence star. Although the energy generation rate during the impact shoots up by a factor of $\sim$ 1000, it immediately plummets as the star expands and cools. Hydrogen burning in the core will be nearly extinguished, but the luminosity will rise dramatically, to as high as $\sim 5000\ L_{\odot}$, as the extended envelope relaxes back into thermal equilibrium and then follows a Kelvin-Helmholtz track on a timescale of $\sim 10^4$ yrs. The supernova is initially much more luminous with L$\sim 10^9\ L_{\odot}$. However, after $2-3$ years, the supernova luminosity will have decayed enough that a very bright secondary might be visible. After thermal equilibrium is reestablished and the residue has settled back onto the main sequence, the remnant will continue its evolution at a rate prescribed by its new mass. The 1.0 $M_{\odot}$ main sequence secondary will eventually return to the main sequence with a mass of 0.85 $M_{\odot}$, having lost 0.15 $M_{\odot}$ due to the impact, with a slightly smaller radius of 0.9 $R_{\odot}$, and a luminosity of $\sim 0.4\ L_{\odot}$. The subgiant puffs up after the impact and must contract to reignite hydrogen shell-burning, which has been extinguished during the subgiant's expansion. Like the main sequence case, the luminosity will be high during this phase.

A He pre-white dwarf will be left after a supernova explosion with a red giant

companion. Almost all the envelope will be ejected by the impact, but a residual amount of material will form an extended, hydrogen-rich envelope around the degenerate core. This extended envelope of $\sim 0.02\ M_{\odot}$ of hydrogen-rich material will settle down onto the star to feed the hydrogen burning shell. The star will evolve away from the red giant branch at constant luminosity and increasing effective temperature on a timescale of $10^5 - 10^6$ years. Before the luminosity drops, it may appear as an underluminous O or B star. When the star begins to dim and cool, it may pass through an sdO or sdB phase before retiring along a standard He white dwarf cooling track. This binary scenario could be a possible pathway for the formation of a subset of single, low-mass He white dwarfs.

The metallicity of the secondary may increase if it accretes any supernova material as a result of the explosion. We do not expect that the secondary star will accrete a significant amount of supernova material by the direct impact of the supernova shell on the surface of the star because, as the shock created by the impact propagates through the stellar envelope, the shock-heated material escapes the secondary, carrying away any impinging supernova material. However, this does not necessarily mean that the secondary will not accrete any low-velocity iron-group elements (or oxygen and silicon if the ejecta is radially mixed) long after the initial impact.

High resolution late-time observations focused on detecting stripped hydrogen and helium from the companion star are needed to verify the single-degenerate scenario. With non-LTE synthetic spectra, such observations may be used to discriminate between the main sequence, the subgiant, and the red giant companions. Asymmetry in the supernove ejecta, distorted P Cygni lines or line ratios, and slight polarization may also indicate an unseen companion star.

Our theoretical study was performed in support of the quest to to unravel the persistent mystery of the site of Type Ia supernova explosions. Given the emerging cosmological importance of such expolosions as standardizable candles and the resulting renaissance in their study, the time is ripe for a renewed investigation into the consequences of the variety of binary scenarios for thermonuclear supernovae.

Appendix A

Color Plates

Figure A.1 Frames (a)-(d) illustrate the impact of supernova Type Ia W7 on a 1.0 $M_{\odot}$ main sequence companion at 29, 104, 179 and 329 seconds after the explosion. The color scale indicates $\mathrm{Log}_{10}\rho$: blue $\sim$ 160.0 gm cm^{-3} $\rightarrow$ red $\sim$ 10^{-13} gm cm^{-3}. The explosion occurs off the grid at a distance consistent with the companion losing mass to the white dwarf primary by Roche lobe overflow. Frame (a) shows the companion star at the origin of the grid at 29 seconds, just prior to the impact of the debris. In Frame (b), at 104 seconds, the leading edge of the supernova shell has just collided with the surface of the companion. By 179 seconds (Frame (c)), the leading edge of the supernova shell converges along the downstream axis. The companion is now enveloped in the supernova ejecta. Frame (d), at 329 seconds, shows the shock wave that was driven into the companion by the impact and the bow shock just upstream of the companion. MPEG movies and 2-D images are posted at http://www.astrophysics.arizona.edu and are available via anonymous FTP from www.astrophysics.arizona..edu, in directory pub/marietta.

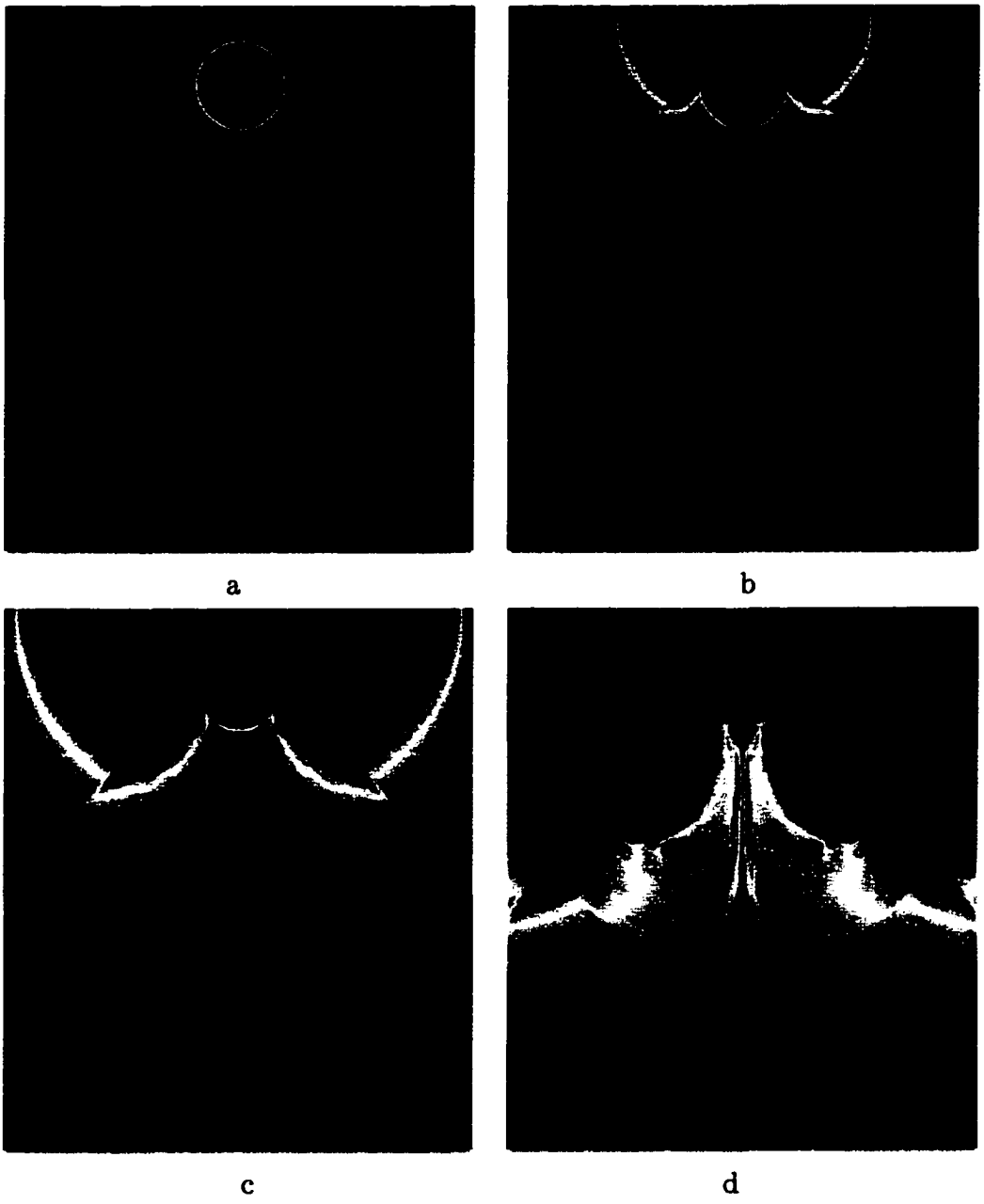

a b

c d

Figure A.2 Frames (a)-(d) illustrate the impact of supernova Type Ia W7 on a 1.0 $M_{\odot}$ main sequence companion at 529, 755, 2029 and 2033 seconds after the explosion. The color scale is the same as in Figure A.1. In Frame (a) the shock has just passed through the stellar core. In Frame (b) the shock has converged within the star along the downstream axis. Kelvin-Helmholtz and Rayleigh-Taylor instabilities are visible in both frames. Frame (c) illustrates the end of the mass stripping phase. By Frame (d), several dynamical times have passed, and the remnant is beginning to recover hydrostatic equilibrium.

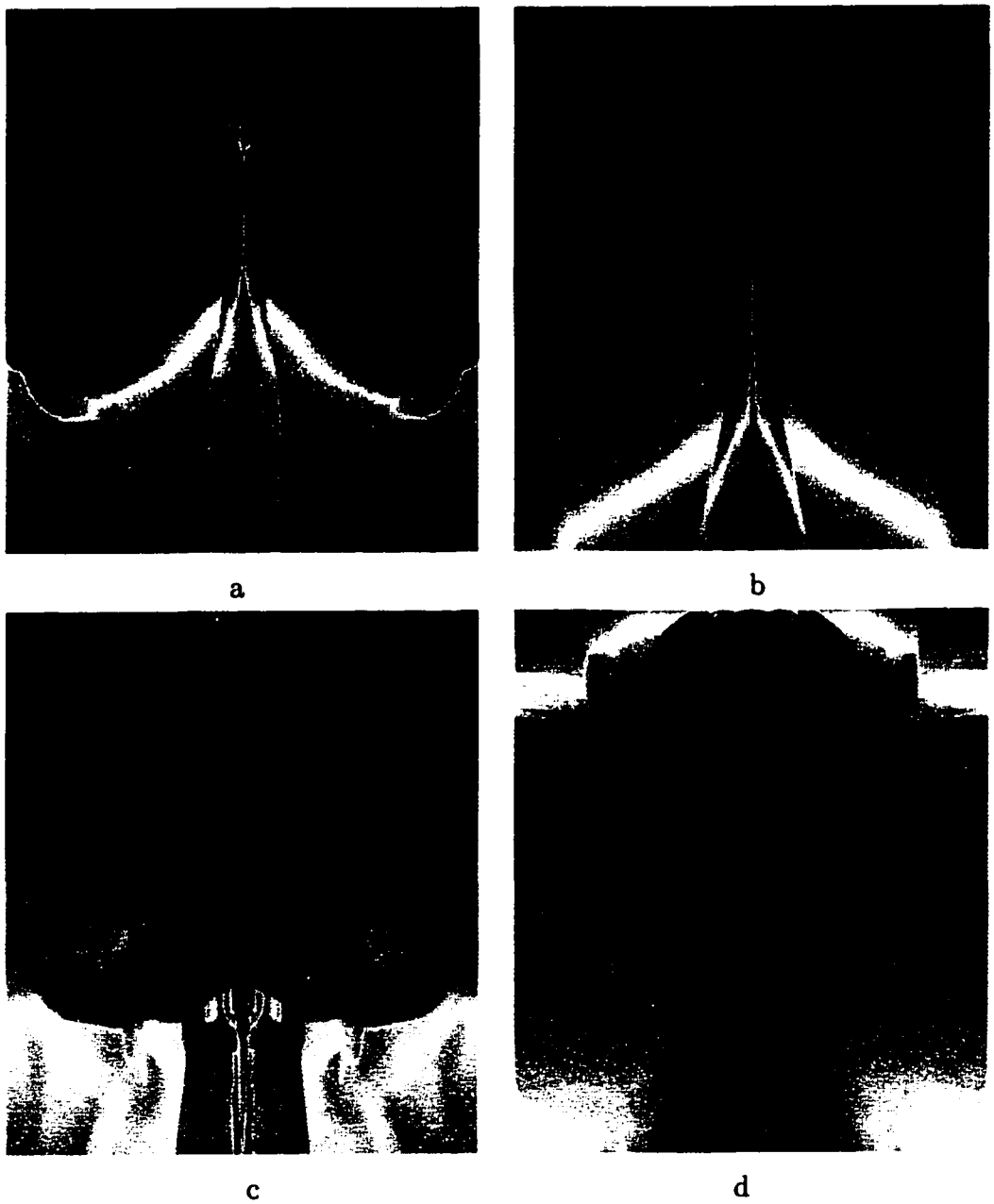

a b

c d

Figure A.3 Frames (a)-(f) illustrate the impact of supernova Type Ia W7 on a 1.0 $M_{\odot}$ main sequence companion in a series of cartoon images, each color indicating the dominant element in that region. For clarity each region is also numbered: (1) circumstellar medium, (2) stellar hydrogen, (3) supernova oxygen-group elements, (4) supernova silicon, and (5) supernova iron-group elements. The frames shown are at 104, 179, 329, 529, 755, and 2029 seconds after the explosion. Frames (a) and (b) show the initial impact. The oxygen, silicon, and iron layers of the supernova ejecta are clearly visible. Frames (c) and (d) illustrate the beginning of the mass stripping phase when the outermost layer of the companion's envelope is stripped and caught in the oxygen and silicon layers of the supernova ejecta. By Frame (e), any mass lost from the companion's envelope is embedded within the iron region of the supernova ejecta. Frame (f) shows the end of the mass stripping phase. The envelope of the companion is now extended; about 15% of the mass will escape the companion and follow the flow of the supernova.

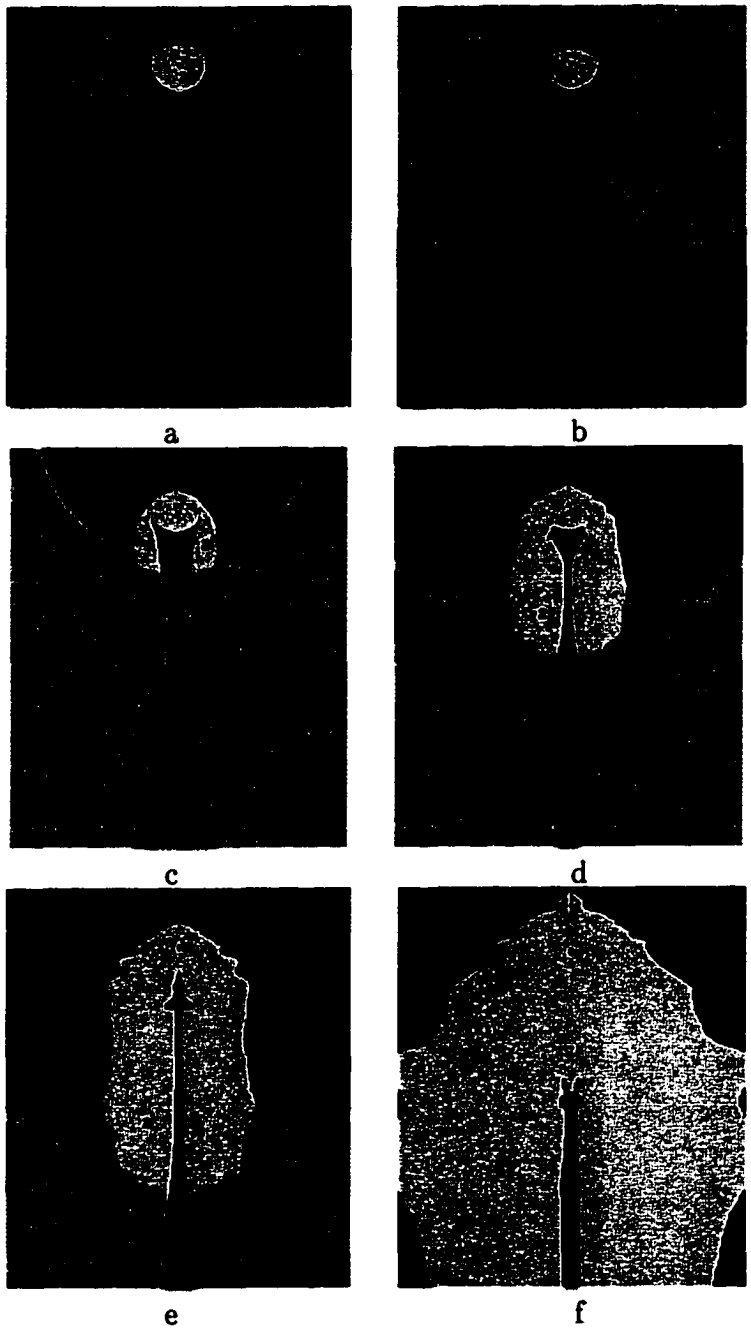
a
b
c
d
e
f

Figure A.4 Frames (a)-(d) illustrate the impact of supernova Type Ia W7 on a 1.0 $M_{\odot}$ main sequence companion for different binary separations: simulations HCV, HCVb, HCVc, and HCVd. The color scale indicates $\mathrm{Log}_{10}\rho$: blue $\sim$ 160.0 gm cm^{-3} $\rightarrow$ red $\sim 10^{-13}$ gm cm^{-3}. This color scale is the same as in Figure A.1. Frame (a) shows the impact for a ratio $a/R = 3.0$ (binary separation over stellar radius) at 1031 seconds after the explosion. This is our HCV simulation. Frame (b) shows the impact with $a/R = 4.0$ at 1336 seconds after explosion, the HCVb test case. Frame (c) shows the impact with $a/R = 6.0$ at 1197 seconds, and Frame (d) with $a/R = 12.0$ at 1308 seconds. The timesteps are increasing primarily because the length of time needed for the supernova ejecta to reach the secondary is increasing.

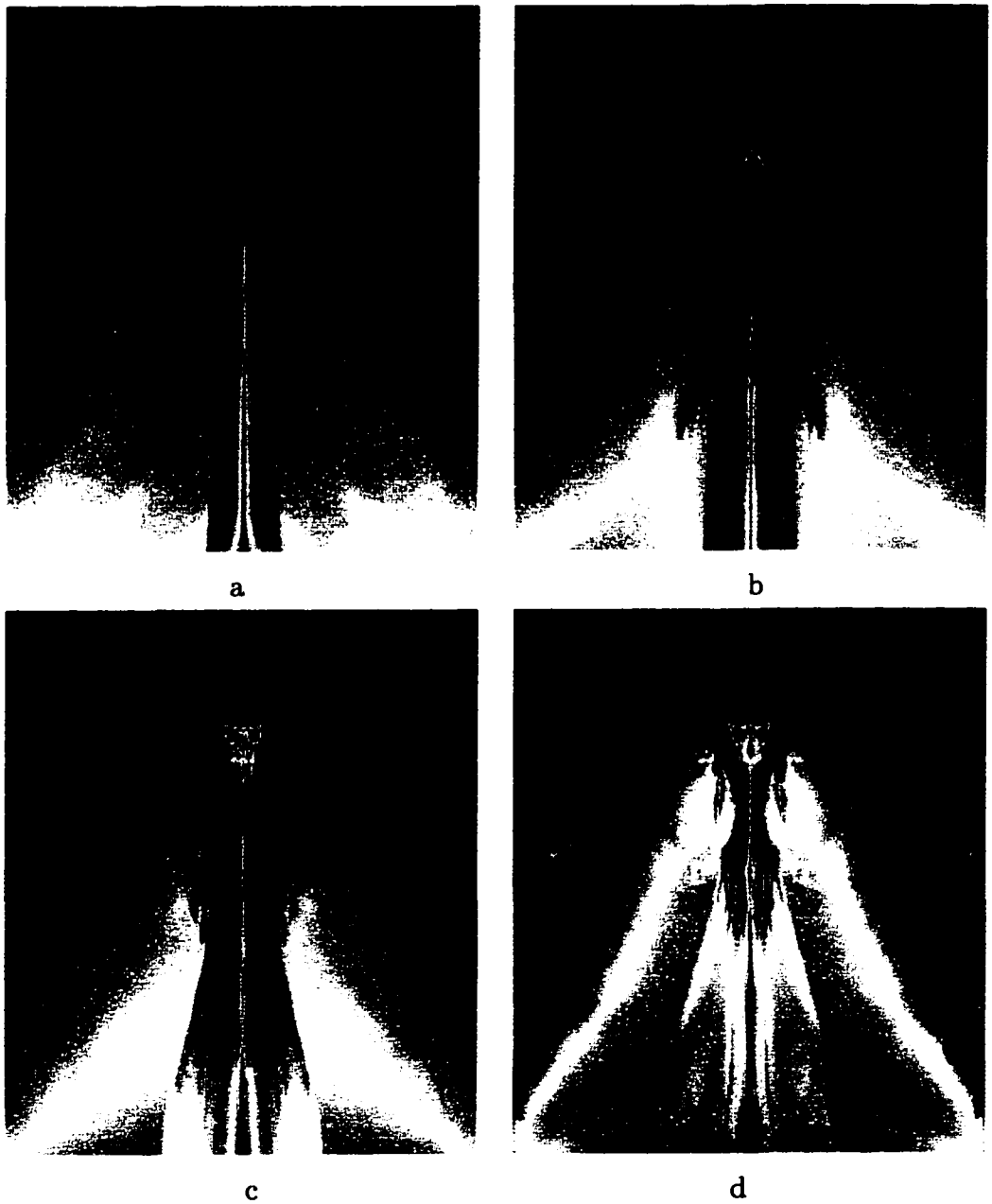

a b

c d

Figure A.5 Frames (a)-(d) illustrate the impact of supernova Type Ia W7 on a 1.13 $M_{\odot}$ subgiant companion at 343, 945, 2044 and 20044 seconds after the explosion. The color scale indicates $\mathrm{Log}_{10}\rho$: blue $\sim 2.7\times10^{3}$ gm cm^{-3} $\rightarrow$ red $\sim 10^{-13}$ gm cm^{-3}. The explosion occurs off the grid at a distance consistent with the companion losing mass to the white dwarf primary by Roche lobe overflow. Frame (a) shows the subgiant and the incoming supernova shell 343 seconds after the explosion. Only 0.06 $M_{\odot}$ of the companion's envelope has been stripped by this time. In Frame (b) at 945 seconds, the shock has just propagated through the subgiant's core and is about to converge in the back of the subgiant. Frame (c) shows the subgiant in the last stages of mass loss. The subgiant has lost 0.15 $M_{\odot}$ of its envelope which can be seen streaming away from the subgiant. By Frame (d), 20044 seconds after the explosion, the remnant of the subgiant is recovering hydrostatic equilibrium.

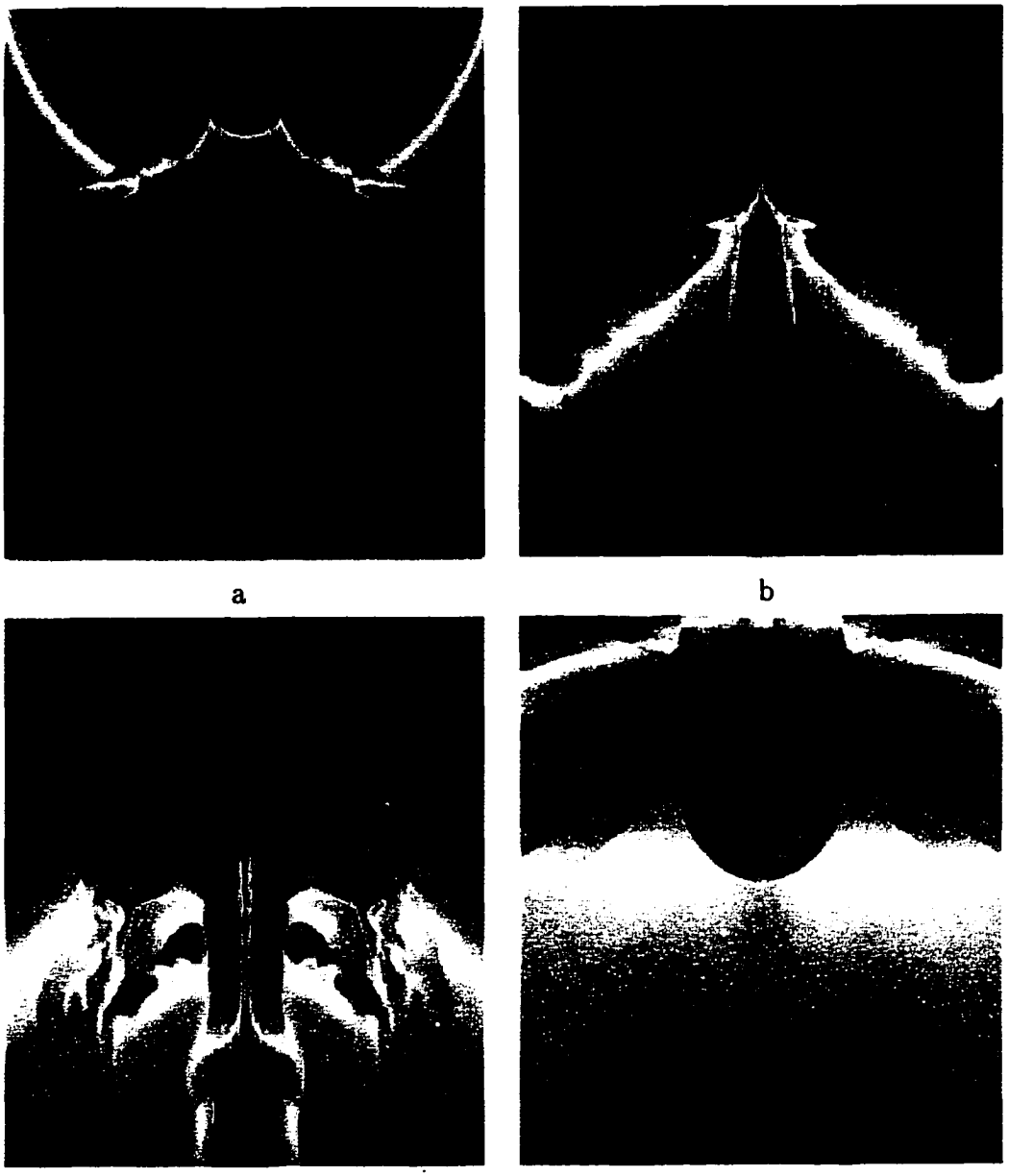

a b

c d

Figure A.6 Impact of supernova Type Ia W7 on a 1.13 $M_{\odot}$ subgiant companion at 1958 seconds near the end of the mass stripping phase. The Kelvin-Helmholtz instabilities, which help the hot material to escape the surface, are easily seen in this image. The color scale is the same as in Figure A.5.

Figure A.7 Frames (a)-(d) illustrate the impact of supernova Type Ia Hedt on a 0.98 $M_{\odot}$ red giant companion at 8.7 hrs, 14.3 hrs, 2.1 days and 5.9 days after the explosion. Only the region around the red giant is shown to emphasize the interaction. The full images are shown in Figures A.8.

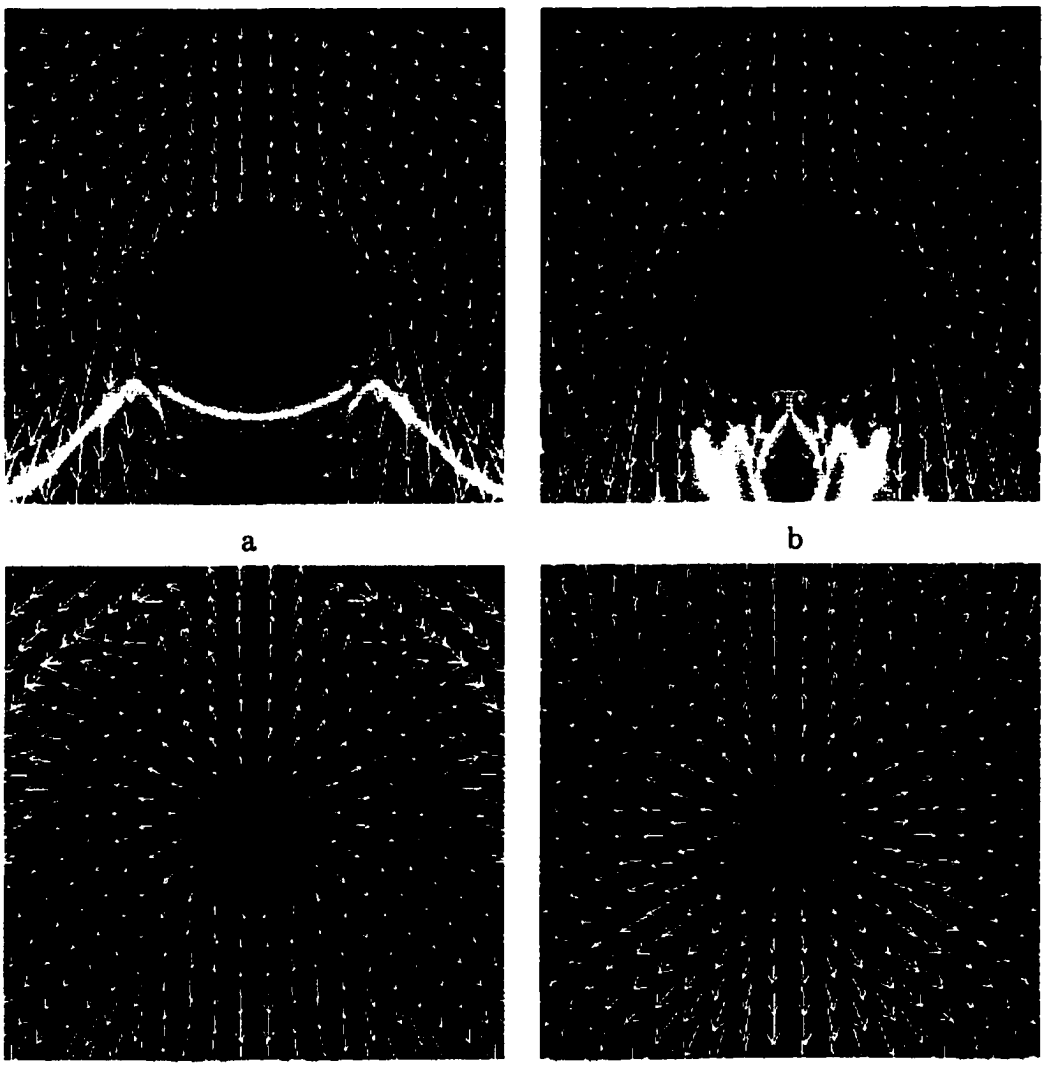

a b

c d

Figure A.8 Frames (a)-(d) illustrate the impact of supernova Type Ia Hedt on a 0.98 $M_{\odot}$ red giant companion at 8.7 hrs, 14.3 hrs, 2.1 days and 5.9 days after the explosion. In these images the supernova can been seen exploding on the grid. These are the full images corresponding to the images in Figures A.7.

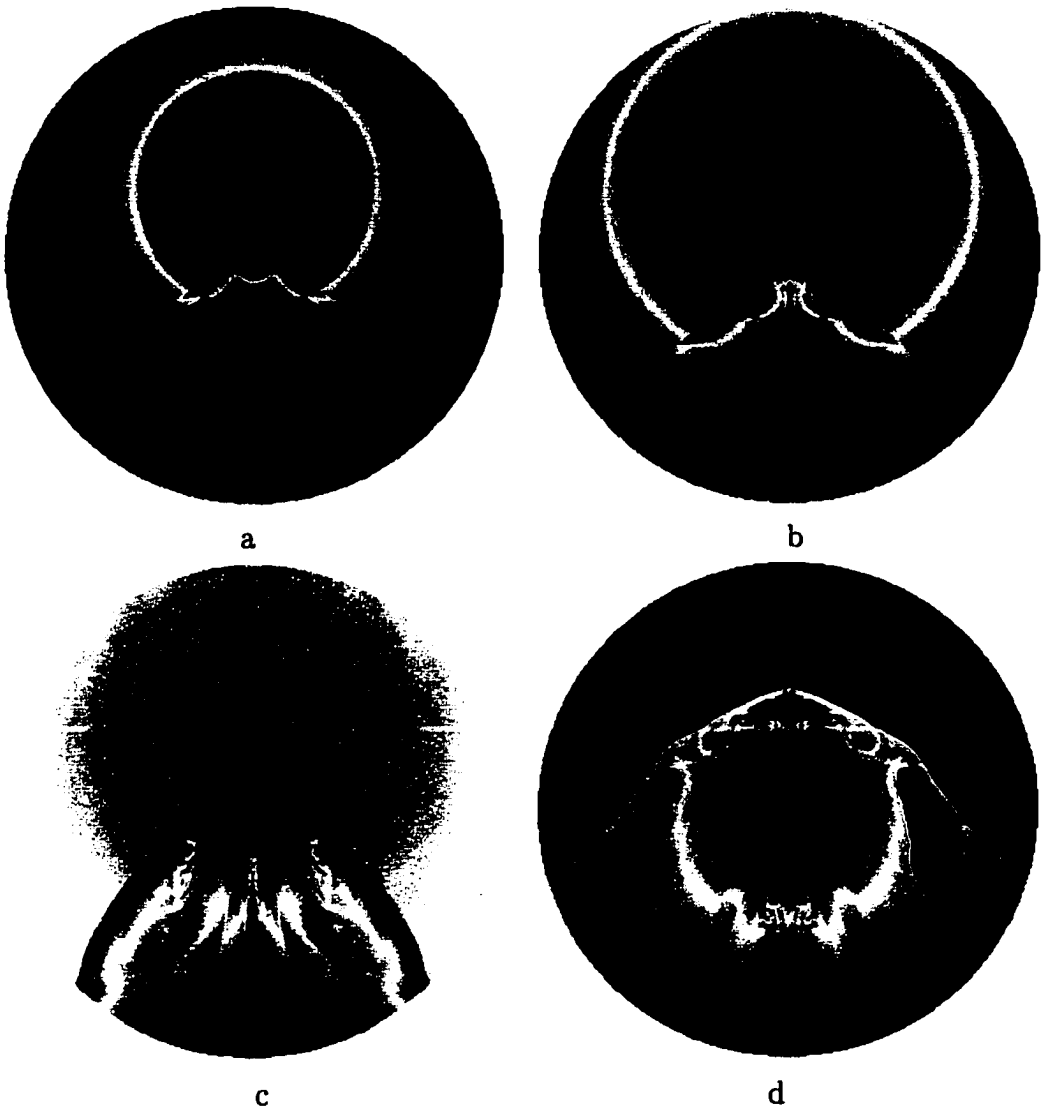

a b c d

Appendix B

Nuclear Energy Generation Estimate

For a quick estimate of the energy generation rate, we calculate the hydrogen burning rate via the three PP chains and the CNO cycle. For the combined rate of the PP1, PP2, and PP3 chains (Clayton 1983)

$$\epsilon_{PP123} = 2.36 \times 10^6 \rho\, X_H^2\, \Psi\, T_6^{-2/3} \exp^{-33.81 T_6^{-1/3}}\, g(T) \;\; \text{ergs s}^{-1}\,\text{gm}^{-1} \qquad \text{(B.1)}$$

with

$$g(T) = 1.0 + 0.0123 T_6^{1/3} + 0.0109 T_6^{2/3} + 0.00095 T_6,$$

where Ψ represents the correction to the energy generation rate of the PPI branch from the energy released simultaneously by the PP2 and PP3 branches. For simplicity, we use a quick approximation for Ψ as shown in Figure B.9 which mimics the actual behavior of Ψ (Parker et al. 1964). For the CNO cycle (Kippenhahn & Weigert 1991)

$$\epsilon_{CNO} = 8.67 \times 10^{27} \rho X_H X_{CNO} T_6^{-2/3} \exp^{-152.28 T_6^{-1/3}}\, H(T) \;\; \text{ergs s}^{-1}\,\text{gm}^{-1} \qquad \text{(B.2)}$$

with

$$H(T) = 1.0 + 0.0027 T_6^{1/3} - 0.00778 T_6^{2/3} - 0.000149 T_6.$$

Figure B.10, which can be compared to Figure 18.8 of Kippenhahn & Weigert (1991), illustrates the total energy generation rate and the contributions from the PP chains and the CNO cycle for a medium with $X_{CNO} = 0.01$ and a density of 1.0 gm cm^{-3}. As expected, at low temperatures the rate is dominated by the PP chain. The CNO cycle turns on at $\sim 10^{7.2}$K. Above that, the hydrogen burning rate climbs so dramatically that we can not neglect the CNO cycle.

To verify that ϵ_{PP123} and ϵ_{CNO} can reproduce the luminosity of our main sequence star, we integrate the energy generation rate over the 1.0 main sequence secondary. Figure B.11 shows that most of the 1.038 $L_\odot$ luminosity is produced in the inner 0.3 of mass. Having shown that we can reproduce the original luminosity

to within a few percent, we can calculate the energy generation of the companion during the impact.

For a quick estimate of the effect of the impact on the nuclear energy generation rate of the main sequence companion, we assume spherical symmetry and calculate the hydrogen burning rate along a 1-D cut through the densest (and hottest) part of the companion during the interaction. As can be seen in Figure 4.8, the energy generation rate shoots up by a factor of 1000 as a result of the shock-heating, then immediately drops precipitously as the star expands. Despite the extremely high energy generation rate, only a small amount of additional energy is deposited in the center of the star because the compression phase is so brief. For the main sequence star an additional $\sim 10^{38}$ ergs has been deposited which is extremely small in comparison with the binding energy of the star ($\sim 10^{48}$ ergs). By the end of the simulation, the energy generation rate is only $7 \times 10^{-2}\ L_{\odot}$. Hydrogen burning has been quenched by the impact.

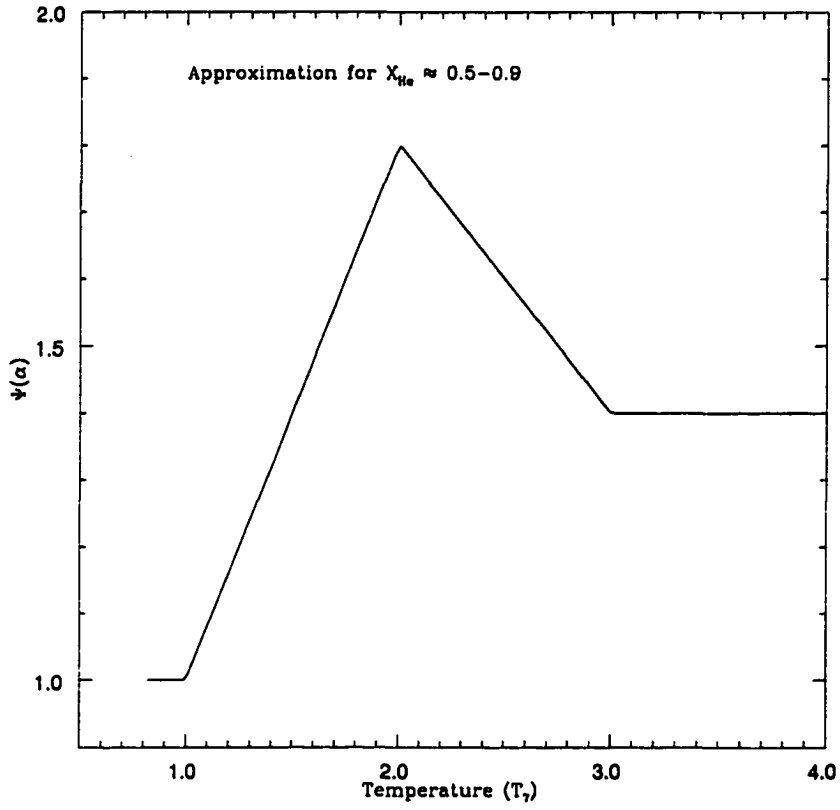

Figure B.9 Approximation for Ψ, the correction to the energy generation rate of the PPI branch from the energy released simultaneously by the PP2 and PP3 branches.

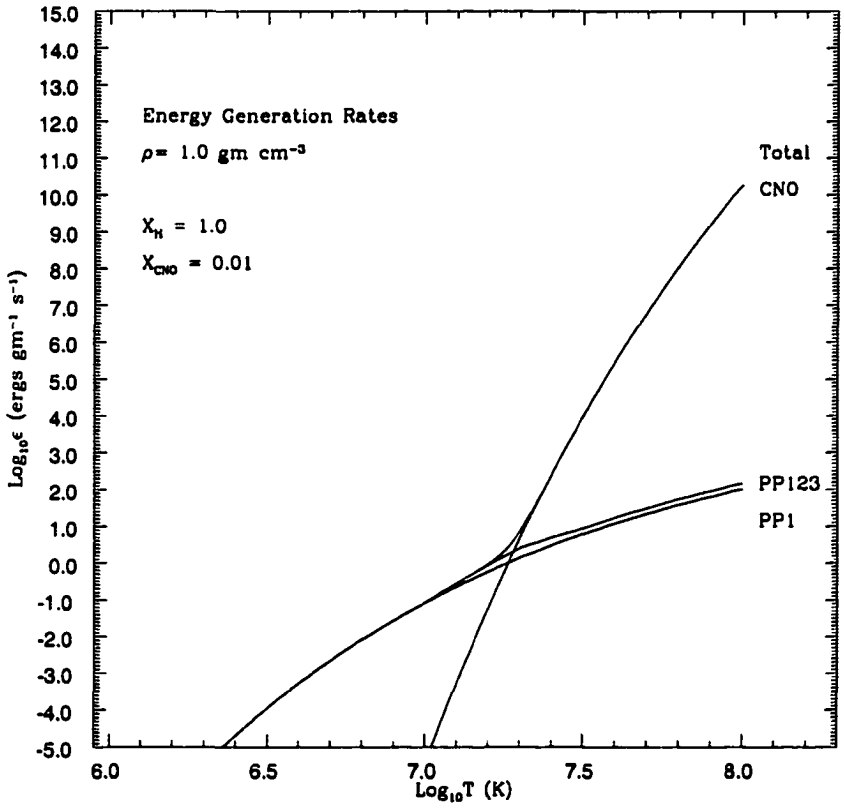

Figure B.10 Total energy generation rate and the contributions from the PP chains and the CNO cycle for a medium with a $X_{CNO} = 0.01$ and a density of 1.0 gm cm^{-3}. Compare with Figure 18.8 of Kippenhahn & Weigert (1991).

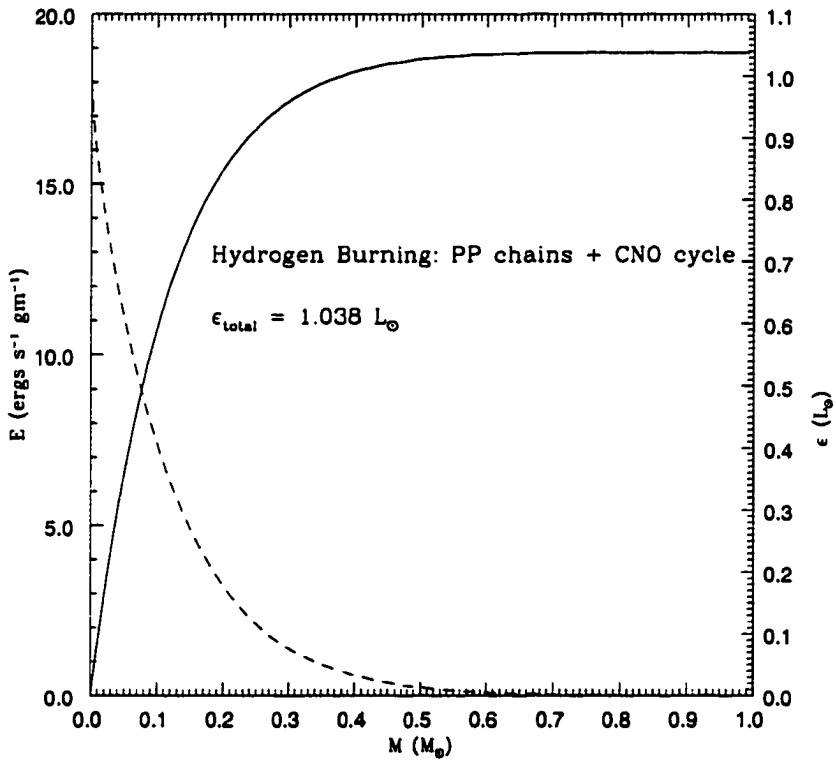

Figure B.11 Energy generation rate and luminosity for a 1.0 $M_\odot$ main sequence star using ϵ_{PP123} (B.1) and ϵ_{CNO} (B.2). The solid line indicates the luminosity. The dashed line indicates the energy generation rate.

Appendix C

Equation of State

For most simulations of the supernova-secondary interaction we use ideal gas and radiation for the equation of state. When degenerate electrons are required in the core of an evolved star, we utilize a tabulated equation of state for the electrons (and positrons, if present) from which we can extract their pressure and energy density based on the density, composition, and temperature of the fluid.

We tabulate the pressure, energy density and entropy of the ionization electrons and pair-produced electrons and positrons for arbitrary degeneracy and relativity in the most direct method possible, following the conventions of Cox & Giuli (1968). Using the ionization electron density $\rho Y_e N_{Av}$ and the temperature as independent variables, we used an bisection technique (Press et al. 1992d) to solve for the degeneracy factor ($\eta = \mu/kT$). Having found the degeneracy based on the ionization electron density and temperature, we find the relativity factor ($\beta = kT/mc^2$) from the temperature and tabulate the thermodynamic variables by directly integrating the appropriate Fermi-Dirac integrals $F_k(\eta,\beta)$. Using $\eta^* = -\eta - 2/\beta$ to simplify the notation for the positron contribution, the equations to be solved are the ionization density ($n_e = n_- - n_+$)

$$n_e = \left(\frac{8\pi}{h^3}\right)\sqrt{2}\beta^{3/2}\left(mc^3\right)\left(F_{1/2}(\eta,\beta) + \beta F_{3/2}(\eta,\beta) - F_{1/2}(\eta^*,\beta) - \beta F_{3/2}(\eta^*,\beta)\right), \tag{C.3}$$

the electron and positron pressures

$$\begin{aligned} P_- &= \left(\frac{8\pi}{3h^3}\right)\left(m^4c^5\right)2^{3/2}\beta^{5/2}\left(F_{3/2}(\eta,\beta) + \frac{1}{2}\beta F_{5/2}(\eta,\beta)\right), \\ P_+ &= \left(\frac{8\pi}{3h^3}\right)\left(m^4c^5\right)2^{3/2}\beta^{5/2}\left(F_{3/2}(\eta^*,\beta) + \frac{1}{2}\beta F_{5/2}(\eta^*,\beta)\right), \end{aligned} \tag{C.4}$$

and the energies

$$E_- = \left(\frac{8\pi}{h^3}\right)\left(m^4c^5\right)2^{1/2}\beta^{5/2}\left(F_{3/2}(\eta,\beta) + \beta F_{5/2}(\eta,\beta)\right),$$

(C.5)

$$E_+ = \left(\frac{8\pi}{h^3}\right)\left(m^4c^5\right)2^{1/2}\beta^{5/2}\left(F_{3/2}(\eta^*,\beta)+\beta F_{5/2}(\eta^*,\beta)\right),$$

and

$$E_{rest} = \left(\frac{8\pi}{h^3}\right)\left(m^4c^5\right)2^{3/2}\beta^{3/2}\left(F_{1/2}(\eta^*,\beta)+\beta F_{3/2}(\eta^*,\beta)\right), \qquad (C.6)$$

where E_{rest} represents the rest mass energy required in the production of electron-positron pairs. The last quantity we calculate is the electron-positron entropy

$$S = (P_- + P_+ + E_- + E_+ + E_{rest})/kT - \eta n_e \qquad (C.7)$$

per Boltzmann's constant per volume.

In essence, this method requires the general Fermi-Dirac integral

$$F_k(\eta,\beta) = \int_o^\infty \frac{x^k(1+\frac{1}{2}\beta x)}{(e^{-\eta+x}+1)}dx \qquad (C.8)$$

for arbitrary η and β. We employ Romberg Integration and Laguerre Quadrature to solve the Fermi-Dirac integral, by selecting the method most appropriate in each $\eta - \beta$ regime and expressing the integrand in its limiting forms (degenerate, non-degenerate), when appropriate.

The simplest table would consist of the thermodynamic quantities expressed as a function of $\log_{10}(\rho Y_e)$ along one axis and $\log_{10}T$ along the other. However, as can be seen from Figure C.12, when the temperature increases (for fixed density and composition) the pressure rises dramatically as pair production begins (T $\approx 6 \times 10^9$). We estimate that such a table covering $-6.0 < \log_{10}(\rho Y_e) < 12.0$ and $3.0 < \log_{10}T < 12.8$ would require approximately a 400×2000 spacing for a total of 8×10^5 grid points. This fine spacing would be necessary to ensure at least 10^{-5} accuracy in the pair production region ($8.0 < \log_{10}T < 10.0$) when used in conjunction with a second-order interpolation scheme.

To maintain accuracy over the entire table, without oversampling the degenerate region, we select a function of temperature to serve as the second axis to ensure that the positron turn-on is well-sampled. After experimentation with many functional forms we selected

$$u(v) = (\arctan v/b)\,/b + kv \tag{C.9}$$

where $v = \log_{10}\mathrm{T} - v_c$ and b and k are constants. The advantage of this function is that, when $u(v)$ is uniformly sampled, the spacing in $\log_{10}\mathrm{T}$ is densest at v_c, which we select to be 9.6 in the positron regime. The equation of state table is therefore calculated as a function of (u, w), u being the above function and w being $\log_{10}(\rho \mathrm{Y}_e)$.

We create a selection of tables (see Table C.1) with grid spacings from 200×200 to 600×600 covering $\rho \mathrm{Y}_e$ from -6.0 to 12.0 and $\log_{10}\mathrm{T}$ from 3.0 to 12.8. Although increasing the number of grid points will always increase the resolution, memory limits constrain the number of grid points that are practical. The smallest table uses 200×200 grid points and requires 2.5 Mbytes. In contrast, the largest table, 600×600, requires 22.7 Mbytes. To minimize numerical problems associated with any pressure or energy discontinuities between the table and off-table approximations, we deliberately employ an extremely broad range of temperatures and densities. Approximations for the electron equation of state outside of the tabulated range must still be added to the interpolation routines in case any iterative search makes an excursion off the table.

The electron equation of state exterior to the table is estimated by replacing the Fermi-Dirac integrals with series expansions in η or β, the form of the expansion depending on the limiting case. For extreme degeneracy and relativity ($\eta >> 1; \beta >> 1$) we employ the Sommerfeld expansion to express the ionization

electron density n_e as a cubic function

$$\eta^3 + \pi^2\eta - n_e\left(\frac{3}{8\pi}\right)\left(\frac{hc}{kT}\right)^3 = 0, \tag{C.10}$$

which can be analytically inverted for η. The pressure and energy

$$\begin{aligned} P &= \left(\frac{2\pi}{3}\right)\left(\frac{kT}{hc}\right)^3 kT\,\eta^4\left(1+\frac{2\pi^2}{\eta^2}+\frac{7\pi^4}{15\eta^4}\right), \\ E &= 3P \end{aligned} \tag{C.11}$$

can be directly solved without a direct integration of the Fermi-Dirac integrals. In the non-relativistic, but extremely degenerate, region ($\eta >> 1; \beta << 1$) we follow a similar procedure. In this case,

$$\eta^3 + \left(\frac{\pi^2}{4}\right)\eta - \left(\frac{3}{16\sqrt{2}\pi}\right)^2\left(\frac{h^2}{mkT}\right)^3 n_e^2 = 0 \tag{C.12}$$

and

$$\begin{aligned} P &= \left(\frac{16\sqrt{2}\pi}{3}\right)\left(\frac{m^{3/2}(kT)^{5/2}}{h^3}\right)\left(\frac{2}{5}\right)\eta^{5/2}\left(1+\frac{5\pi^2}{8\eta^2}-\frac{7\pi^4}{384\eta^4}\right), \\ E &= \frac{3}{2}P. \end{aligned} \tag{C.13}$$

If the electrons are degenerate, but only partially relativistic, we take advantage of of the series expansion provided by Cox & Giuli (1968), pg 849 which expands the electron ionization density, pressure, and energy as

$$n_e = \frac{8\pi}{3}\frac{(mc)^3}{h^3}x^3, \tag{C.14}$$

$$P = \frac{\pi m^4 c^5}{3h^3}f(x), \tag{C.15}$$

$$E = P\frac{g(x)}{f(x)}$$

with $f(x) = x(x^2+1)^{1/2}(2x^2-3) + 3\ln(\sqrt{1+x^2}+x)$ and $g(x) = 8x^3(\sqrt{1+x^2}-1) - f(x)$ in terms of the Fermi momentum as $x = p_F/mc$ (Chandrasekhar 1957). Finally, in the non-degenerate domain ($\eta << 1$) we assume ideal gas ($P = n_e kT; E = 3/2P$).

We estimate the accuracy of the table and its interpolation routines by comparing the pressure from the Fermi-Dirac integration to the interpolated values from the table at a selection of density and temperature points that are not grid points of the table. Figure C.13 shows the fractional error as a function of temperature for a selection of $\log_{10}(\rho Y_e)$ slices through the table for the 600 × 600 table. Figure C.14 shows the same slices for the 400 × 400 table. Over much of the table, the error is between $10^{-5} - 10^{-6}$. The largest error at high temperatures is at the highest densities where the positrons don't turn-on until $\log_{10}$T> 9.6. At low temperatures near the edge of the grid, which for this table is 10^3 K, the error rises dramatically for low densities as the interpolation routine moves to inaccurate off-table approximations. To avoid this problem, we create an additional table with a minimum temperature of 10 K. We find the errors remain almost the same in the high temperature region of the grid. This is our preferred table.

Table C.1. Equation of State Tables

Resolution	Mbytes	$\log_{10}(\rho Y_e)$	$\log_{10}T$	Fractional Error
200 × 200	2.5	-6.0, 12.0	3.0, 12.8	$< 10^{-4}$
400 × 200	5.0	-6.0, 12.0	3.0, 12.8	$< 10^{-4}$
200 × 400	5.0	-6.0, 12.0	3.0, 12.8	$< 10^{-4}$
400 × 400	10.0	-6.0, 12.0	3.0, 12.8	$< 10^{-5}$
600 × 600	22.7	-6.0, 12.0	1.0, 12.8	$< 10^{-5}$
600 × 600	22.7	-6.0, 12.0	3.0, 12.8	$< 10^{-5}$

Figure C.12 Electron-Positron & Radiation Equation of State. The heavy solid lines illustrate the temperature dependence of the pressure for a selection of ρY_e values, which represents the ionization electron number density when multiplied by Avogadro's number. The pressure from the electrons, positrons, and radiation is included, the pressure from the ions is not. The horizontal region of each pressure profile corresponds to the degenerate region of the table. As the temperature rises, the degeneracy is lifted, and the slight incline of the pressure profile now corresponds to the ideal gas region of the table. At higher temperatures the pressure rises rapidly until the fluid is radiation-dominated. All the profiles converge at the radiation-dominated region as the dependence on the electron number density disappears. The light solid lines illustrate the degeneracy contours. Running almost, but not quite, parallel to the degeneracy contours are the entropy contours, shown as dashed lines. The entropy is in units of entropy k_B^{-1} baryon^{-1} Y_e^{-1}.

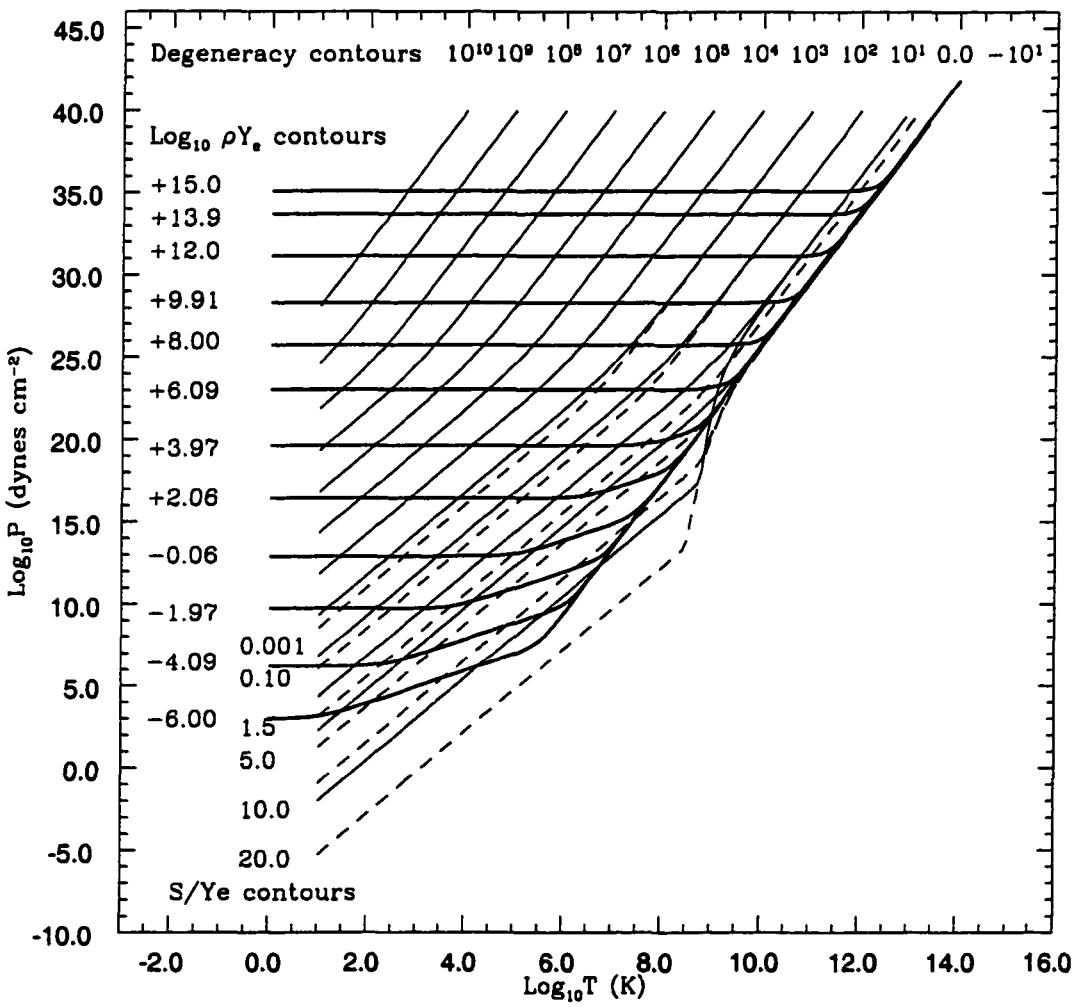
Degeneracy contours 10^10 10^9 10^8 10^7 10^6 10^5 10^4 10^3 10^2 10^1 0.0 −10^1
Log10 ρYe contours
+15.0
+13.9
+12.0
+9.91
+8.00
+6.09
+3.97
+2.06
−0.06
−1.97
−4.09
−6.00
S/Ye contours
0.001
0.10
1.5
5.0
10.0
20.0
Log10P (dynes cm−2)
Log10T (K)
45.0
40.0
35.0
30.0
25.0
20.0
15.0
10.0
5.0
0.0
-5.0
-10.0
-2.0
0.0
2.0
4.0
6.0
8.0
10.0
12.0
14.0
16.0

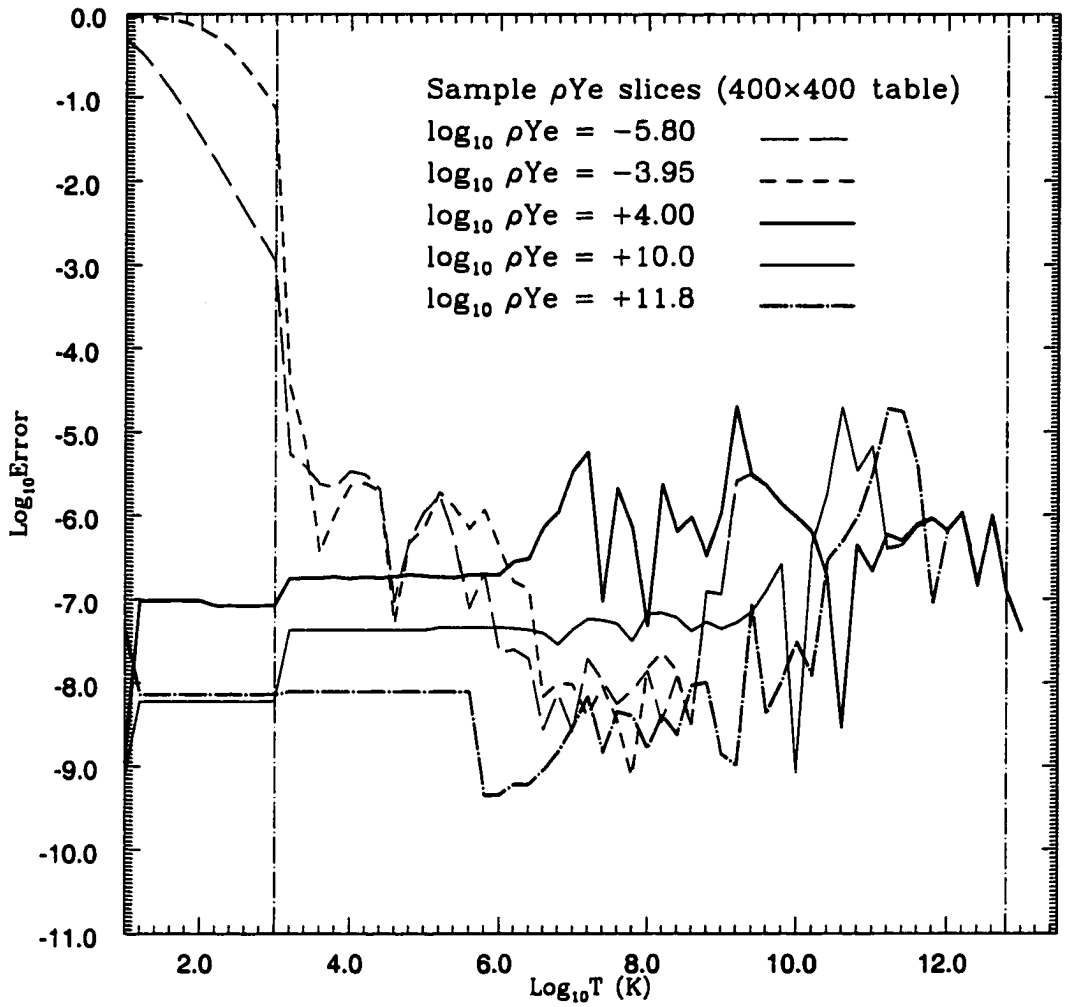

Figure C.13 Accuracy of 400 × 400 EOS table. The solid, vertical lines indicate the range of the table in temperature. The error measures the fractional difference between the exact pressure found by integrating the Fermi-Dirac integrals and the pressure interpolated from the table for the selection of densities and temperatures shown. Pressures off the table are taken from the appropriate approximation, as discussed in the text.

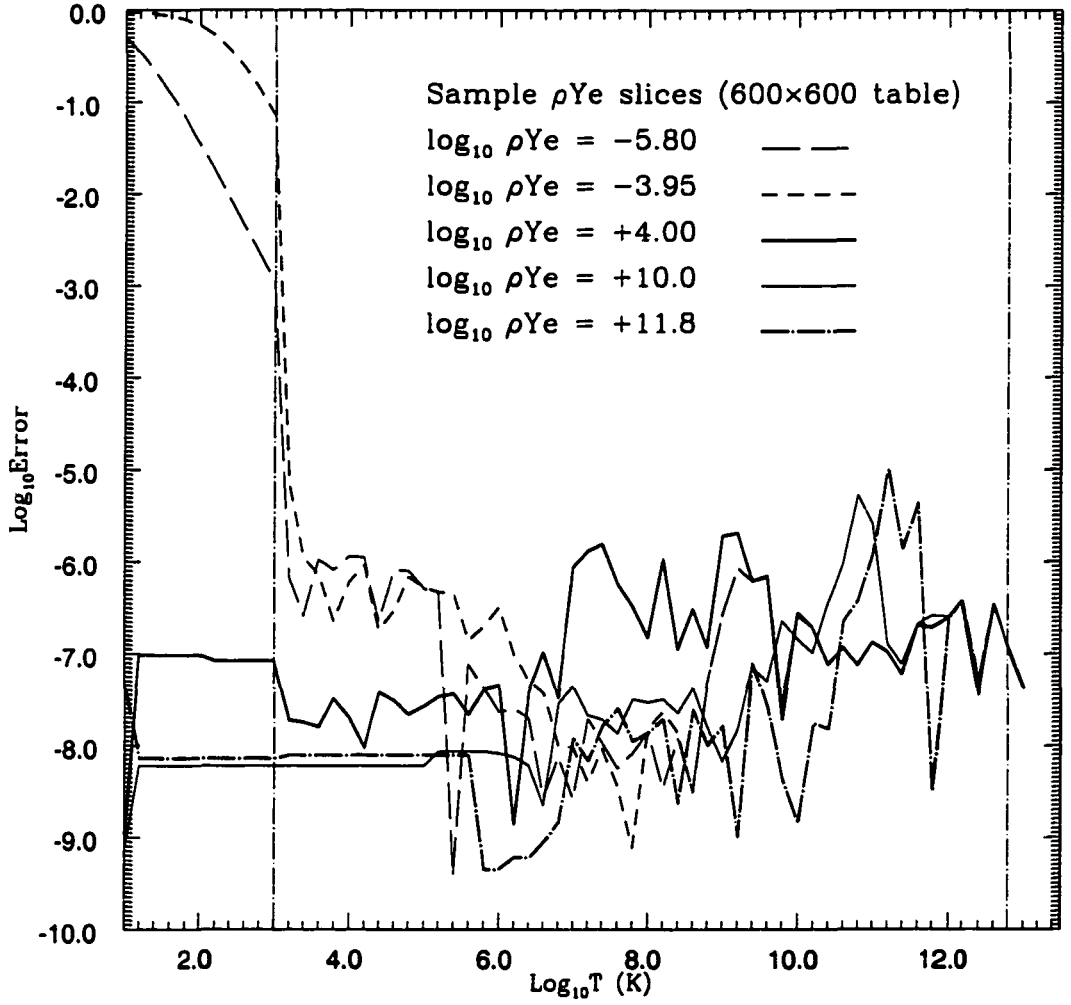

Figure C.14 Accuracy of 600 × 600 EOS table. The solid, vertical lines indicate the range of the table in temperature. The error measures the fractional difference between the exact pressure found by integrating the Fermi-Dirac integrals and the pressure interpolated from the table for the selection of densities and temperatures shown. Pressures off the table are taken from the appropriate approximation, as discussed in the text.

REFERENCES

Applegate, J. H., & Terman, J. L. 1989, ApJ, **340**, 380

Arnett, W. D., Fryxell, B., & Müller, R. 1989, ApJ, **341**, L63

Benvenuto, O. G., & Althaus, L. G. 1999, MNRAS, **303**, 30

Branch, D., Buta, R., Falk, S. W., McCall, M. L., Sutherland, P. G., Uomoto, A., Wheeler, J. C., Wills, B. J. 1982, ApJ, **252**, L61

Branch, D., Pauldrach, W. A., Puls, J., Jeffery, D. J., & Kudritzki, R. P. 1991, in *SN1987A and Other Supernovae*, eds. J. Danziger et al., (Garching: ESO)

Branch, D., Livio, M., Yungelson, L. R., Boffi, F. R., & Baron, E. 1995, PASP, **107**, 1019

Chaboyer, B. 1998, private communication

Chandrasekhar, S. 1957, *Introduction to Stellar Structure*, (University of Chicago Press, Chicago)

Cheng, A. 1974, Ap&SS, **31**, 49

Chugai, N. N. 1986, *Soviet Astronomy*, **30**, 563

Clayton, D. C. 1983, *Principles of Stellar Evolution and Nucleosynthesis*, (University of Chicago Press, Chicago)

Colella, P., & Woodward, P. 1984, *J. Comp. Phys.*, **54**, 174

Colgate, S. A. 1970, Nature, **225**, 247

Cox, J. P., & Giuli, R. T. 1968, *Principles of Stellar Structure, Volume 1 and 2*, (Gordon and Breach, New York)

Della Valle, M., & Livio, M. 1994, ApJ, **423**, L31

Della Valle, M., Benetti, S., & Panagia, N. 1996, ApJ, **459**, L23

Eggleton, P. P. 1983, ApJ, **268**, 368

Filippenko, A. V. 1997, ARA&A, **35**, 309

Fryxell, B. A., & Arnett, W. D. 1981, ApJ, **243**, 994

Green, E. 1999, personal communication

Hachisu, I., Kato, M. & Nomoto, K. 1996, ApJ, **470**, L97

Hachisu, I., Kato, M. & Nomoto, K. 1999a, preprint

Hachisu, I., Kato, M. & Nomoto, K., & Umeda, H. 1999b, preprint

Ho, L. C., & Filippenko, A. V. 1995, ApJ, **444**, 165

Iben, I., Jr., & Tutukov, A. 1984, ApJS, **54**, 335

Iben, I., Jr., Tutukov, A. 1986, ApJ, **311**, 742

Iben, I., Jr., & Tutukov, A. 1991, ApJ, **370**, 615

Iben, I., Jr., & Livio, M. 1993, PASP, **105**, 1373

Iben, I., Jr., Tutukov, A. 1993, ApJ, **418**, 343

Iben, I., Jr., & Tutukov, A. 1994, ApJ, **431**, 264

Israelian, G., Rebolo, R., Basri, G., Casares, J., & Martín, E. L. 1999, submitted to Nature, January 1999

Jeffery, D. J., Leibundgut, B., Kirshner, R. P., Benetti, S., Branch, D., & Sonneborn, G. 1992, ApJ, **397**, 304

Kenyon, S. J., Livio, M., Mikolajewska, J., Tout, C. A. 1993, ApJ, **407**, L81

Kippenhahn, R. & Weigert, A. 1991, *Stellar Structure and Evolution*, (Springer-Verlag, New York)

Li, X.-D., & van den Heuvel, E. P. J. 1997, A&A, **322**, L9

Livio, M. & Truran, J. W. 1992, ApJ, **389**, 695

Livio, M. 1999, preprint

Liebundgut, B., Kirshner, R. P., Filippenko, A. V., Shields, J. C., Foltz, C. B., Phillips, M. M., Sonneborn G. 1991, ApJ, **371**, L23

Livne, E., Tuchman, Y., & Wheeler, C. J. 1992, ApJ, **399**, 665

Marsh, T. R., Dhillon, V. S., & Duck, S. R. 1995, MNRAS, **275**, 828

Müller, E., & Steinmetz, M. 1995, *Computer Physics Communications*, **89**, 45

Nomoto, K. 1982, ApJ, **253**, 798

Nomoto, K. 1982, ApJ, **257**, 780

Nomoto, K., Thielemann, F.-K., & Yokoi, K. 1984, ApJ, **286**, 644

Nomoto, K., & Kondo Y. 1990, ApJ, **367**, L19

Parker, P. H., Bahcall, J. N. & Fowler, W. A. 1964, ApJ, **139**, 602

Pinto, P. et al. 1999, in prep.

Press, W. H., Teukolsky, S. A., Vettering, W. T., Flannery, B. P., 1992, *Numerical Recipes in C*, (Cambridge University Press)

Polcaro, V. F., & Viotti, R. 1991, A&A, **242**, L9

Rappaport, S., DiStefano, R., & Smith, J. D. 1994, ApJ, **426**, 692

Ruiz-Lapuente, P., Jeffrey, D. J., Challis, P. M., Filipenko, A. V., Kirshner, R. P., Ho, L. C., Schmidt, B. P., Sánchez, F., & Canal, R. 1993, Nature, **365**, 728

Ruiz-Lapuente, P. 1996, in the proceedings of the NATO-ASI on Thermonuclear Supernovae, held in Aiguablava, Spain, June 19-30, 1995, *Thermonuclear Supernovae*, 205 (Kluwer Academic Publishers)

Ruiz-Lapuente, P. 1997, *Science*, **276**, 1813

Saffer, R. A., Livio, M., & Yungelson, L. R. 1998, ApJ, **502**, 394

Sills, A., Lombardi, J. C. Jr., Bailyn C. D., Demarque P., Rasio F. A., & Shapiro S. L. 1997, ApJ, **487**, 290

Sofia, S. 1967, ApJ, **149**, L59

Taam, R. E., & Fryxell, B. A. 1984, ApJ, **279**, 166

Tutukov, A. V., Yungelson, L. R., & Iben, I., Jr. 1992, ApJ, **386**, 197

Turatto, M., Benetti, S., Cappellaro, E., Danziger, I. J., Della Valle, M., Gouiffes, C., Mazzali, P. A., & Patat, F. 1996, MNRAS, **283**, 1

Verbunt, F. & Zwaan, C. 1981, A&A, **100**, L7

Webbink, R. F. 1984, ApJ, **277**, 355

Wheeler, C. J., Lecar, M., & McKee, C. F. 1975, ApJ, **200**, 145

Wheeler, J. C., & Harkness, R. P. 1990, Rep. Prog. Phys., **53**, 1467

Wheeler, C. J. 1992, IAU Symposium 151 *Evolutionary Processes in Interacting Binary Stars*, eds. Y. Kondo et al., (Kluwer Academic Publishers)

Whelan, J. & Iben, I. 1973, ApJ, **186**, 1007

Woodward, P., & Colella, P. 1984, *J. Comp. Phys.*, **54**, 115

Woosley, S. E., & Weaver, T. A. 1986, ARA&A, **24**, 205

Woosley, S. E., & Weaver, T. A. 1994, ApJ, **423**, 371

Yungelson, L., Livio, M., Tutukov, A., & Kenyon, S. J. 1995, ApJ, **447**, 656

Yungelson, L., Livio, M. 1998, ApJ, **497**, 168

This manuscript was prepared with the AAS LaTeX macros v4.0.